AN ABSTRACT OF THE DISSERTATION OF

Daniel Gaebele for the degree of Doctor of Philosophy in Electrical and Computer Engineering presented on May 24, 2021.

Title: Global Hierarchical Control of a Park of Spar Buoy-type Floating Oscillating Water Column Wave Energy Converters

Abstract approved: _____

Mario E. Magaña

Converting energy from ocean waves is a challenging area for control theory application because of the nonlinear dynamics in various time scales. Generally, wave energy converter (WEC) control is applied in order to maximize power absorption, in the most common wave conditions, and subject to the devices' physical constraints. Commonly, researchers and designers prescribe the type of control algorithm based on the WEC archetype and its actuators. However, due to the nonlinear response to the constantly varying ocean waves, a single controller is unlikely to fit all operating conditions. This dissertation presents a global hierarchically controlled park of floating oscillating water column (OWC) spar-buoy type WECs for grid-scale power production. The controller is composed of a hierarchical controller and a subset of local controllers. The supervisory controller, which is based on the discrete event systems dynamics, ensures a safe and power-improving behavior, by enabling dif-

ferent local controllers depending on the current operating regime. The knowledge incorporated in the supervisor is based on a detailed state-space model of a park of seven OWCs, developed from scratch. This control-oriented wave-to-wire model considers hydrodynamic interactions, nonlinear forces, air compressibility, and a shared mooring configuration in six degrees of freedom. The novel local controllers include a robust second-order sliding mode controller, for reference following between a server and client WEC array and an algorithm for power shedding when needed. The results show good potential for the application of the standard supervisory control approach in Wave Energy, due to its adaptability to different WEC types and incorporation of safety mechanisms.

Global Hierarchical Control of a Park of Spar Buoy-type Floating
Oscillating Water Column Wave Energy Converters

by

Daniel Gaebele

A DISSERTATION

submitted to

Oregon State University

in partial fulfillment of
the requirements for the
degree of

Doctor of Philosophy

Presented May 24, 2021
Commencement June 2021

Doctor of Philosophy dissertation of Daniel Gaebele presented on May 24, 2021.

APPROVED:

_____

Major Professor, representing Electrical and Computer Engineering

_____

Head of the School of Electrical Engineering and Computer Science

_____

Dean of the Graduate School

I understand that my dissertation will become part of the permanent collection of Oregon State University libraries. My signature below authorizes release of my dissertation to any reader upon request.

_____

Daniel Gaebele, Author

ACKNOWLEDGEMENTS

First, I would like to thank my major advisor Professor Magaña for this incredible opportunity to pursue a Ph.D. in the heart of the Willamette Valley. I am grateful for his trust in me and my work and his extensive knowledge on systems theory. I highly value his continued support and his sponsoring through the National Science Foundation (Award Number: 1711859).

I would like to thank my committee, Professor Brekken for his contagious excitement about renewable energy and his teaching on electric machines, Professor Cao for his inspiring dedication and his introduction to power electronics and Professor Cotilla-Sanchez for always creating a light-hearted atmosphere. Many thanks to Professor Henriques and the IST team in Lisbon for their collaboration and their expertise on OWCs equipped with the biradial turbine. Thanks to PMEC and the PMEC cohort for broadening my contact with marine renewable energy.

Special thanks to my family for their unconditional support and their love. Merci to Matt for our swims in rivers, lakes and the ocean. Thanks to Jesse for our long runs in the McDonald forest and the unforgettable runs in the Cascades. I acknowledge the incredible privilege of an extended, yet limited, immune system to share outdoor activities with friends during a global pandemic.

Unlimited thanks to Ali. Besides sharing all my favourite activities, thank you for tranquilly sharing our (bedroom) office, sharing our meals and sharing our lives. You are making me a better researcher, writer and human. *Alles zusammen!*

TABLE OF CONTENTS

TABLE OF CONTENTS (Continued)

TABLE OF CONTENTS (Continued)

LIST OF FIGURES

LIST OF FIGURES (Continued)

LIST OF TABLES

LIST OF APPENDIX TABLES (Continued)

NOMENCLATURE

Abbreviations

WEC	wave energy converter
OWC	Oscillating water column
DoF	degree of freedom
BEM	Boundary-Element method
OSU	Oregon State University
PM	Pierson–Moskowitz
PTO	Power take-off
CoG	Center of gravity
ES	energy storage
SOC	state of charge
IB	inter body
HSSV	High Speed Stop Valve
PE	power electronics
SC	Squirrel-cage
AC	alternating current
DC	direct current
IC	initial condition
IRF	impulse response function
RMS	root mean square

Formula Signs

formula symbol	unit	description
P_{w}	kW/m	mean wave power density
T_{p}	s	wave (peak) energy period
H_{s}	m	significant wave height
ρ_{w}	kg/m^3	density of sea water $\rho_{\mathrm{w}} = 1025\,\mathrm{kg}$
g	m/s^2	earth acceleration $g = 9.81\,\mathrm{m/s}^2$
λ	m	wave length
T	s	wave period (regular)
k	rad/m	angular repetency (wave number)
ω	rad/s	angular wave frequency
d_{w}	m	water depth
v_{p}	m/s	phase velocity
η	m	free surface elevation
A_{w}	m	wave amplitude
$S(\cdot)$	m^{2}s/rad	wave energy spectrum
A_{PM}	m^2/s^4	Pierson-Moskowitz coefficient
B_{PM}	1/s^4	Pierson-Moskowitz coefficient
f_{p}	1/s	wave peak frequency
ω_n	rad/s	single frequency component
$\lvert A(\omega_n) \rvert$	m	amplitude modulus
N_{w}	-	number of irregular wave components
ϕ_n^{RND}	rad	wave random phase component

formula symbol	unit	description
q	-	interaction factor
θ_m	°	incident wave angle from direction m
d_{s}	m	array separation distance
x	m	surge coordinate (Note: state variables are either bold, or have a subscript)
y	m	surge coordinate
z	m	heave coordinate
r^x	m	roll coordinate
r^y	m	pitch coordinate
r^z	m	yaw coordinate
$\boldsymbol{x}$	multiple	state vector
$\boldsymbol{u}$	multiple	control input vector
$\boldsymbol{x}_{\mathrm{pos}}$	m	position state vector
$\boldsymbol{\mathcal{X}}_{\mathrm{pos}}$	m	concatenated park position state vector
$\hat{\boldsymbol{\mathcal{X}}}_{\mathrm{pos}}$	m/s	concatenated park velocity state vector
$\hat{\boldsymbol{x}}_{\mathrm{vel}}$	m/s	velocity state vector
$\boldsymbol{x}_{p^*}$	$-$	relative air pressure state vector
$\boldsymbol{x}_{\Omega}$	rad/s	rotational speed state vector
x_{SOC}	$-$	state of charge

formula symbol	unit	description
$\boldsymbol{M}$	kg,kgm^2	inertia matrix
$\boldsymbol{F}^{\mathrm{H}}$	N	hydrostatic restoring force vector
$\boldsymbol{F}^{\mathrm{M}}$	N	mooring force vector
$\boldsymbol{F}^{\mathrm{Ex}}$	N	excitation force vector
$\boldsymbol{F}^{\mathrm{R}}$	N	radiation damping force vector
$\boldsymbol{F}^{\mathrm{PTO}}$	N	PTO pressure induced force vector
$\boldsymbol{F}^{\mathrm{VD}}$	N	viscous drag force vector
$\boldsymbol{J}_r$	–	linear mapping between body and world frame
$\boldsymbol{R}_r$	–	intrinsic rotation matrix about r_i^z, r_i^x, r_i^y
$\boldsymbol{T}_r$	–	rotation matrix for translations
S_b, S_p	m^2	cross sectional area of buoy $_b$ or piston $_p$
V_b	m^3	volume of water displaced by the buoy
$\overline{GM}$	m	metacentric height

formula symbol	unit	description
L_1, L_2, L_3	m	length of bottom mooring lines segments 1,2 and 3
$\alpha_1, \alpha_2, \alpha_3$	°	angles between bottom mooring lines segments and horizontal
w_{L}	kg/m	bottom mooring line weight per unit length
F_{C}	N	vertical force due to clump weight in bottom mooring line
F_{J}	N	vertical force due to jumper float in bottom mooring line
$T_{\mathrm{b}}, T_{\mathrm{a}}$	N	bottom mooring line tension at the buoy and the anchor
h_{fl}	m	horizontal distance between fairlead at buoy and anchor
z_{fl}	m	vertical distance between fairlead at buoy and anchor
L_{IB}	m	length of inter-body mooring line segment
$F_{\mathrm{C,IB}}$	N	vertical force due to clump weight in inter-body mooring
$T_{\mathrm{IB,s}}, T_{\mathrm{IB,e}}$	N	inter-body mooring line tension at the start buoy and the end buoy
$\alpha_{\mathrm{s}}, \alpha_{\mathrm{e}}$	°	angles between inter-body mooring lines segments and horizontal
$\boldsymbol{p}_{\mathrm{fl}}$	m	fairlead position vector
$\boldsymbol{v}_{\mathrm{IB,s}}, \boldsymbol{v}_{\mathrm{IB,e}}$	m	direction vector inter-body mooring tension
$\boldsymbol{v}_{\mathrm{BTM}}$	N	direction vector bottom mooring
$\hat{\boldsymbol{F}}_{\mathrm{IB,s}}, \hat{\boldsymbol{F}}_{\mathrm{IB,e}}$	N	inter-body mooring force vector for start and end
$\hat{\boldsymbol{F}}_{\mathrm{BTM}}$	N	bottom mooring force component vector
$\hat{\boldsymbol{T}}_{\mathrm{IB,s}}, \hat{\boldsymbol{T}}_{\mathrm{IB,e}}$	N	inter-body mooring torque vector for start and end
$\hat{\boldsymbol{T}}_{\mathrm{BTM}}$	N	bottom mooring torque component vector

formula symbol	unit	description
$\boldsymbol{D}^{\theta}$	°	incident wave spread vector
N_{θ}	–	number of incident wave directions
$\boldsymbol{\phi}^{\text{SH}}$	–	incident wave location shift vector
N_{w}	–	number of wave frequencies
$\boldsymbol{\Gamma}$	kg/s^2	excitation force coefficient vector
$\boldsymbol{\phi}^{\text{Ex}}$	°	excitation force coefficient phase vector
A^{∞}	kg	added mass coefficient at infinite frequency
$K(t)$	kg/s^2	radiation impulse response function
$B(\omega)$	kg/s	radiation damping coefficient
H	kg/s^2	Hankel matrix
$\boldsymbol{S}$	kg/s^2	matrix of singular values
$A^{\text{R}}, B^{\text{R}}, C^{\text{R}}, D^{\text{R}}$	multiple	radiation state space matrices
ρ_{c}	kg/m^3	air density in chamber
ρ_{in}	kg/m^3	density of flow into turbine
V_{c}	m^3	volume of air chamber
h_0	m	height air chamber at calm sea
p	N/m^2	pressure inside air chamber
p_{at}	N/m^2	atmospheric pressure
ρ_{at}	kg/m^3	atmospheric air density
p^*	–	dimensionless relative pressure
γ	-	specific heat ratio of air

formula symbol	unit	description
I_t	kgm^2	moment of inertia turbine/generator set
B_t	kgm^2/s	turbine friction coefficient
T_t	Nm	turbine torque
T_gen	Nm	generator torque
d_t	m	turbine diameter
Ψ	–	dimensionless pressure head
Φ	–	dimensionless low rate
Π	–	dimensionless power coefficient
η_t	–	turbine efficiency
$u_\mathrm{HSSV,\times}$	–	position high speed stop valve
$\dot{m}_\mathrm{t}$	kg/s	mass flow through turbine
C_VD	–	matrix with quadratic drag coefficients
A_VD	m^2	reference area matrix for drag coefficients
η_gen	–	efficiency generator
$P_\mathrm{elec}^\mathrm{AC}$	W	alternating current electric power
$P_\mathrm{elec}^\mathrm{DC}$	W	dirrect current electric power
η_PE	–	efficiency power electronics
P_link	W	electric power in the DC link network
P_load	W	electric power transmitted to the power grid
η_SM	–	efficiency storage medium
$W_\mathrm{SM}^\mathrm{rated}$	J	rated storage capacity of the storage medium

formula symbol	unit	description
$\bar{z}_{\text{server}}^{\text{RMS}}$	m	measure for motion of the server array
$\bar{P}_{\text{mech}}$	W	time averaged mechanical power
Q	–	set of discrete states
Gi	–	WEC Automaton
Q_{m}	–	set of marked states
Q_{D}	–	set of desired states
u_j	–	uncontrollable discrete event j
c_k	–	controllable discrete event k
Σ	–	set if all discrete event
δ_i	–	state transition function (uncontrolled)
D	–	desired WEC Automaton
S	–	supervisor of WEC
T	–	state observer of supervisor
ψ	–	supervisor output map
K	–	language of desired WEC Automaton behaviour

Convention

Most quantities in this work are time varying. Therefore, the time dependency notation (t) is omitted in most cases, except when confusion with constant quantities could arise, or when the time dependency needs to be emphasized. Generally, vectors

are denoted with bold lowercase letters, e.g. $\boldsymbol{x}$. There are three main categories denoted by capital letters. First, variables that are commonly denoted with capital letter in the literature, for example volume V. Second, forces F, which are also found in vectorized form $\boldsymbol{F}$. Third, matrices, e.g. the state space system matrices, A,B,C and D. Concatenated matrices and forces, i.e. matrices and forces with multiple previously introduces matrices and force as their entries, respectively, are denoted by bold, script, capital letters, such as the park inertia matrix $\boldsymbol{\mathcal{M}}$ and the generalized park force vector $\boldsymbol{\mathcal{F}}$. The dot accent denotes the time derivative of the respective variable, for example $\dot{\boldsymbol{x}}$. The lowercase $f()$ illustrates the dependency of a variable, on other variables, but the actual *function* is not necessarily specified, e.g. $\dot{\boldsymbol{x}} = f(\boldsymbol{x}, \boldsymbol{u})$. The notation of dependency is not limited to $f()$, but can be used for all variables to emphasize their explicit dependency on other variables, such as the frequency dependency, or the dependency on the turbine pressure head.

PREFACE

Converting energy from ocean waves is a challenging area for control theory application because of the nonlinear dynamics in various time scales. Generally, wave energy converter (WEC) control is applied in order to maximize power absorption, in the most common wave conditions, and subject to the devices' physical constraints. Commonly, researchers and designers prescribe the type of control algorithm based on the WEC archetype and its actuators. However, due to the nonlinear response to the constantly varying ocean waves, a single controller is unlikely to fit all operating conditions. This dissertation presents a global hierarchically controlled park of floating oscillating water column (OWC) spar-buoy type WECs for grid-scale power production. The controller is composed of a hierarchical controller and a subset of local controllers. The supervisory controller, which is based on the discrete event systems dynamics, ensures a safe and power-improving behavior, by enabling different local controllers depending on the current operating regime. The knowledge incorporated in the supervisor is based on a detailed state-space model of a park of seven OWCs, developed from scratch. This control-oriented wave-to-wire model considers hydrodynamic interactions, nonlinear forces, air compressibility, and a shared mooring configuration in six degrees of freedom. The novel local controllers include a robust second-order sliding mode controller, for reference following between a server and client WEC array and an algorithm for power shedding when needed. The results show good potential for the application of the standard supervisory control approach in Wave Energy, due to its adaptability to different WEC types and incorporation of

Chapter 1 Introduction

Oceans will play a big role in the mitigation of climate change. One of the many ways that they will do so is by offering a vast, currently untapped renewable energy source. This is where this work comes in as a small component. Converting energy from ocean waves is a challenge for control engineers who are tasked to make the wave energy capturing devices more efficient and more robust with less cost compared to mechanical solutions. One popular method of control design is modelling. The model should simplify a real world process just enough to reproduce it's essential dynamics, without making it unnecessarily complex. Designers can use such a model to test and evaluate new concepts quicker and cheaper when compared to physical experiments. Control engineers use systems and control theory to design algorithms which change the systems time behaviour based on the model by closing the loop and making decisions based on the instantaneous system state. These algorithms make up what is known as a controller. Commonly, researchers and engineers prescribe the type of control algorithm based on the wave energy converter (WEC) archetype and its actuators to optimize the hydrodynamic interactions. However, due to the nonlinear response to the constantly varying ocean waves, a single controller is unlikely to fit all operating conditions and WEC types. This dissertation presents a global hierarchically controlled park of multiple identical floating oscillating water column (OWC) Spar-buoy type WECs for grid-scale power production. The controller is composed

of a hierarchical controller and a subset of local controllers, specifically designed for this type of WEC. The underlying model is a state-space model of seven OWCs, developed from scratch based on first principles. This control-oriented wave-to-wire model considers hydrodynamic interactions, nonlinear forces, air compressibility, and a DC-link network between the WECs in the park.

1.1   Outline

This work starts with an assessment of the global wave energy resource in Sec. 1.2 followed by the mathematical description of regular and irregular waves in Sec. 1.2.1. To convert energy from waves a device called a wave energy converter (WEC) needs to be placed in the wave field. The interactions between waves and small bodies are addressed in Sec. 1.2.2 followed by the mathematical description of the fundamental interactions in Sec. 1.2.3. After this theory section, the history of wave energy conversion is discussed in Sec. 1.3 and an overview of different devices is given in Sec. 1.3.1. Controls research for ocean wave energy converters began concurrently with the first fundamental research in the field in the 70s and a summary of the development and common strategies are presented in Sec. 1.3.2. The thesis will deal with a specific kind of promising WEC, a floating Oscillating Water column (OWC) of the Marmok-A-5 type introduced in Sec. 1.4. This Spar-buoy type WEC requires a rectifying air turbine to convert alternating air flow into kinetic energy. Types and working principles of rectifying air turbines are introduced in Sec. 1.4.1. The next steps in the energy conversion chain, namely the electro-magnetic and the electric

energy conversion, are first mentioned in Sec. 1.5 within the discussion of wave to wire models. Those models enable the emulation of the real world, and further the assessment of new ideas and concepts without the cost and risk of physical experiments. One popular theoretical concept is the deployment of multiple identical WECs in a WEC park to save cost associated with maintenance and mooring systems, introduced in Sec. 1.5.1. However, there are two challenges which stand in the way of developing successful Spar-buoy OWC parks. First, hydrodynamic interactions and shared mooring systems complicate the modeling process of WEC parks and second, the common WEC control strategies are not applicable to floating OWC WECs due to the physics of their actuators.

The main body of this work starts with the development of a dynamic model of a park of seven hydro-dynamically interacting Marmok-A-5 floating OWC WECs with shared mooring system, in all degrees of freedom (DoFs) in Chap. 2. The concept of energy conserving physical quantities in a single OWC WEC, the relation to the widely used State Space Representation, and the corresponding state vector for the OWC WEC park are presented in Sec. 2.1.1, Sec. 2.1.2 and Sec. 2.1.3, respectively. The state dynamics are governed by equations representing the physical forces (Sec. 2.2) and control inputs that are identified. The considered individual forces are modeled in detail in the ensuing sections. Namely, the linear hydrostatic restoring force (Sec. 2.2.2), the nonlinear mooring force resulting from a quasi-static approach to model a shared mooring system (Sec 2.2.3), the irregular excitation forces based on linear hydrodynamic coefficients (Sec. 2.2.4), the radiation force approximated with linear state space systems including interactions with other WECs in the park

(Sec. 2.2.5), the force due to the pressure in the air chamber connecting the WEC, the water column and the biradial turbine (Sec. 2.2.6) and finally, the linear viscous drag force (Sec. 2.2.7). The electric power flow is modeled by considering the conversion losses from the AC generators over a DC link, including a storage unit to the grid connection in Sec.2.3. All the modeled components are connected in Sec. 2.4 with the full vectorized and concatenated state space representation of the entire WEC park.

The mathematical model developed after first principles is not helpful without numerical parameters quantifying the dynamics. The main drivers of the OWC WEC park are its hydrodynamic properties, which are obtained in Chap. 3. The linear hydrodynamic coefficients result from boundary element (BEM) solver ANSYS AQWA (Sec. 3.1). Due to limitations of the BEM software two different BEM simulations had to be conducted. First, a detailed simulation of three Marmok-A-5 WECs with imaginary rigid body, representing the full internal water column in Sec. 3.1 and second a simulation of the seven physical buoys in the WEC park configuration, without the internal imaginary body representing the water column. The first model is used for detailed radiation properties inside single WEC and with the nearby WECs and the second model for the diffraction and excitation properties of the park layout. The order of theoretical hydrodynamic interactions between the distinct WECs in all DoFs is enormous. Therefore, several interactions need to be neglected as part of the post processing of hydrodynamic results, which discussed in the section of the respective hydrodynamic coefficient, namely, the added mass Sec. 3.3, the radiation damping in Sec. 3.4 and the excitation force and the corresponding phase coefficient in Sec. 2.2.4.

A direct validation of the model with experimental data is not possible, since floating OWC WEC parks are still a theoretical concepts. However, numeric experiments with predictable outcome are conducted and evaluated in Chap. 4. As first step, the model is simulated without ocean waves under varying initial conditions and the decaying behavior is observed in Sec. 4.2. Next, the behavior in irregular wave fields, with varying sea states and angles of arrival is observed and discussed in Sec. 4.3.

One main finding is that the kinetic energy transferred to the WEC (in terms of it's heave oscillation) strongly varies over the time scale of a few minutes, although exposed to the same sea climate, due to the highly nonlinear system response. This motivates to regard the WEC parks as a system with different operating regimes, e.g. a low energetic response and a near resonance response resulting in high energy transfer and potentially the need for shedding power to protect system components. This class of systems is generally known as discrete event systems and addressed in Chap. 5. An event can randomly occur and change the systems discrete state. The time continuous dynamics between events are irrelevant for the transition between different states of the OWC WEC park. The possible behavior together with the desired behavior and the necessary control actions are modeled in terms of a discrete events Automaton in Sec.5.1. This results in a hybrid system modelling of the global state of the WEC park.

Although the control inputs have been identified in the dynamic model and are respected in the discrete event model, their design is first addressed in Chap. 6. The first section introduces local controllers (Sec. 6.1), such as a feedback control law

for generator torque based on the turbine angular speed and the maximization of the turbine aerodynamic efficiency (Sec. 6.1.1). Next a novel second-order sliding mode control approach is designed for turbine reference speed following (Sec. 6.1.2). The reference velocity is dynamically computed in a server-client manner between different WECs in the park. A simple power shedding valve control is suggested based on limiting the turbine rotational subject to an efficient electro-magnetic energy conversion in Sec. 6.1.4. Finally, for completeness, a trivial grid load control algorithm is proposed in Sec. 6.1.5. On a hierarchically higher level than the local controller sits a supervisory controller (Sec. 6.3). The supervisor is designed with the standard supervisory control using the supervisor formal language (Sec. 6.3.1) to keep the WEC park running with its desired behavior whenever possible. Protection mechanisms have to be enabled once the standard behaviour is not possible. The discrete events state observer, which connects the continuous time model with the discrete event model is presented in Sec. 6.3.2. The decision maker, which translates the supervisory decisions into the selection of a local controller is presented in Sec. 6.3.3.

Finally, the performance of the six DoF together with the proposed control algorithms is evaluated and discussed in Chap. 7

1.2 Ocean Wave Energy

Most of the available energy on earth comes from the sun, including the energy that creates ocean waves. The bodies of water on earth function as large thermal solar panels, releasing heat on the air-water interface, generating wind and consequently waves. The bigger the water surface is, the longer the distance over which the wind can accelerate the water. This distance is known as fetch and explains why the waves in the oceans are larger than waves in lakes. The waves can travel long distances without significant energy loss, therefore the energy density increases compared to underlying wind and solar sources. The mean wave power density P_w becomes a function of the wave energy period T_e and the significant wave height H_s [50], namely,

$$P_\mathrm{w} = \frac{\rho_\mathrm{w} g^2}{64\pi} T_\mathrm{e} H_\mathrm{s}^2 \tag{1.1}$$

where ρ_w is the (sea) water density and g is the earth acceleration. The denotations of T_e and H_s already imply that for a real ocean wave there is no sole wave height or period, which will be discussed in Sec. 1.2.1. Assuming a commonly found ocean wave with $H_\mathrm{s} = 2\,\mathrm{m}$ and $T_\mathrm{p} = 10\,\mathrm{s}$ results in $P_\mathrm{w} \approx 20\,\mathrm{kW/m}$. By entirely capturing only one meter of this wave energy flux, approximately 20 average US households could be powered. In [11], the authors divide the global wave climate into classes based on different ocean characteristics for device design. Their most basic classification in terms of H_s and T_e shows a distribution of P_w around the world, which is illustrated in Fig. 1.1. The grey contour indicates the $15\,\mathrm{kW/m}$ boundary for viable device deployment. The well-known wave energy researcher, António F. de O. Falcão, accesses a "good"

> 15 kW/m

> 15 kW/m

> 15 kW/m
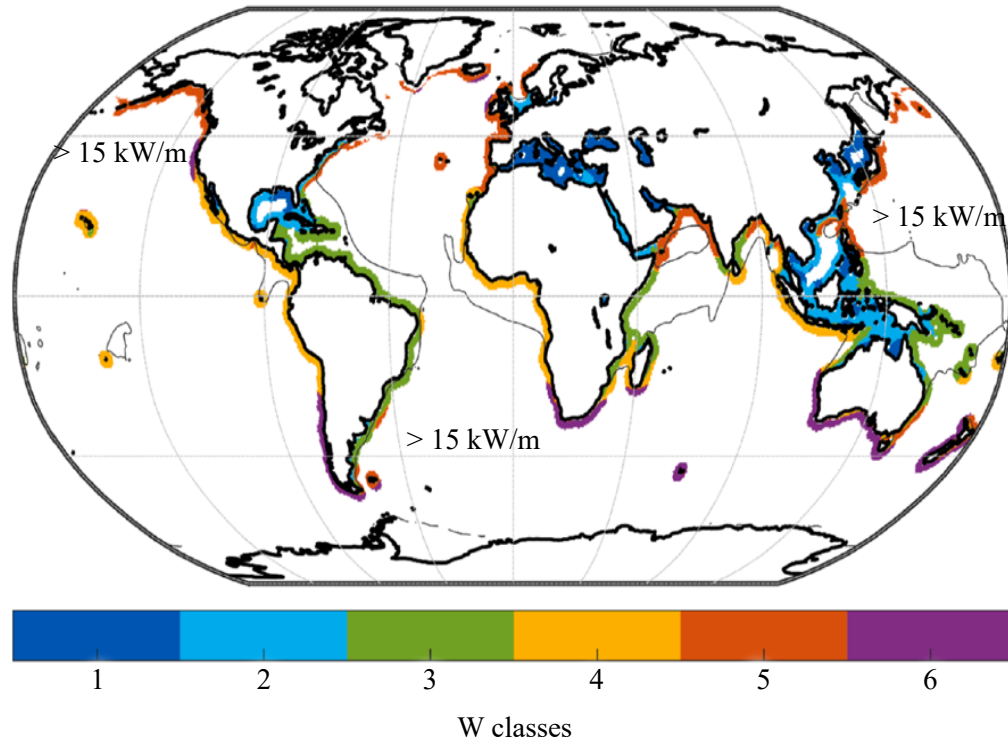
Figure 1.1: World map with classified wave energy resources [11].

offshore location if the annual average power ranges from $20\,\text{kW/m}$ to $70\,\text{kW/m}$ [14], which would be classes 4-6 in the figure. The estimated global theoretical potential is about $3365\,\text{GW}$ [36]. If an overall efficiency of 30% could be achieved the theoretical potential would be $1000\,\text{GW}$ electrical power. This is in the magnitude of the total installed wind turbine capacity will likely reach soon. (Installed wind capacity: 2019: $650\,\text{GW}$ [22], 2020: $743\,\text{GW}$ [23]). Most wave energy research is conducted in countries like USA, Canada, Portugal, Denmark, Norway and the UK, due to the higher power density on the west coasts compared to the east costs, as Figure 1.1 illustrates. This can be attributed to the westerlies, prevailing winds in rotation direction of the

earth from west to east, in the middle latitudes, based on the atmospheric pressure gradient between the subtropical high pressure belt and the polar front [34].

The US west coast has an additional difference to its east coast. The continental shelf is almost nonexisting as illustrated in Fig. 1.2 after the model of [41]. The waves experience less frictional losses with the sea floor when advancing the shore line, resulting in high ocean wave activity. The excellent wave resources among the
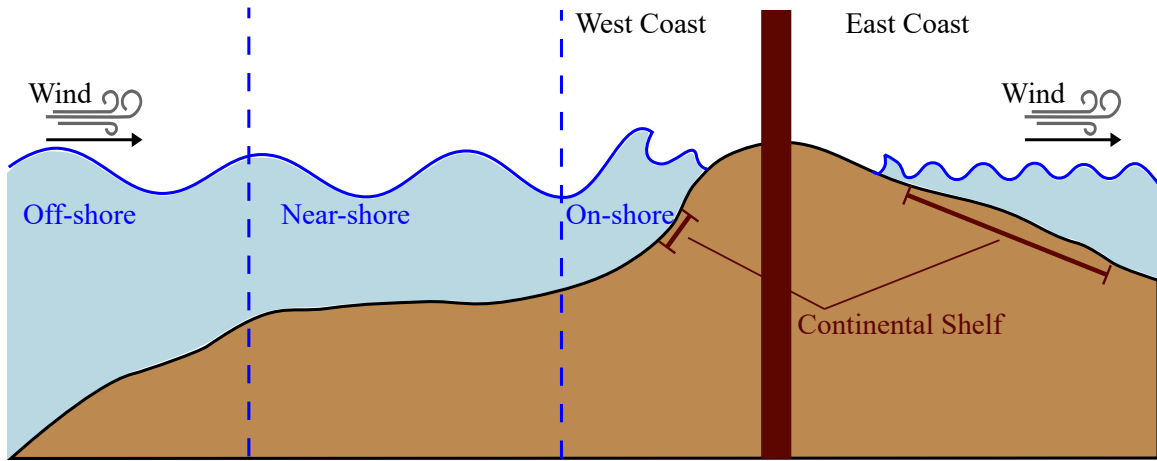
Figure 1.2: Wave formation and coastal division.

Pacific Northwest are one explanation for the high research effort conducted by higher education institutions like Oregon State University (OSU).

1.2.1 Description of Ocean Waves

An ocean wave is an unique structure and very complex compared to waves generated in a wave tank. There are different ways to classify and describe them in a more or less simplified fashion. A very comprehensive presentation can be found in the book from

Johannes Falnes [16], often referred to as the bible of ocean wave energy conversion. A swell is a set of surface gravity waves, generated far outside in the ocean due to a finished fetch. After leaving the area of generation those waves have time to structure themselves and approximately arrange to harmonic, so called regular waves, which should not be swayed by local winds, to attain a human-readable period.

1.2.1.1 Regular Waves

The period of a regular wave can either be expressed spatially, called wavelength λ, or time-wise and in the following referred to with T. The wave number can now be stated as

$$k = \frac{2\pi}{\lambda} \tag{1.2}$$

and in an analog manner the definition of the angular frequency is given by

$$\omega = \frac{2\pi}{T}. \tag{1.3}$$

Most ocean waves are still considered as surface waves, where the water is sufficiently deep to not influence the waves. By defining a water depth d_{w}, using the Laplace equation, evaluating the homogeneous boundary condition on the interface between water and air and assuming a constant pressure a relation for ω and k is found with [16],

$$\omega^2 = gk \tanh(kd_{\mathrm{w}}). \tag{1.4}$$

This is also known as the dispersion equation. If the phase velocity depends on frequency, a wave is dispersive, which is in general the case for gravity waves on water. Substituting (1.2) into $\tanh(kd)$ makes it evident that for a water depth $d_w = \lambda/2$, $\tanh(\pi) \approx 1$, wherefore equation 1.4 simplifies to

$$\omega^2 = gk. \tag{1.5}$$

Hence, $d_w > \lambda/2$ is commonly used to speak about deep water, because of the independence of the dispersion equation from the water depth. The dispersion relation yields the phase velocity (the propagation speed of the wave),

$$v_p \equiv \omega/k = g/\omega = \lambda/T. \tag{1.6}$$

On the other hand, it follows that the wave length is only a function of the time period T, namely,

$$\lambda = \frac{g}{2\pi}T^2 \approx 1.56T^2. \tag{1.7}$$

In conclusion, a regular wave can be completely described in terms of the period T and its height H. Although a sinusoidal shape is often assumed for practical use, real ocean waves are neither symmetric in the horizontal nor in the vertical direction. They more likely follow an approximately trochoidal form, which means they have a peaked crest and a flatter trough [33]. There are different ways to describe the waves in a nonlinear way and for the deep water case the method of Sir George Stokes from the 19th century is suitable [52]. After the example of Stokes a third order approach

to relate the wave elevation η with k and the position coordinate x is used, namely,

$$\eta(x) = A_\mathrm{w} \cos(kx) + \frac{1}{2}kA_\mathrm{w}^2 \cos(2kx) + \frac{3}{8}k^2 A_\mathrm{w}^3 \cos(3kx), \tag{1.8}$$

where A_w is the wave amplitude. This is also known as a Stokes wave. Consequently,

Figure 1.3: Excerpt from [52] showing a Stokes wave with $A_\mathrm{w} = 7\lambda/80$ and the plane sea level.

this representation leads to a wave height from the trough to the crest of

$$H = 2A_\mathrm{w}\left(1 + \frac{3}{8}k^2 A_\mathrm{w}\right), \tag{1.9}$$

due to the addition of all single amplitudes for $x = n\lambda$, $n \in \mathbb{N}$ leading to the crest and due the positive sign of the double frequency term for $x = (n + 1/2)\lambda$ $n \in \mathbb{N}$ in a trough. Again, for small values of k and small amplitudes the wave height becomes independent of k and converges to two times the wave amplitude. However, the maximum displacement from the sea level (gray, dashed line (----)) of the Stokes distinguishes from the harmonic trigonometric waves, which are illustrated in the top right graph in Fig. 1.4 for a Stokes wave with a period of $T = 8$s and an amplitude of

$A_{\text{w}} = 5$m with a solid dark red line (———) in comparison with a cosine function with the same period and amplitude (dotted, crimson line (⋯⋯)). The crest becomes higher and the trough lower. Nevertheless, the difference is small compared to the corresponding wave length of $\lambda = 100$m, displayed in the top left plot with equally scaled axes and becomes even less regarding sea conditions that are more likely, e.g. $T = 10$s, $A_{\text{w}} = 1$m. The more common sea conditions are displayed with the dark blue and royal blue lines for the Stokes wave and the corresponding cosine, respectively (——— / ⋯⋯)). On the bottom part of Fig. 1.4 the wave elevation η is given as a
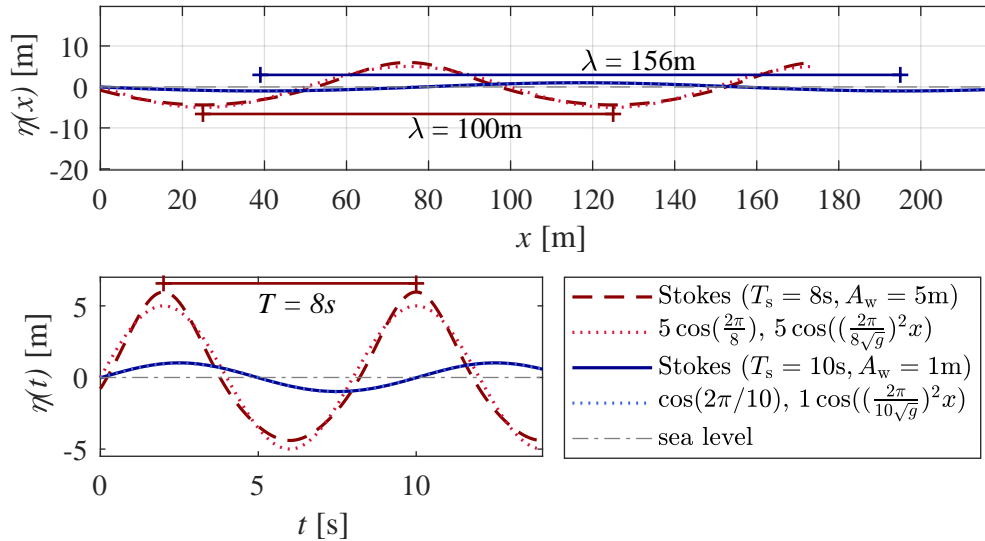
Figure 1.4: Regular waves.

function of t, following the same relation as before, namely

$$\eta(t) = A_{\text{w}} \cos(\omega t) + \frac{1}{2} k A_{\text{w}}^2 \cos(2\omega t) + \frac{3}{8} k^2 A_{\text{w}}^3 \cos(3\omega t). \tag{1.10}$$

This time dependent function will be used to emulate regular waves in the simulations in this work, with T and A_w as parameters, wherefore

$$k = \frac{1}{g} \left(\frac{2\pi}{T} \right)^2 \tag{1.11}$$

is used. All shown functions are simulated until a time of 14s, which is directly discernible in the time dependent function in the bottom part. With the top part the wave length dependent propagating speed becomes obvious, wherefore the wave with the higher period (——) travel a longer distance compared the wave with the smaller wave length.

1.2.1.2 Irregular Waves

Real ocean waves usually do not travel undisturbed over very long distances or are locally generated by the wind. This class with a stochastic nature is called irregular waves and the following descriptions follows again Falnes [16]. Approximately, they can be considered as a superposition of waves with many different frequencies, based on available statistical values of the amplitude, phase and direction of propagation. Consequently, a real sea state can be modeled with components of harmonic waves, still assuming linear wave theory. Therefore, spectral descriptions of the sea states are used, e.g. the well known Pierson-Moskowitz (PM) spectrum. This functional relation between the frequency and the corresponding energy is based on semi-empirical results

and defined as

$$S(f) = \frac{A_{\mathrm{PM}}}{f^5} \exp\left(-\frac{B_{\mathrm{PM}}}{f^4}\right), \tag{1.12}$$

where A_{PM} and B_{PM} are used to parameterize the spectrum and a feasible choice is

$$A_{\mathrm{PM}} = \frac{B_{\mathrm{PM}} H_{\mathrm{s}}^2}{4}, \text{ and } B_{\mathrm{PM}} = \left(\frac{5}{4}\right) f_{\mathrm{p}}^4. \tag{1.13}$$

Now, the definition of the significant wave height H_{s} from (1.1) can be stated as

$$H_{\mathrm{s}} = 4\sqrt{\int_0^\infty S(f)\mathrm{d}f}. \tag{1.14}$$

Here, f_{p} denotes the peak frequency, which is the inverse of the peak period T_{p}. The corresponding angular frequency ω dependent spectrum S_ω can be described by

$$S_\omega(\omega) = \frac{1}{2\pi} S\left(\frac{\omega}{2\pi}\right). \tag{1.15}$$

In Fig. 1.5 different wave spectra $S_\omega(\omega)$ for various pairs of significant wave heights H_{s} and peak periods T_{p} are illustrated. The different wave heights H_{s} are identified with the colors dark red (2.5 m), dark green (3.5 m) and dark blue (4.5 m), respectively. The varying amplitudes modulus of the harmonic wave components $|A(\omega)|$ can be calculated with the information provided be the real-valued non-negative $S_\omega(\omega)$ with

$$|A(\omega_n)| = \sqrt{2S_\omega(\omega_n)\Delta\omega}, \tag{1.16}$$
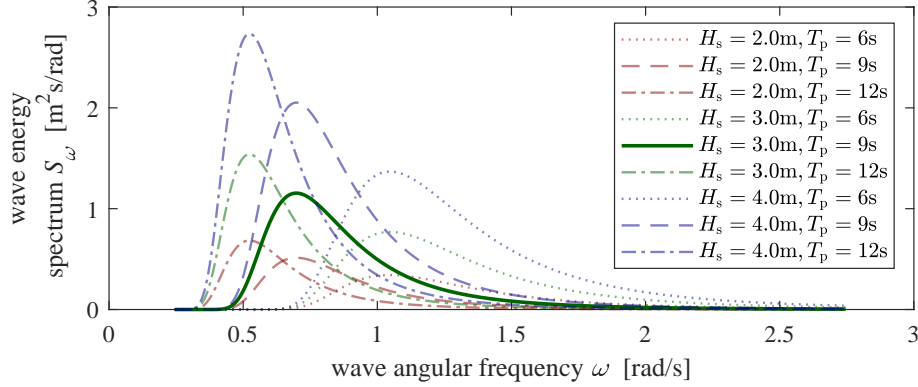
Figure 1.5: Angular frequency dependent Pierson-Moskowitz spectrum for different combinations of H_s and T_p.

where ω_n denotes a frequency in the interval of $\omega \in \left[\frac{\sqrt{6}}{10}, \frac{\sqrt{6}}{10} + 2.5\right]$ [rad/s] equally distributed into $N_\text{w} = 200$ frequencies, to cover the energy dense area of the spectrum. The irrational boundaries of the interval are chosen to avoid repetition over time for the irregular wave.

As most of the oceans energy content is associated with waves of periods between 5s to 15s, some cases in this interval are evaluated. All the dashed-dotted lines represent a spectrum with $T_\text{p} = 13$s, which is the highest depicted period, resulting in the highest energy density. The dotted lines illustrate the lower time period of $T_\text{p} = 7$s, leading to lower energy density. The more common wave frequency of $T_\text{p} = 10$s is plotted with the highest opacity and the dashed and solid lines, respectively. The only solid line in the figure represents the energy spectra, representative for most of the sea states, namely the combination of $H_\text{s} = 2.0$m and $T_\text{p} = 10$s (——), which will be used to characterize the irregular waves in this work.

The spectrum $S_\omega(\omega)$ contains no information about the phase of the individual

wave component. The phase ϕ^{RND} is assumed to be continuously uniformly distributed in the interval $[-\pi, \pi]$ for every $N_{\mathrm{w}} = 200$ components. Now, the free water surface η at time t can be computed as a superposition of every wave component with its corresponding phase as

$$\eta_0(t) = \sum_{n=1}^{N_{\mathrm{w}}} |A(\omega_n)| \cos(\omega_n t - \phi_n^{\mathrm{RND}}). \qquad (1.17)$$

The random phase ϕ_n^{RND} is generated once and later reused to have the same irregular wave for different simulation runs. As final step, the time profile $\eta_0(t)$ will be ramped, to start from rest at $t = 0\,\mathrm{s}$ with the function

$$\eta(t) = \eta_0(t) \left(\frac{2}{1 + \exp\left(-\frac{t}{2}\right)} - 1 \right) \qquad (1.18)$$

In Fig. 1.6 the surface elevation η for this wave is plotted until a time $t = 120\mathrm{s}$ and compared to a Stokes wave with the equivalent parameters, namely $T_{\mathrm{p}} \equiv T = 10\mathrm{s}$ and $H_{\mathrm{s}} \simeq 2A_{\mathrm{w}} = 2\mathrm{m}$ Note that for the excitation force and the free surface elevation in the time domain simulations the spatial coordinates and a wave spread is taken into account (see Sec. 2.2.4).

1.2.2 Wave Body Interactions

In order to use ocean waves as power source, it is necessary to understand the theory of the behavior of bodies in water. An overview introducing wave body interactions and the occurring radiation and diffraction can be found in [16] and [6]. The progress
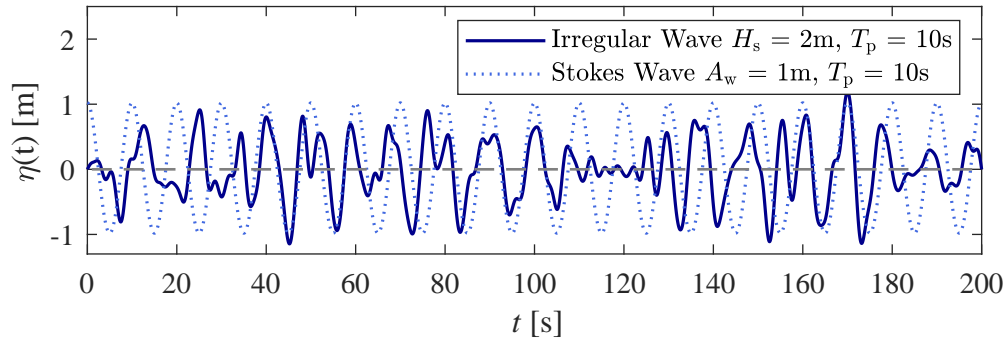
Figure 1.6: Time dependent surface elevation of an irregular wave and a Stokes wave, witch $H_s = 2$m and $T_p = 10$s.

of a plane wave meeting floating objects, in this case, small devices, the so-called point absorbers (see section 1.3.1), is visualized in Fig. 1.7 following the idea of [6] to demonstrate the effects of radiation. To simplify the illustration a calm sea surface is assumed, until in Fig. 1.7 (a) the first incident wave hits the point absorber. In order to absorb energy from the incoming plane wave the body is set into motion, hence a circular wave is radiated from the moving floating object(Fig. 1.7 (b)). On the one hand, this wave interferes constructively and destructively with the incident ocean wave and on the other hand it is an incident wave for other bodies. As time continuous in Fig. 1.7 (c) the second floating point was already exposed to multiple incident waves and is radiating circular waves as well. This wave will again propagate and interfere with both waves and bodies. It follows that responses of the bodies are dependent on the radiated waves of all the other bodies, which makes the calculation of the responses non-trivial (see section 3.4).

Another illustrated example for waves interacting with bodies with the aim to absorb the energy is found in Fig.1.8 [16]. The black cylinder in the figure represents
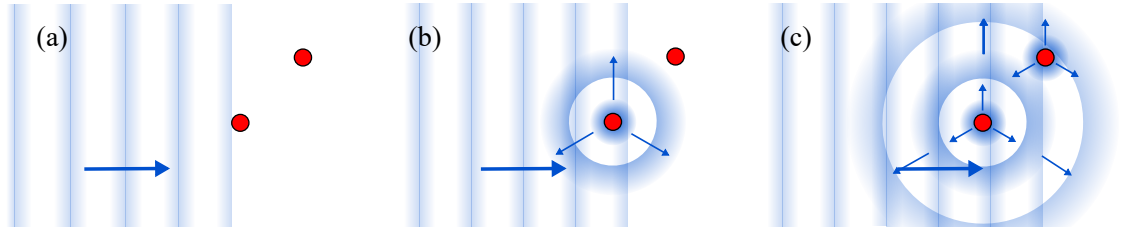
Figure 1.7: Interaction between incident waves (coming from the left) and point absorbers: (a): Wave meets the first point absorber, (b): First point absorber radiates a circular wave due to its motion after absorbing energy from the incident wave, (c): Next point absorber that met by incident waves radiates circular waves itself.

an oscillating floating point absorbers. In Fig. 1.8 (a) the device moves in heave (up and down) and therefore generates symmetric plane waves propagating away from the oscillating body compared with Fig. 1.8 (b) where the device generates plane antisymmetric waves either through pitch or surge (back and forth) motion. Without the bodies movement the water surface would be calm. Fig. 1.8 (c) displays an incident ocean wave. Finally Fig. 1.8 (d) represents the superposition of the waves in (a), (b) and (c). In this case the incident wave would be absorbed completely, if the bodies oscillate vertically and horizontally in an optimal way. However, the three dimensional version of the problem is more complex, due to radiation in circular patterns known from Fig. 1.7, wherefore it is not possible to cancel a plane wave completely. This behavior is shown in Fig. 1.9 (c) together with the phenomenon of diffraction.

This diffraction occurs as well if incident (plane) waves meet objects. The manner how a wave is diffracted is dependent on the body's geometry and strongly dependent
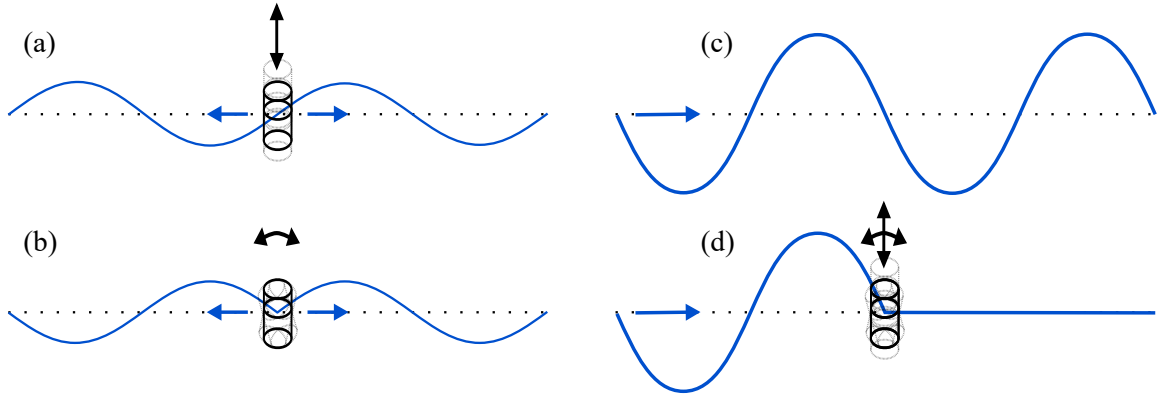
Figure 1.8: Wave generation and absorption by floating bodies, adapted from [16]: (a): Symmetric wave generation employing oscillating heave motion of a straight array, (b): Antisymmetric wave generation, (c): Undisturbed incident ocean wave, (d): Superposition of (a),(b) and (c), which illustrates the entire absorption of the incident wave.

on their number and arrangement. One of the main parts responsible for the excitation of other bodies are the diffracted waves, wherefore it is important to take them into account while designing the array configuration. Certain arrangements can lead to a constructive interaction hence an average higher excitation force usable in energy conversion whereas the opposite can be the case as well due destructive interaction. In [39] the authors study the dynamic performance of distinct array configurations taking the interactions between the devices into account and their results are used to illustrate several different diffraction cases. In Fig. 1.9 the dimensionless elevation due diffraction of the water surface around one and two cylindrical bodies is shown in (a) and (b), respectively. In Fig. 1.9 (c) the effects of radiation are taken into account in addition to the diffraction for the two point absorbers.
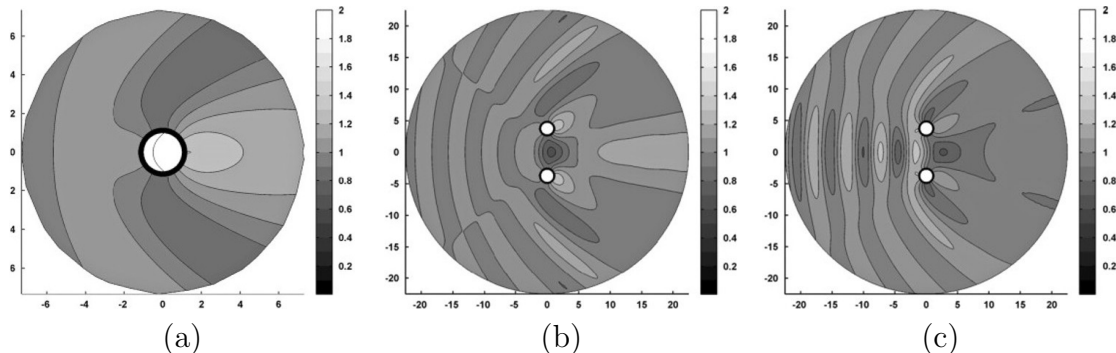
Figure 1.9: Wave diffraction around cylindrical bodies, (a): Single cylinder, (b): Two cylinders in a line, (c): Two cylinders in a line with simulated radiation in addition to the diffraction [39]

1.2.3 Hydrodynamic Fundamentals

A body immersed in water either with unsteady motion or with unsteady flow around it experiences additional effects from the fluid acting on it. Those effects are described after Falnes example [16]. The motion of the submerged body results in motion (flow) of the surrounding water. A part of the energy is radiated away from the body, called the radiated power

$$P_r = \frac{1}{2} R_r v^2. \tag{1.19}$$

Here R_r denotes the radiation resistance, depending on the geometry and v the velocity of the object. However, another part of the energy is stored instead. On the one hand, in kinetic energy due to the velocity of the water and, on the other hand, as potential energy caused by the deformation of the water surface. This energy is transferred to the mechanical system itself. The difference between the average values of added kinetic energy and the added potential energy is related to the so

called added mass, which is usually positive. However, there are exceptional cases leading to a larger added potential energy compared to kinetic energy and therefore a negative added mass. The added mass is frequency dependent and will be referred to with $A(\omega)$. For time domain simulations or equations of motion, the added mass for $\omega \to \infty$ is used to have weight added to the system (in a physical way) and denoted A^∞. An easy example is found in the lecture notes [55]. Under the assumption of small motions and linear behavior a floating body is modeled as a basic mass-spring-damper with displacement x, mass m, spring coefficient k and damping coefficient d, i.e.

$$m\ddot{x} + d\dot{x} + kx = f(t). \tag{1.20}$$

Here $f(t)$ stands for an external force acting on the mass. Now assuming an acceleration / deceleration in water and the following movement of the surrounding fluid results in an added mass force $-A^\infty \ddot{x}$ on the right hand side of the equation. A rearrange yields,

$$(m + A^\infty)\ddot{x} + d\dot{x} + kx = f(t). \tag{1.21}$$

With this example, it can be shown that the added mass changes the natural frequency ω_{system} of the system, namely

$$\omega_{\text{system}} = \sqrt{\frac{k}{m + A^\infty}}. \tag{1.22}$$

Consequently the knowledge of the added mass is inevitable to simulate a floating device, although the derivation is non trivial for shapes deviating from basic geometries

and require the use of sophisticated software solutions to calculate the values.

1.3 Ocean Wave Energy Conversion

The earliest patent was obtained by an engineer in Belfast, working on the Wells turbine. It was filed in 1799 in Paris by Mr. Girard and his son [48]. Fascinated by the force that the ocean can exert on ships, he imagined a lever connecting a vessel and mechanical devices like pumps or directly to mills. At this time, nobody thought about extracting electricity from renewables. The history of the rise of wave energy conversion in the 70s and continuing years is reviewed in [12]. The oil crisis of 1973 raised the interest in large-scale energy production from the waves. After his wife told Stephen Salter, of the University of Edinburgh, he should solve the energy crisis [48], he published a paper in the prestigious journal *Nature* in 1974, which brought wave energy to the attention of the international scientific community. In 1976 and 1978 the first conferences on wave energy took place in England and one year later two genuinely international conferences in Edinburgh and Gothenburg. The activities in the following years remained mainly at the academic level because of the theoretical difficulty of the diffraction and radiation wave phenomena in the hydrodynamic process of wave energy absorption. A further difficulty is related to the design of the power take-off module (PTO) (air turbine, hydraulics, electrical generator and others) due to the variability of the absorbed energy flux in several time scales: wave-to-wave (seconds), sea states (hours and days) and seasonable variations. This (largely random) variability is considered as the main disadvantage of

wave power, however, characterization of the wave climate had been done before for navigation and harbor, coastal and offshore engineering, hence this knowledge is used for the assessment of the wave energy resource and the conception of the individual wave energy converter (WEC).

1.3.1 Types of Wave Energy Converters

Generally it can be said "A good wave absorber must be a good wave-maker", Falnes [16]. However, the dependency on the water depth and the location on-, near- or offshore (Fig 1.2) leads to a variety of distinct devices, unlike the common large wind turbines, to exploit the existing condition at the area of application optimally. Currently, it is estimated that around 150 WECs have been reported at a global scale [50]. Depending on their location, working principle, mooring configuration, or size a WEC can be placed in various categories. Different authors use different names and allocations. The classification cannot be distinct in consequence of commonalities and overlapping. The authors of [50] use the following categories according to the working principle: point absorbers, attenuators and terminators. A point absorber is similar to a buoy which captures energy from all direction at one point and can either be floating or completely submerged. An attenuator is usually orientated with the wave direction and generates energy through motion of floaters relative to each other. Fig. 1.10 (b) shows a photograph of the Wave Star attenuator, where the floaters on the left hand side transfer the motion of the waves through the levers to the hydraulic cylinder PTO. Terminators act as breakwaters, but in contrast to fixed breakwaters

in harbors the terminators do not reduce the waves intensity through dissipation, instead the water will be concentrated into a higher reservoir and released through a hydro turbine. This operation principle is illustrated in the top part of Fig 1.10 (c). In the bottom part of this figure the Wave Dragon terminator with his two reflectors, to lead the waves to the overtopping reservoir, is photographed. In addition, the oscillating water column (OWC) has to be mentioned. Falcão and Henriques give a introduction to OWCs in [14]. A OWC device has a semi-submerged chamber open to the sea and the atmosphere. The waves alternately raise and lower the level of the inner free-surface of the water which leads to a pressure change in the chamber, that forces an airflow, running a turbine connected to a generator. In Fig. 1.10 (a) a concept of a OWC, fixed to e.g. a breakwater, is illustrated.

(a)　　　　　　　　　(b)　　　　　　　　　(c)
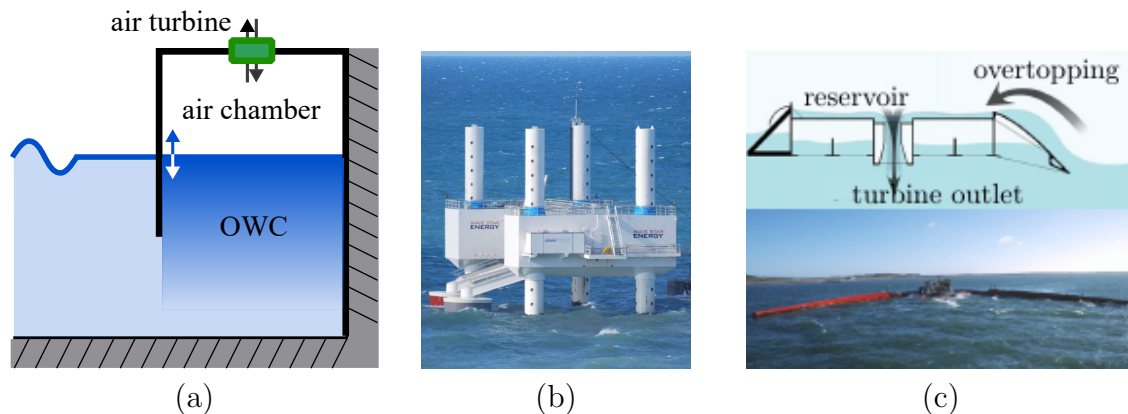
Figure 1.10: Types of Wave Energy Converters: (a) Concept of a fixed OWC, (b): Attenuator - Wave Star [37], (c): Terminator - Wave Dragon [56]

The main advantage of the OWC compared to most other WECs is its simplicity: The only moving part of the PTO is the rotor of a turbine, which is located above the water level. Hence, OWCs are a major class of wave energy converters, possibly

with the largest number of patents so far deployed into the sea.

1.3.2   Control of Wave Energy Converters

In addition to new pathways, wave energy researchers continue to find ways to drive down costs, improve performance, and ensure safety, reliability, and acceptability of grid-scale devices. Control design has long been and continues to be one of the primary areas of research for reaching those goals [16]. The purpose of the control algorithms is almost always to maximize energy absorption from the incoming waves, subject to the WEC dynamics and the physical limitations of the device and the actuators [20]. Recently, there has been a drive to reduce algorithm complexity by, for example, avoiding excitation force estimation or forecasting and circumventing online numerical optimization, both of which require complex computations by the controller at every time step [47]. Another challenge are times when the wave resource exceeds the rated device power. For example in wind turbines, this is dealt with by blade pitch control to the shed power [3]. For WECs shedding strategies would strongly dependent on archetype [47]. One type of WEC where such strategies are possible are oscillating water column (OWC) WECs, by closing an additional valve [31]. However, there is a gap in WEC control research that addresses multiple challenges at once, with easy frameworks, that can be transferred to different WEC archetypes.

1.4   Marmok-A-5 floating OWC

This floating oscillating water column is one of the simplest WEC and the most basic form consists of a long vertical tube, open at both ends. In a report from the British Department of Trade in 2005 this first concept of a Spar-buoy type WEC is considered the most promising, regarding reliability and economic value compared to other floating OWCs for energy generation [9] The first concept the Marmok-A-5 type follows that scheme and is illustrated in 1.11 (a). In comparison to a fixed OWC, the air chamber moves as well (predominantly in heave) due to the buoyancy through waves and the oscillation of the entire structure radiates new waves (see Sec. 1.2.2). However, the whole body's movement is designed to be out of phase with the water column [9], whereby the length of the tube determines the resonance frequency of the OWC. Oceantec, the company that developed the Marmok-A-5 successfully deployed a full scale prototype of the Marmok-A-5 in 2016 (see Fig 1.11 (c)). The dimensions of the floating OWC can be understood with the people in the foreground in Fig 1.11 (b).

So far only a single MARMOK has been deployed, thus this work models arrays later on. In Fig. 1.12 two identical MARMOKs are sketched to scale, with a separation distance of 30 m. In this sketch also the air chamber and the rectifying air turbine on top are illustrated, which are discussed in the next section.
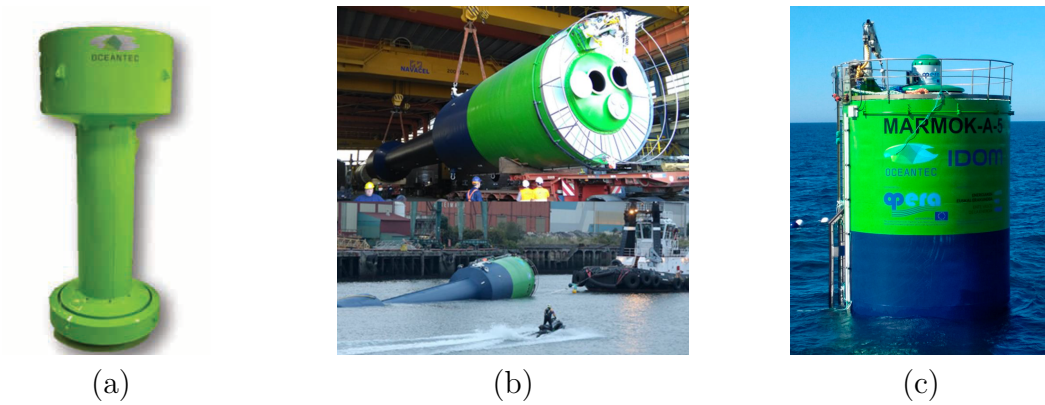
Figure 1.11: OWC Marmok-A-5. (a) First concept [10], (b) Photograph of the full scale Marmok-A-5 device while manufacturing and deployment [10], (c) Deployed Marmok-A-5 equiupped with the biradial turbine [57].

1.4.1 Rectifying Air Turbines

As mentioned before, the reason for the simplicity of the OWC is the rotor of the turbine being the only moving part. However, the concepts are not that trivial and again there is no prevailing one over the years, wherefore the history and different turbines are reviewed in [14]. The alternating airflow requires either the use of rectifying valves, which are regarded as impractical in large devices but work, for example, in small navigation buoys or self-rectifying turbines, i.e. the rotation direction remains the same regardless of the airflow direction. Most of those self-rectifying turbines are axial flow machines of two basic types: the earlier mentioned Wells turbine and the impulse turbine. The Wells turbine, invented in 1976, is the most popular one, even though impulse turbines are common alternatives, which also have been studied, tested and used.

The presented characteristics and illustrations of the Wells turbine originate from
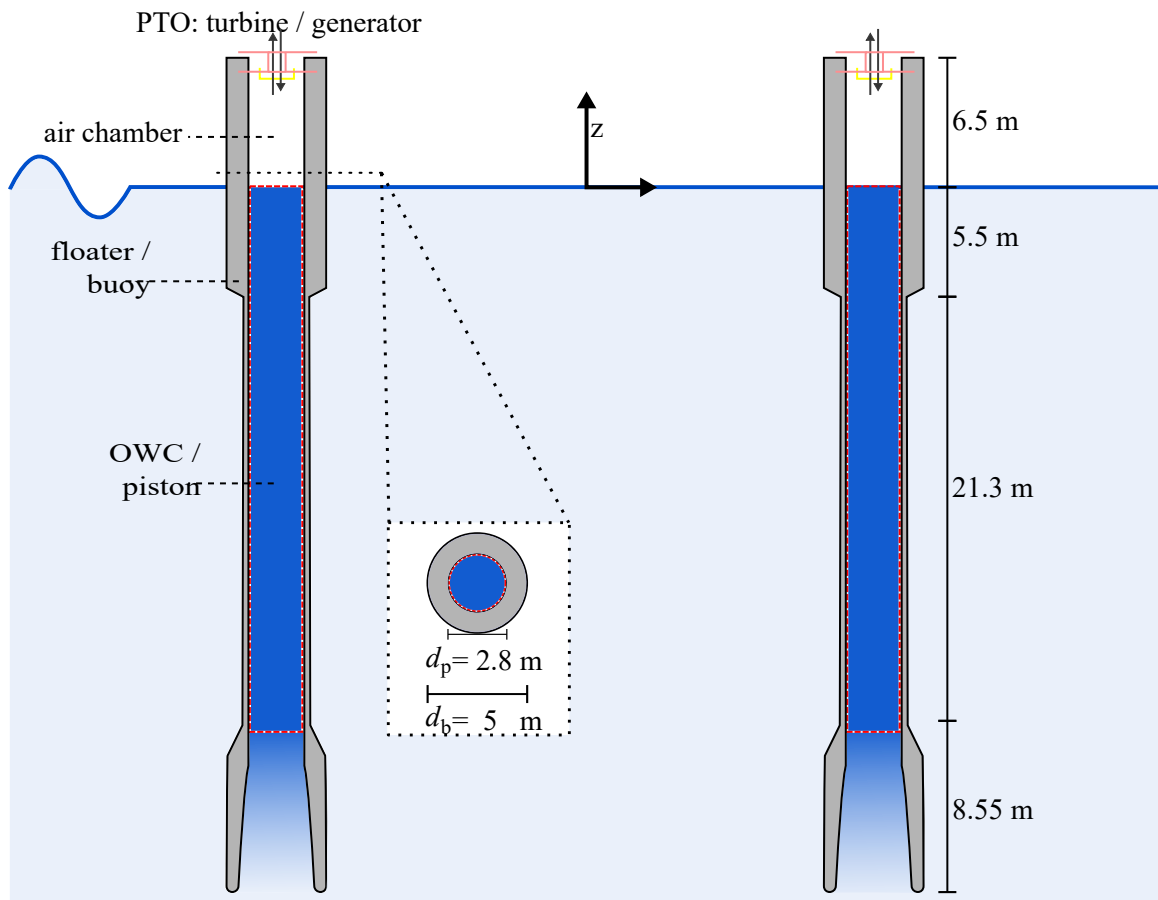
Figure 1.12: Sketch of two Marmok-A-5 devices. Figure is to scale.

the lecture notes from [49]. The symmetrical profile of the rotor blades is determining for the capability to rectify the in - and outflow. Additionally, a high circumferential velocity is necessary, illustrated in Fig. 1.13 (a) with u to guaranty the uplift force on the rotor blade. The dotted lines stand for the forces and flow velocities for an inflow and the solid lines for an outflow, respectively. v is the the actual velocity of the alternating airflow. w is the the relative velocity through addition of u and v, leading to lift and the drag on the airfoil. The orthogonal part of the total force on

the rotor blade F_u is the force which maintains the rotational speed of the turbine and it is independent of the flow direction. In the front part of the photograph Fig.
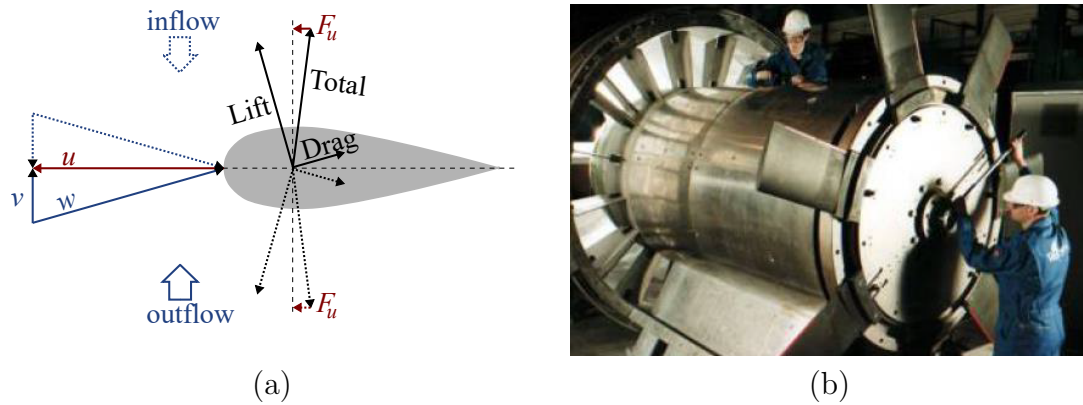
Figure 1.13: Wells turbine. (a) Sketch of the rotor blade profile and the prevailing flows and forces, (b) Photograph of the Wells turbine [49].

1.13 (b), the symmetrical rotor blades of the Wells turbine are shown. On the one hand, the hub is large to fit a generator inside, on the other hand, the circumferential velocity close to the hub is lower compared to the tips of the rotor blades, which can lead to flow separation, inducing changes in the lift and drag. The high velocities and the flow separation can produce a high noise level, which is a common problem of all air/gas turbines, especially if the WECs are deployed on the shore line or near shore [14]. In [54] the authors conduct a study on the noise characteristics of several self-rectifying turbines and conclude that impulse turbines have an advantage over Wells turbines.

A new impulse turbine is the biradial turbine introduced in [15] and appears to be the best choice in terms of performance. This turbine is illustrated in Fig. 1.14 and is symmetric with respect to a plane vertical to its rotation axis. The name comes

from the radial flow into and out of the central rotor, which is shown in Fig. 1.14 (b) for both directions. The flow into the rotor is directed through guide vanes. There
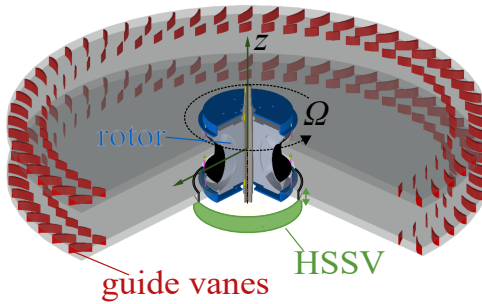
Figure 1.14: Biradial turbine with fixed guide vanes and the High Speed Stop Valve added around the rotor. Adapted from [5].

are two distinct connected rows of guide vanes, illustrated in blue in the figure. By sliding the complete guide vanes set axially, the guide vanes can be inserted into or removed from the flow to ensure that the downstream guide vanes do not obstruct the flow out of the rotor. The peak efficiency is about 79 % and is probably the highest ever measured of a self-rectifying air turbine [14]. Therefore, the biradial turbine is the choice for this work.

Other concepts are not further pursued, but there are more. For example, two identical unidirectional air turbines are joined in parallel, such that most of the flow is admitted to one turbine with a good efficiency, while the other turbine is in choking mode. Those turbines can either be connected to one generator or each run their own generator or conventional unidirectional flow turbines (e.g. Francis turbine) equipped with rectifying systems [14].

1.5   Wave to wire models

Control of WECs has often been focused on hydrodynamic control to absorb the maximum energy possible from ocean waves. This generally significantly simplifies the performance of real power take-off (PTO) systems [42]. A downside of hydrodynamic WEC control might be a decrease in the power quality, in terms of the peak-to-average-power ration. This makes it more difficult to meet the standards for marine energy grid integration. In order to simulate the effects all the way through the power conversion chain, namely, from waves to device over PTO and power electronics up to an electric network, need to be included in the dynamic model. Such models are referred to as wave-to-wire models. However, including all the required dynamics and constraints in the control problem may considerably vary the control strategy and the power output [42].

1.5.1   Arrays of Wave Energy Converters

To efficiently harvest high amounts of wave energy, it is imperative to deploy multiple WECs in an array configuration. Therefore, it is possible to capture a wider section of a plane incident wave (see Fig.1.8). An introduction and factors that influence the array layout are given in [60] and [8], respectively. In 1977 Budal was the first to investigate the theory of power absorption of arrays coming up with the concept of the interaction factor $q(\theta) = P_{N,max}/(N \cdot P_{1,max})$ which is defined as the ratio between the produced power by an array to the power produced by the same amount of single (isolated) devices. This interaction factor is dependent on the incident wave angle

θ, and strongly on the wave period and the placement of the devices [16] (although the q factor is less dependent on the period in irregular waves (Sec. 1.2.1) and is observed in Sec. 4.3. Note that As stated in section 1.2.2, the interaction between radiated and diffracted waves can either be constructive or destructive, wherefore the placement can lead to $q > 1$, or $q < 1$, respectively, for the interference inside the array. In [8] the authors study the influence of the separation distance d_s, the wave directionality, the number of WECs on different array layouts, which are illustrated in Fig. 1.15. Configuration (a) represents a class of linear layouts consisting of three or four bodies. The standard three body configuration is a equilateral triangle (Fig 1.15 (b)). The base of the Rhombus configuration (Fig. 1.15 (c)) is an equilateral triangle with an additional WEC with the same distance to the others. The triangle also find itself in the Hexagon with central WEC configuration (Fig. 1.15 (d)), as first suggested by Vicente et al. [58]. The authors vary the incident wave angle from
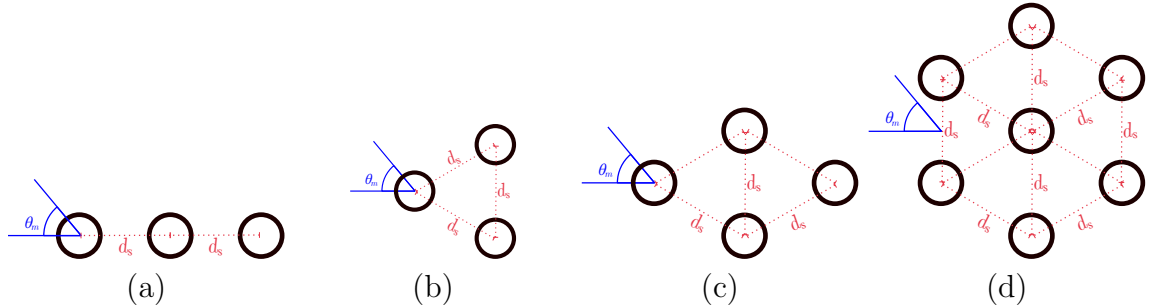
Figure 1.15: Different Arrays Layouts. (a): Linear, (b): Triangle, (c): Rhombus, (d): Hexagon.

$0°$ to $90°$, wherefore the linear array (a), for example, changes from an attenuator to a terminator (see Sec. 1.3.1) and reaches the same orientation to the waves like in Fig. 1.8, hence, theoretically, an entire absorption of the part of the wave crest is

possible, but the research group limits the simulation to the dominant heave motion. The variation in the distance is orientated to the wave length corresponding to the wave period on which the devices are tuned. In general a 180° delay in phase is achievable [8]. The linear array was found to have the worst q factor in contrast to similar efficiencies for the triangular and the squared configuration depending on the wave climate. However, for multi-directional waves the equilateral triangle is the optimal configuration [8] and therefore used for preliminary investigations in the thesis. The main body of this work is concerned with a park of seven WECs placed in a hexagon with a central WEC Fig. 1.15 (d). This configuration should retain the good performance in multi directional waves. For the determination of the spacing other non-hydrodynamic factors as electrical cabling, size restriction and mooring cost can be important as well. Therefore, in this work a distance smaller than the optimal one for reaching the 180° delay in phase is chosen. Another benefit of park deployment is that the WECs have their power peaks at different instances in time and if the WECs are electrically connected the park power is naturally smoothed among the power network.

1.6   Summary

Ocean wave energy is a vast, nearly untapped renewable energy resource. But, the development of wave energy converters is challenging and complicated due to the harsh ocean environment and consequently associated with a high price tag. Dynamic simulation models should be used for cheap and material free investigations of the

WEC performance and potential strategies to improve the performance and guarantee a safe operation.

Chapter 2   Dynamic Model

Generally, dynamic models simplify a real world process while trying to reproduce the essential features. Commonly, the simulation of dynamic models is conducted in the time domain, although in wave energy research it is not unusual to simulate dynamic equations in the frequency domain, if the made assumptions justify linear relations between the properties of the system. The amount of detail desired in this work requires nonlinear effects and consequently a time domain simulation model. However, for some features of a system, e.g. the transition between two distinguishable operating regions, the continuous dynamics between the instances of time are irrelevant. The occurrence of such a transition is called event and is observed when looking at the system from a higher level. The next section describes the general approach on how to model a floating OWC, followed by the description of the quantities storing energy and their conservation in Sec. 2.1.1. The concept of energy carrying states and the definition of the states for a park of $N = 7$ WECs are described in Sec. 2.1.3, followed by the acting forces in Sec. 2.2. The next stage in energy conversion chain, namely, the electric energy conversion, is modelled in terms of the power flow between the WECs in the park and an energy storage unit up to the power grid, described in Sec. 2.3. In Sec. 2.1.2 the forces and state variables are combined to express the model in a state space representation, functioning as the time domain simulation model.
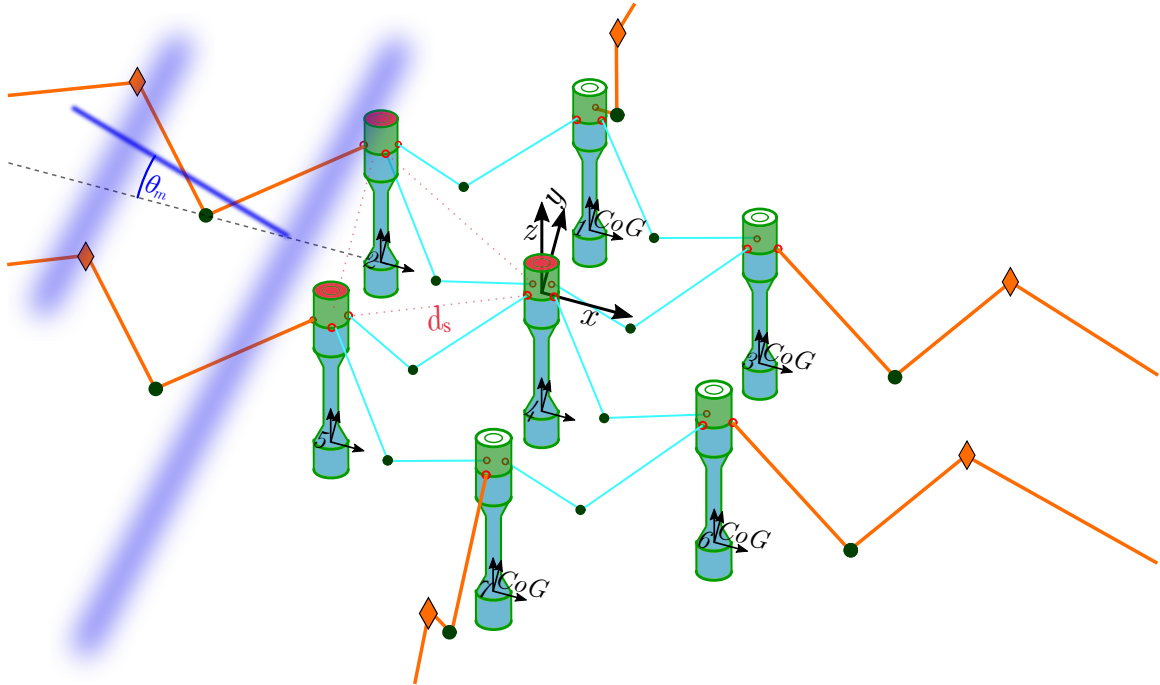
Figure 2.1: Sketch of the floating OWC WEC park configuration with minimum separation distance d_s between each WEC, exposed to a plane incident wave field at angle θ_m. The inter body mooring lines are illustrated in cyan and the bottom mooring lines in orange. Note that the end of the anchors of the bottom mooring lines are not illustrated and the sketch is not perfectly to scale.

2.1 Modeling Approach

A Portuguese research group at the University of Lisbon extensively researches floating OWC devices. The first principle approach to derive the main dynamic equations of a single floating OWC is inspired by the work of that group, e.g. [13, 24, 31]. A floating OWC WEC is considered a two body heaving system, with the first body representing the buoy and the second body is the full oscillating water column. The inner free surface is approximately level, since the incident ocean wave length is much

greater than the buoy's inner diameter. Therefore, the OWC is represented by an imaginary rigid piston, indicated with superscript ^{p}. The two body system enables us to use oscillating body theory to describe the interactions between buoy and piston. Related is the assumption of small wave amplitudes and body motions to apply linear water wave theory which enables the application of linear hydrodynamic interactions. Practical corrections are made with nonlinear forces to mitigate the limitations of the linear approach, such as the viscous drag force, mooring force and the nonlinear force connecting the buoy and its water column due to the air pressure inside the chamber. The latter force is another of the interactions between the two bodies, acting in opposite direction on the buoy and the piston. When computing the change rate of the pressure the air compressibility is taken into account.

The pressure in the air chamber is mostly affected by the relative heave motion between buoy and piston, which makes the heave motion the main driver for power conversion from kinetic power (ocean waves and body motion) to pneumatic power (air pressure). To a smaller extent, the heave motion is influenced by motion in other degrees of freedom (DoFs). However, the other dynamics in other DoFs are mostly of interest for the overall motion of the WEC park, such as drifting and the interactions due to a shared mooring system.

The aim of this work is a holistic simulation model for an OWC park, consequently all buoy DoFs are considered together with the heave position of the imaginary rigid piston. Let us use a right-handed Cartesian coordinate system to describe the spatial state of the WECs. A positive heave displacement $z(t)$ is defined to be upwards and $z(t) = 0$ is at the calm ocean surface. The positive surge axis x shall point

towards the shore, as illustrated in Fig. 2.2. The rotations about the surge x, sway y and heave z, roll, pitch and yaw, shall be denoted r^x, r^y, r^z, respectively. The heave position of the piston shall be denoted $z^{\mathrm{p}}(t)$. To express the dynamics of a WEC a body fixed reference $(\hat{x}, \hat{y}, \hat{z}, \hat{r}^x, \hat{r}^y, \hat{r}^z, \hat{z}^{\mathrm{p}})$ should be used, since the inertial properties of the WEC remain constant in time in this frame [21]. The origin of
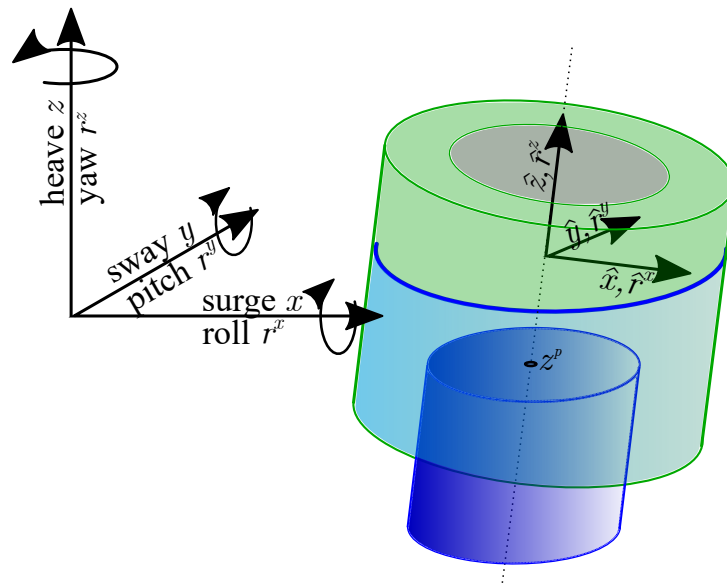
Figure 2.2: Arbitrarily displaced and simplified buoy with body coordinate frame $(\hat{x}, \hat{y}, \hat{z})$ and rotations $(\hat{r}^x, \hat{r}^y, \hat{r}^z)$ and OWC piston heave position z^{p}, in world coordinate frame (x, y, z), with corresponding rotations (r^x, r^y, r^z). Note: The origin of body coordinate frame (^) equals the bodies CoG, which is not represented in the figure.

the body fixed frame is defined to be the center of gravity (CoG) of the respective body. For every DoF Newton's second law is used as basis for the equations of motion (Sec. 2.1.2). Namely, that the change rate of the momentum equals the sum over all

acting forces/torques,

$$m\dot{v} = \sum F. \tag{2.1}$$

2.1.1 Energy Conservation in OWC WECs

For the representation of the floating OWC i in terms of dynamical equations its components need to be abstracted. In Fig. 2.3 the main components, namely, the WEC with buoy and piston and the PTO with turbine and generator are illustrated. The air chamber is the interface between WEC and the PTO. Starting from the left
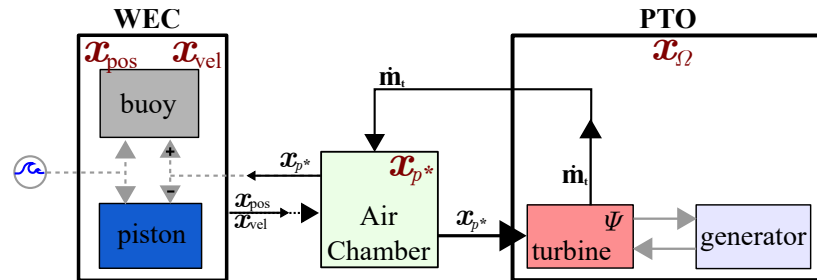
Figure 2.3: Components of the floating OWC with the state variables, representing the quantities capable of storing energy in the system.

in the figure, let us assume an ocean wave brings buoy and piston into motion, thus wave energy is converted into potential and kinetic energy. Relative motion between buoy and piston changes the volume of the air chamber, but the same amount of air is trapped, assuming the air has not left through the turbine yet. This means that the potential and kinetic energy is conserved in the chamber's air pressure. Now, this air pressure accelerates the turbine/generator set and consequently the energy is converted into rotational (kinetic) energy, which will then be converted into electrical

energy by the generator opposing the turbine. Let us assume that all the WECs $i \in [1; 7]$ are connected electrically, including a single energy storage (ES) unit in the link. The ES stores energy in form of chemical potential energy.

2.1.2 State Space Representation

To describe properties of a system the description with variables known as state variables is used often. Common practice is to define quantities that are capable of storing energy in a system as the states, e.g. positions, velocities and pressures, contained in vector $\boldsymbol{x}(t)$. The dynamic equations are a set of equations or rules specifying how those state variables change over time, as a function of the current and past values of the state variables, control inputs $\boldsymbol{u}(t)$, and uncontrollable inputs, such as the ocean waves vector $\boldsymbol{w}(t)$, namely,

$$\dot{\boldsymbol{x}}(t) = f\big(\boldsymbol{x}(t), \boldsymbol{u}(t), \boldsymbol{w}(t)\big) \tag{2.2}$$

This is the standard nonlinear state space representation and it is required when $f()$ contains nonlinear relations between the states. In the real world most relations are nonlinear and in this work pressure dynamics (Sec. 2.2.6), mooring (Sec. 2.2.3) and viscous drag forces (Sec. 2.2.7) need to be modelled nonlinearly to accurately model those effects. The control inputs $\boldsymbol{u}(t)$ require actuators in the physical system, but can be used to alter the dynamics of the system. Commonly, control researchers use the knowledge of the system contained in (2.2) to design the control inputs (Chap.

6). Let us assume that all states can be measured directly, since the necessary sensors are common and consequently the output equation is trivial.

If the dynamics can be adequately modeled with linear time invariant relations the widely known linear state space form is a special case of (2.2), namely

$$\dot{\boldsymbol{x}}(t) = A\boldsymbol{x}(t) + B\boldsymbol{u}(t) \tag{2.3}$$

$$\boldsymbol{y}(t) = C\boldsymbol{x}(t) + D\boldsymbol{u}(t) \tag{2.4}$$

Here $\boldsymbol{y}(t)$ denotes the systems outputs and A denotes the system dynamics matrix, B the input distribution matrix, C the output distribution matrix and D the input feed through matrix. in this work the linear state space form is used to model the memory effect of the radiation force due the past device motion and the resulting radiation force (Sec. 2.2.5). The notation of the time dependency of the state and input variables is omitted in the rest of the thesis, but generally quantities indicated with x and u are time varying.

2.1.3 State Vector

The instantaneous value of the main energy storing quantities in WEC i will be used to describe the current system state x_i and for the overall park state vector $\boldsymbol{x}$ the ES state of charge (SOC) is included. Let us start with the position vector,

$$\boldsymbol{x}_{\mathrm{pos},i} = \begin{bmatrix} x_i & y_i & z_i & r_i^x & r_i^y & r_i^z & z_i^{\mathrm{p}} \end{bmatrix}^T, \tag{2.5}$$

and the velocity vector in the body frame,

$$\hat{\boldsymbol{x}}_{\mathrm{vel},i} = \begin{bmatrix} \dot{\hat{x}}_i & \dot{\hat{y}}_i & \dot{\hat{z}}_i & \dot{\hat{r}}_i^x & \dot{\hat{r}}_i^y & \dot{\hat{r}}_i^z & \dot{\hat{z}}_i^{\mathrm{p}} \end{bmatrix}^T.$$ (2.6)

The transformation from body frame into world frame is addressed in Sec. 2.2.1f. Let us concatenate the position and velocity vectors of the $N = 7$ WECs to the vectors,

$$\boldsymbol{\mathcal{X}}_{\mathrm{pos}} = \begin{bmatrix} \boldsymbol{x}_{\mathrm{pos},1} \\ \vdots \\ \boldsymbol{x}_{\mathrm{pos},N} \end{bmatrix} \in \mathbb{R}^{7N} \text{ and } \hat{\boldsymbol{\mathcal{X}}}_{\mathrm{vel}} = \begin{bmatrix} \hat{\boldsymbol{x}}_{\mathrm{vel},1} \\ \vdots \\ \hat{\boldsymbol{x}}_{\mathrm{vel},N} \end{bmatrix} \in \mathbb{R}^{7N}$$ (2.7)

The pressure in the air chamber is accounted for in the vector of the relative pressure difference

$$\boldsymbol{x}_{p^*} \in \mathbb{R}^N$$ (2.8)

The rotational speeds of the turbine-generator sets are contained in the vector

$$\boldsymbol{x}_\Omega \in \mathbb{R}^N$$ (2.9)

Lastly, the state of charge of the ES is denoted

$$x_{\mathrm{SOC}} \in [0, 1],$$ (2.10)

were $x_{\text{SOC}} = 0$ indicates an empty ES and $x_{\text{SOC}} = 1$ indicates a full ES. Finally, let us define the main state vector for WEC park with N WECs,

$$
\boldsymbol{x} = \begin{bmatrix} \boldsymbol{\mathcal{X}}_{\text{pos}} \\ \hat{\boldsymbol{\mathcal{X}}}_{\text{vel}} \\ \boldsymbol{x}_{p^*} \\ \boldsymbol{x}_{\Omega} \\ x_{\text{SOC}} \end{bmatrix} \in \mathbb{R}^{16N+1} \tag{2.11}
$$

This states space and control oriented notation is used through out the work to clearly indicate the dependency on a state variable for the derivation of the acting forces and later the control algorithms.

2.2   Acting Forces

The equations governing the dynamics of the system state $\boldsymbol{x}$ in (2.3) are mainly physical forces. Fig. 2.4 shows an expanded version of Fig. 2.3 which includes those forces and if the forces are a function of the state variables, their dependency is illustrated. The subscript $_i$ is dropped in the figure. Now, taking into account that the forces act along the time varying body axes, Equation (2.1) evolves to the Cummins equation [7], in the control oriented notation,

$$
\dot{\hat{\boldsymbol{x}}}_{\text{vel},i} = \boldsymbol{M}_i^{-1} \left(\boldsymbol{F}_i^{\text{H}} + \boldsymbol{F}_i^{\text{M}} + \boldsymbol{F}_i^{\text{PTO}} + \boldsymbol{F}_i^{\text{R'}} + \boldsymbol{F}_i^{\text{Ex}} + \boldsymbol{F}_i^{\text{VD}} \right). \tag{2.12}
$$
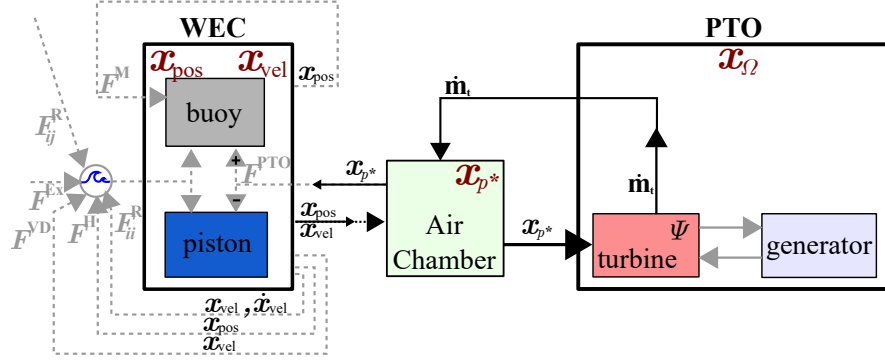
Figure 2.4: Components of the floating OWC with the state variables and the acting forces.

Here $\boldsymbol{M}_i^{-1}$ denotes the inertia matrix, containing the physical device mass, the moment of inertia about the respective axis and the added mass components in all DoFs. Consequently, $\boldsymbol{M}_i^{-1}$ yields body i to body i interactions. The considered generalized forces vectors $\boldsymbol{F}_i$ on WEC i are composed of a linear force vector and rotational torque vector. The following forces will be further derived in the ensuing sub-sections.

$\boldsymbol{F}^{\mathbf{H}}$ The hydrostatic restoring force vector, adding a spring like effect in some DoFs (Sec. 2.2.2).

$\boldsymbol{F}^{\mathbf{M}}$ The mooring force vector due to mooring connection with the sea floor and the inter body moorings (Sec. 2.2.3). No mooring is connected to the imaginary piston.

$\boldsymbol{F}^{\mathbf{Ex}}$ The excitation force vector accounts for all incident waves on the body and it results from solving the diffraction problem (Sec. 2.2.4).

$\boldsymbol{F}^{\mathbf{R}}$ The radiation force vector includes interactions from the motion of other bodies in the park. It results from solving the radiation problem, approximated with

a linear state space model (Sec. 2.2.5).

$\boldsymbol{F}^{\mathbf{PTO}}$ The force vector due to the pressure change in the chamber induced by the turbine/generator dynamics. It is acting in opposite direction for buoy and OWC (Sec. 2.2.6).

$\boldsymbol{F}^{\mathbf{VD}}$ The viscous drag force vector based on the common assumption of a constant drag coefficient following the semi-empirical Morison equation (Sec. 2.2.7).

2.2.1   Coordinate Transformation

The forces and velocities act along the time varying axes in the body coordinate frame, while the displacements are given in the fixed world frame [21] (compare Fig 2.2). In linear hydrodynamic models there is no difference between the two frames, but since nonlinearities are considered in all DoFs, the linear mapping $\boldsymbol{J}_{r,i}$ is used at every time step to correct for the translations and rotations between body frame (ˆ) and world reference frame, namely

$$\boldsymbol{x}_{\mathrm{vel},i} = \boldsymbol{J}_{r,i} \underbrace{\begin{bmatrix} \hat{x}_i & \hat{y}_i & \hat{z}_i & \hat{r}_i^x & \hat{r}_i^y & \hat{r}_i^z & \hat{z}_i^{\mathrm{p}} \end{bmatrix}^T}_{\hat{\boldsymbol{x}}_{\mathrm{vel},i}}, \tag{2.13}$$

with

$$\boldsymbol{J}_{r,i} = \begin{bmatrix} \boldsymbol{R}_{r,i}(r_i^z, r_i^x, r_i^y) & \boldsymbol{0}^{3\times3} & 0 \\ \boldsymbol{0}^{3\times3} & \boldsymbol{T}_{r,i}(r_i^z, r_i^x, r_i^y) & 0 \\ \boldsymbol{0}^{1\times3} & \boldsymbol{0}^{1\times3} & \cos r_i^y \cos r_i^x \end{bmatrix}. \tag{2.14}$$

Here $\boldsymbol{R}_{r,i}$ is the intrinsic rotation matrix about r_i^z, r_i^x, r_i^y and applied to the transnational velocities,

$$\boldsymbol{R}_{r,i} = \begin{bmatrix} \cos r_i^z & -\sin r_i^z & 0 \\ \sin r_i^z & \cos r_i^z & 0 \\ 0 & 0 & 1 \end{bmatrix} \begin{bmatrix} \cos r_i^y & 0 & \sin r_i^y \\ 0 & 1 & 0 \\ -\sin r_i^y & 0 & \cos r_i^y \end{bmatrix} \begin{bmatrix} 1 & 0 & 0 \\ 0 & \cos r_i^x & -\sin r_i^x \\ 0 & \sin r_i^x & \cos r_i^x \end{bmatrix} \quad (2.15)$$

The rotation,

$$\boldsymbol{T}_{r,i} = \begin{bmatrix} 1 & \sin r_i^x \tan r_i^y & \cos r_i^x \tan r_i^y \\ 0 & \cos r_i^x & -\sin r_i^x \\ 0 & \sin r_i^x / \cos r_i^y & \cos r_i^x / \cos r_i^y \end{bmatrix} \quad (2.16)$$

is applied to the rotational velocities. The last entry of (2.14) governs the pistons heave velocity inside the potentially rotated WEC.

2.2.2   Hydrostatic Restoring Force

The spring like effect of the hydrostatic restoring force acts in heave, roll and pitch, but not in the other DoFs [40]. In matrix form for WEC i this yields,

$$
\boldsymbol{F}_i^{\mathrm{H}} = \begin{bmatrix}
0 & 0 & 0 & 0 & 0 & 0 & 0 \\
0 & 0 & 0 & 0 & 0 & 0 & 0 \\
0 & 0 & -\rho_{\mathrm{w}} g S_{\mathrm{b}} & 0 & 0 & 0 & 0 \\
0 & 0 & 0 & -\rho_{\mathrm{w}} g V_{\mathrm{b}}\overline{GM} & 0 & 0 & 0 \\
0 & 0 & 0 & 0 & -\rho_{\mathrm{w}} g V_{\mathrm{b}}\overline{GM} & 0 & 0 \\
0 & 0 & 0 & 0 & 0 & 0 & 0 \\
0 & 0 & 0 & 0 & 0 & 0 & -\rho_{\mathrm{w}} g S_{\mathrm{p}}
\end{bmatrix}
\begin{bmatrix}
x_i \\
y_i \\
z_i \\
r_i^x \\
r_i^y \\
r_i^z \\
z_i^{\mathrm{p}}
\end{bmatrix}
\tag{2.17}
$$

Here, ρ_{w} is the ocean water density, g is the gravity acceleration, and V_{b} denotes the volume of water displaced by the buoy. The annular cross section of the buoy is denoted S_{b} and S_{p} denotes the inner cross-sectional area of the piston. The metacentric height $\overline{GM}$ at rest is used, assuming that the body motion is less than $\overline{GM}$. For more detailed studies of the WEC motion and its stability in extreme conditions, the instantaneous GM should be taken into account. It varies with the instantaneous position of the device, directly affecting the center of buoyancy of the spar. If the GM becomes negative, the motion becomes unstable, decreasing the extracted power, since kinetic energy is transferred from the the heave mode to the pitch mode [46]. Those phenomena are a driver of parametric resonance.

2.2.3 Mooring Force

In this work a quasi-static mooring model is used to keep the WEC park from drifting away. A quasi-static model can capture some of the nonlinear mooring behavior, but neglects the line motion itself [25].
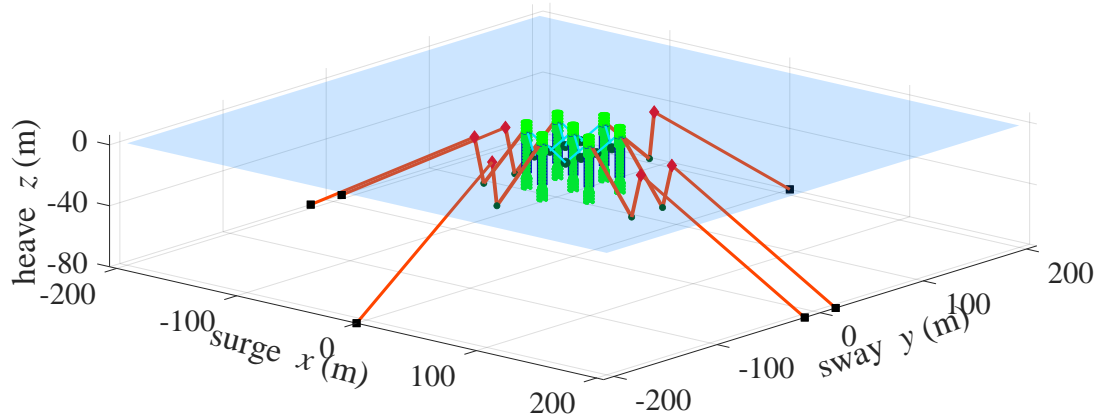
Figure 2.5: WEC park configuration at calm seat. Figure is to scale.

2.2.3.1 Bottom mooring

Six bottom mooring lines are connected to the outer WECs in the park, illustrated in Fig. 2.5. The tensions in every line are computed individually. The instantaneous tension in other mooring lines is irrelevant for the others, so that only the instantaneous positions of the respective fairleads, where a mooring line is connected to the buoy affect the tension and consequently the force on the buoy. Giorgi et al. present a compact description of the nonlinear equations to model a single bottom mooring

line [21]. Such a mooring line is illustrated in Fig 2.6 in orange. The bottom mooring
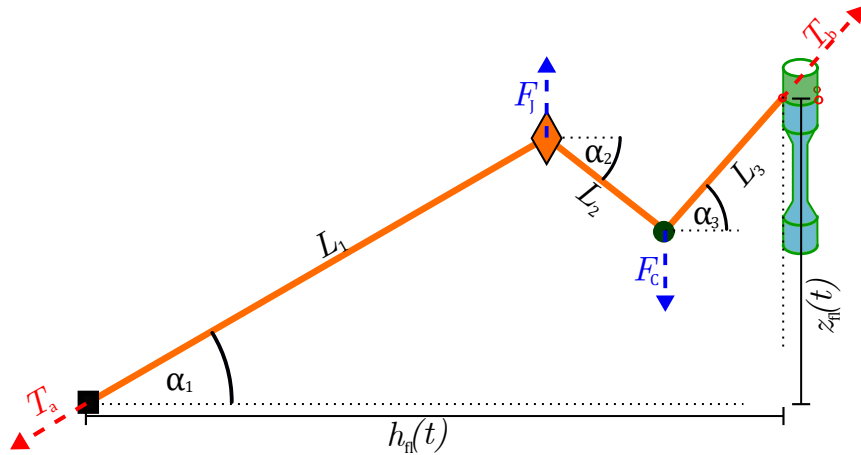
Figure 2.6: Single bottom mooring line projected in plane. Figure is not to scale.

line is composed of three straight lines, with lengths L_1, L_2, L_3, with weight per unit length w_L and a jumper (diamond) and clump weight (circle) in between. For simplicity, the mooring line is projected in a plane (square) cutting through the anchor and the buoy, so that the horizontal distance between the anchor and the fairlead $h_{fl}(t)$ can be used together with the vertical distance $z_{fl}(t)$ to numerically compute the tension of the cable at the buoy T_b and the anchor T_a. Let us restate the slightly recasted equation system [21], with the vertical and horizontal force balance

$$0 = T_b \sin \alpha_3 - w_L(L_1 + L_2 + L_3) - F_C + F_J - T_a \cos \alpha_1 \tag{2.18}$$

$$0 = T_b \cos \alpha_3 - T_a \cos \alpha_1. \tag{2.19}$$

Followed by a torque balance,

$$
\begin{aligned}
0 =& T_\mathrm{b} \cos \alpha_3 z_\mathrm{fl}(t) - T_\mathrm{b} \sin \alpha_3 h_\mathrm{fl}(t) \\
&+ w_\mathrm{L} \left[\cos \alpha_1 \left(\frac{L_1^2}{2} + L_1 L_2 + L_2 L3 \right) + \cos \alpha_2 \left(\frac{L_2^2}{2} + L_2 L_3 \right) + \cos \alpha_3 \frac{L_3^2}{2} \right] \\
&+ \cos \alpha_1 L_1 \left(F_\mathrm{C} - F_\mathrm{J} \right) + \cos \alpha_2 F_\mathrm{C},
\end{aligned}
\tag{2.20}
$$

and lastly two equations imposing geometrical constraints,

$$
0 = \cos \alpha_1 L_1 + \cos \alpha_2 L_2 + \cos \alpha_3 L_3 - h_\mathrm{fl}(t) \tag{2.21}
$$

$$
0 = \sin \alpha_1 L_1 + \sin \alpha_2 L_2 + \sin \alpha_3 L_3 - z_\mathrm{fl}(t). \tag{2.22}
$$

Here the unknowns $\alpha_1, \alpha_2, \alpha_3$ denote the angle between the respective line L_1, L_2, L_3 and the horizontal plane. The net weight force and net buoyancy force of the clump weight and the jumper are denoted F_C and F_J, respectively. In the time domain simulation, the system eqs. (2.18) to (2.22) is only solved every 0.1s to and hold the value to save computation time. The previous solution is used as initial guess for the nonlinear equation solver to further decrease the computation time.

2.2.3.2   Inter Body mooring

For an inter body (IB) mooring lines, two lines with the same length length L_IB and weight per unit length w_IB are assumed together with a single weight force F_IB between a buoy-buoy connection, illustrated in Fig. 2.7 [26]. The system of equations
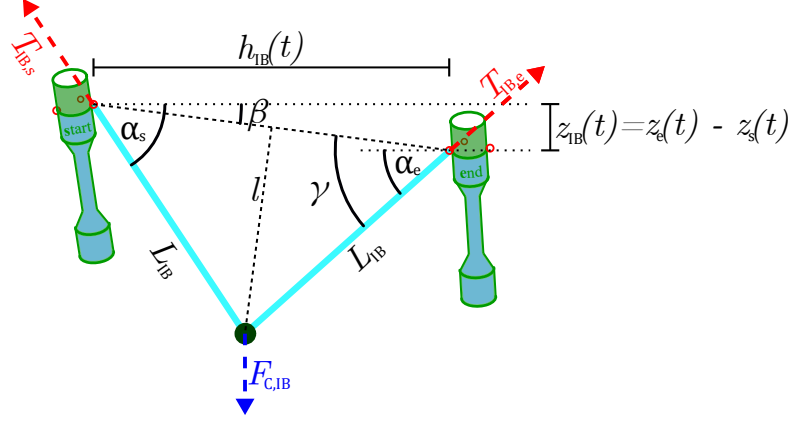
Figure 2.7: Inter body mooring line between two arbitrary displaced WECs projected into plane. Figure is not to scale.

is solved for the tensions at the start buoy $T_{\mathrm{IB,s}}$ and the tension $T_{\mathrm{IB,e}}$ at the buoy at the end of the IB mooring line. The vertical force and torque balance,

$$0 = - T_{\mathrm{IB,s}} \sin \alpha_{\mathrm{s}} - 2 w_{\mathrm{IB}} L_{\mathrm{IB}} - F_{\mathrm{C,IB}} + T_{\mathrm{IB,e}} \sin \alpha_{\mathrm{e}} \tag{2.23}$$

$$0 = - w_{\mathrm{IB}} \frac{L_{\mathrm{IB}}^2}{2} (3 \cos \alpha_{\mathrm{s}} + \cos \alpha_{\mathrm{e}}) - F_{\mathrm{C,IB}} \cos \alpha_{\mathrm{s}}$$
$$+ T_{\mathrm{IB,e}} \big(\sin \alpha_{\mathrm{e}} h_{\mathrm{IB}}(t) - \cos \alpha_{\mathrm{e}} z_{\mathrm{IB}}(t) \big) \tag{2.24}$$

are a function of the horizontal and vertical distance between the fairleads of two IB moored buoys $h_{\mathrm{IB}}(t)$ and $z_{\mathrm{IB}}(t)$, respectively. The torque balance is formulated about the starting buoy, indicated by subscript $_s$. Assuming that the IB lines do not change their length, the system of equations can be explicitly solved for the angles between

the lines and the horizontal α_s, α_e with trigonometry, namely

$$\begin{bmatrix} \alpha_s \\ \alpha_e \end{bmatrix} = \begin{bmatrix} \beta - \gamma \\ \beta + \gamma \end{bmatrix}, \tag{2.25}$$

with the angles

$$\beta = \tan^{-1}\left(\frac{z_{IB}(t)}{h_{fl}(t)}\right) \tag{2.26}$$

$$\gamma = \sin^{-1}\left(\frac{l}{L_{IB}}\right) \tag{2.27}$$

and the length

$$l = \sqrt{L_{IB}^2 - \frac{h_{IB}^2(t) + z_{IB}^2(t)}{4}}. \tag{2.28}$$

Consequently, let us isolate $T_{IB,s}, T_{IB,e}$ at the ends of the IB mooring lines in eqs. (2.23) and (2.24) and calculate them analytically, with

$$\begin{bmatrix} T_{IB,s} \\ T_{IB,e} \end{bmatrix} = \begin{bmatrix} -\sin\alpha_s & \sin\alpha_e \\ 0 & \sin\alpha_e h_{IB}(t) - \cos\alpha_e z_{IB}(t) \end{bmatrix}^{-1} \cdot$$

$$\begin{bmatrix} 2w_{IB}L_{IB} + F_{C,IB} \\ w_{IB}\frac{L_{IB}^2}{2}(3\cos\alpha_s + \cos\alpha_e) + F_{C,IB}\cos\alpha_s L_{IB} \end{bmatrix}. \tag{2.29}$$

Solving (2.29) directly yields a noticeable simulation time reduction, when compared to the equation system with eqs. (2.23) and (2.24) (which would require two additional

equations, e.g. the ones to impose geometrical constraints).

2.2.3.3 Line Tension in Body coordinate frame

The tensions of the mooring lines in the two previous subsections are currently given in the imaginary plane of the mooring line. To finally compute the mooring forces and torques, the tensions have to be transformed into the world and body coordinate system, respectively, at every mooring simulation step. The position of fairlead j from buoy i is given through,

$$\boldsymbol{p}_{\mathrm{fl},i,j}(t) = \mathbf{CoG}_i + x_{\mathrm{pos},i} + \boldsymbol{R}_{r,i}(r_i^z, r_i^x, r_i^y) \cdot \hat{\boldsymbol{p}}_{\mathrm{fl},i,j}, \qquad (2.30)$$

as a function of the instantaneous buoy displacement and the constant position $\hat{p}_{\mathrm{fl},i,j}$ of the fairlead j in the body coordinate frame. Note that the outer WECs have $j = 3$ fairleads, two for IB connections, one for the bottom mooring and the central WEC has $j = 4$ fairleads, all connecting to other WECs. Therefore, the indices are dropped in the following analysis, since the denotation is strongly depending on the used mooring configuration and cannot be generalized. The focus of the analysis lies on the conceptual method. Let α_{fl} denote the angle in the horizontal world plane between two mooring attachment points, start and end, (either anchor-fairlead, or fairlead-fairlead) with y- distance Δy_{se} and x-distance Δx_{se}. Clearly,

$$\alpha_{\mathrm{fl}}(t) = \tan^{-1}\left(\frac{\Delta y_{\mathrm{se}}}{\Delta x_{\mathrm{se}}}\right) \qquad (2.31)$$

Note that the 2 argument arctangent is used in (2.31) to cover all quadrants of the x-y plane. Now, state the vectors of the respective mooring tension in the world frame,

$$
\boldsymbol{v}_{\mathrm{IB,s}} = \begin{bmatrix} \cos\alpha_{\mathrm{s}}\cos\alpha_{\mathrm{fl}} \\ \cos\alpha_{\mathrm{s}}\sin\alpha_{\mathrm{fl}} \\ \sin\alpha_{\mathrm{s}} \end{bmatrix}, \quad \boldsymbol{v}_{\mathrm{IB,e}} = - \begin{bmatrix} \cos\alpha_{\mathrm{e}}\cos\alpha_{\mathrm{fl}} \\ \cos\alpha_{\mathrm{e}}\sin\alpha_{\mathrm{fl}} \\ \sin\alpha_{\mathrm{e}} \end{bmatrix}, \quad \boldsymbol{v}_{\mathrm{BTM}} = \begin{bmatrix} \cos(-\alpha_3)\cos\alpha_{\mathrm{fl}} \\ \cos(-\alpha_3)\sin\alpha_{\mathrm{fl}} \\ \sin(-\alpha_3) \end{bmatrix}.
$$
(2.32)

Consequently, the mooring tensions can be transformed into the body frames with,

$$
\hat{\boldsymbol{F}}_{\mathrm{IB,s}} = T_{\mathrm{IB},s}\boldsymbol{R}_r\frac{\boldsymbol{v}_{\mathrm{IB,s}}}{||\boldsymbol{v}_{\mathrm{IB,s}}||}, \quad \hat{\boldsymbol{F}}_{\mathrm{IB,e}} = T_{\mathrm{IB},s}\boldsymbol{R}_r\frac{\boldsymbol{v}_{\mathrm{IB,e}}}{||\boldsymbol{v}_{\mathrm{IB,e}}||}, \quad \hat{\boldsymbol{F}}_{\mathrm{BTM}} = T_{\mathrm{b}}\boldsymbol{R}_r\frac{\boldsymbol{v}_{\mathrm{BTM}}}{||\boldsymbol{v}_{\mathrm{BTM}}||}. \quad (2.33)
$$

Now, consider the torques about the CoG of the respective body,

$$
\hat{\boldsymbol{T}}_{\mathrm{IB,s}} = \begin{bmatrix} \hat{F}^y_{\mathrm{IB,s}}\hat{p}^z_{\mathrm{fl}} + \hat{F}^z_{\mathrm{IB,s}}\hat{p}^y_{\mathrm{fl}} \\ \hat{F}^x_{\mathrm{IB,s}}\hat{p}^z_{\mathrm{fl}} + \hat{F}^z_{\mathrm{IB,s}}\hat{p}^x_{\mathrm{fl}} \\ \sqrt{\hat{F}^x_{\mathrm{IB,s}} + \hat{F}^y_{\mathrm{IB,s}}}\,r_{\mathrm{b}}\sin\alpha_{\mathrm{diff}} \end{bmatrix}, \quad \hat{\boldsymbol{T}}_{\mathrm{IB,e}} = \begin{bmatrix} \hat{F}^y_{\mathrm{IB,e}}\hat{p}^z_{\mathrm{fl}} + \hat{F}^z_{\mathrm{IB,e}}\hat{p}^y_{\mathrm{fl}} \\ \hat{F}^x_{\mathrm{IB,e}}\hat{p}^z_{\mathrm{fl}} + \hat{F}^z_{\mathrm{IB,e}}\hat{p}^x_{\mathrm{fl}} \\ -\sqrt{\hat{F}^x_{\mathrm{IB,e}} + \hat{F}^y_{\mathrm{IB,e}}}\,r_{\mathrm{b}}\sin\alpha_{\mathrm{diff}} \end{bmatrix},
$$

$$
\hat{\boldsymbol{T}}_{\mathrm{BTM}} = \begin{bmatrix} \hat{F}^y_{\mathrm{BTM}}\hat{p}^z_{\mathrm{fl}} + \hat{F}^z_{\mathrm{BTM}}\hat{p}^y_{\mathrm{fl}} \\ \hat{F}^x_{\mathrm{BTM}}\hat{p}^z_{\mathrm{fl}} + \hat{F}^z_{\mathrm{BTM}}\hat{p}^x_{\mathrm{fl}} \\ \sqrt{\hat{F}^x_{\mathrm{BTM}} + \hat{F}^y_{\mathrm{BTM}}}\,r_{\mathrm{b}}\sin\alpha_{\mathrm{diff}} \end{bmatrix}. \quad (2.34)
$$

Here the lever arm for the yaw torque is the constant radius of the buoy r_{b}. The angle for the yaw torque represents the deviation between the angle of the mooring lines in the horizontal plane and the angle of the respective fairlead plus the instantaneous

yaw rotation of the WEC

$$\alpha_{\text{diff}} = \alpha_{\text{fl}} - \left(\tan^{-1} \left(\frac{\hat{p}_{\text{fl}}^y}{\hat{p}_{\text{fl}}^x} \right) + \hat{r}^z \right).$$
(2.35)

Note, that again the respective angle, respective fairlead position and respective yaw angle is used. The superscripts in (2.34) denote which component of the respective mooring force in the body coordinate frame is used. Finally, the generalized mooring force vector $\boldsymbol{F}_i^{\text{M}}$ is computed by superposing the force and torque components of the different mooring lines concatenate a zero for the piston,

$$\boldsymbol{F}_i^{\text{M}} = \begin{bmatrix} \hat{\boldsymbol{F}}_{\text{IB,s}} + \hat{\boldsymbol{F}}_{\text{IB,e}} + \hat{\boldsymbol{F}}_{\text{BTM}} \\ \hat{\boldsymbol{T}}_{\text{IB,s}} + \hat{\boldsymbol{T}}_{\text{IB,e}} + \hat{\boldsymbol{T}}_{\text{BTM}} \\ 0 \end{bmatrix}.$$
(2.36)

2.2.4 Excitation Force

Let us assume a wave field with a N_θ-directional swell, with the vector of incident wave angles $\boldsymbol{\theta} \in \mathbb{R}^{N_\theta}$ and wave spread

$$\boldsymbol{D}^\theta, \text{ with } \sum_{m=1}^{N_\theta} D_m^\theta = 1.$$
(2.37)

Since linear water wave theory is assumed the wave excitation at WEC i is described in terms of the phase shift

$$\phi_i^{\text{SH}} = \frac{2\pi}{\boldsymbol{\lambda}} \left(x_i \cos \boldsymbol{\theta} + y_i \sin \boldsymbol{\theta} \right).$$
(2.38)

Here the wave length vector $\boldsymbol{\lambda} \in \mathbb{R}^{N_\theta}$ follows (1.7). The resulting excitation force is obtained as a superposition of the N_w wave-frequency components and the N_θ directions,

$$\boldsymbol{F}_i^{\mathrm{Ex}} = \sum_{m=1}^{N_\theta} \sum_{k=1}^{N_\mathrm{w}} \boldsymbol{\Gamma}_i(\omega_k, \theta_m) D_m^\theta A_{k,m} \cos\left(\omega_k t + \phi_{i,m}^{\mathrm{SH}} + \phi_{k,m}^{\mathrm{RND}} + \boldsymbol{\phi}_i^{\mathrm{Ex}}(\omega_k, \theta_m)\right). \quad (2.39)$$

Here $\phi_{k,m}^{\mathrm{RND}}$ is a phase component for each frequency and direction and is a random variable governed by a uniform distribution over $[0, 2\pi]$. The vector containing hydrodynamic excitation coefficients $\boldsymbol{\Gamma}_i(\omega_k, \theta_m) \in \mathbb{R}^7$ at the wave frequency ω_k from direction θ_m and the corresponding excitation phase component $\boldsymbol{\phi}_i^{\mathrm{Ex}}(\omega_k, \theta_m)$ incorporate excitation and diffraction properties of the bodies into the model. The amplitudes of the waves components $A_{k,m}$ depend on the wave spectrum $S_{\omega,\mathrm{m}}(\omega)$ (1.16).

2.2.5 Radiation Force

The radiation problem yields more hydrodynamic coefficients which can be taken into account for in the time domain representation with the generalized force vector

$$\boldsymbol{F}_i^{\mathrm{R}}(t) = -\underbrace{\sum_{j=1}^{N} \boldsymbol{A}_{ij}^{\infty} \dot{\hat{\boldsymbol{x}}}_{\mathrm{vel},j}(t)}_{\boldsymbol{F}_i^{\mathrm{R},\infty}} - \underbrace{\sum_{j=1}^{N} \int_0^t \boldsymbol{K}_{ij}(t-\tau) \hat{\boldsymbol{x}}_{\mathrm{vel},j}(\tau)\mathrm{d}\tau}_{\boldsymbol{F}_i^{\mathrm{R'}}}, \quad (2.40)$$

acting on WEC i due to WEC j. With the state space representation in mind, the radiation force vector will be separated into two components. The first component $\boldsymbol{F}_i^{\mathrm{R},\infty}$ explicitly depends on the acceleration $\dot{\hat{\boldsymbol{x}}}_{\mathrm{vel},j}$ and the second component $\boldsymbol{F}_i^{\mathrm{R'}}$

explicitly depends on the velocity $\hat{\boldsymbol{x}}_{\mathrm{vel},j}$ of the jth WEC. Here $A_{ij}^{\infty} \in \mathbb{R}^{7\times 7}$ represents the constant added mass on WEC i due to motion of WEC j, as a result of the frequency dependent added mass $A_{ij}(\omega)$ evaluated at $\omega \to \infty$ as in Cummins formulation [7]. The kernel function of the convolution integral in (2.40) incorporates the frequency dependent radiation damping coefficient $B_{ij}(\omega) \in \mathbb{R}^{7\times 7}$ into the radiation force component depending on the velocity, via the inverse Fourier transformation

$$K_{ij}(t) = \frac{2}{\pi} \int_0^{\infty} B_{ij}(\omega) \cos(\omega t) \mathrm{d}\omega \qquad (2.41)$$

Consequently, instead of using the two real, frequency dependent matrix functions $\boldsymbol{A}(\omega) \in \mathbb{R}^{7N\times 7N}$ and $\boldsymbol{B}(\omega) \in \mathbb{R}^{7N\times 7N}$ the time dependent matrix function $\boldsymbol{K}(t) \in \mathbb{R}^{7N\times 7N}$ is used and the constant matrix $\boldsymbol{A}^{\infty} \in \mathbb{R}^{7N\times 7N}$ containing the same hydrodynamic information. This is known as the Kramers-Kronig relation in hydrodynamic radiation. The derivation using the principle of causality is described in [16] in detail. Instead of solving the convolution integral in (2.40) at every time step, it is approximated with a linear state space representations that shares the same impulse response. This has three major benefits. First, it makes the system more convenient for motion control and second, an increase in efficiency in terms of simulation time and third an easier integration into standard simulation environments such as Matlab/Simulink [53]. The implementation of the following method is based on the open source code from WECSim [62], with adjustments on how to find the maximal admissible order for the state space representation. To obtain a minimal realization of the discrete time impulse response the realization theory is being followed, due

its simplicity advantage over the continuous time [53]. Let us omit the subscript in the following description of the general approach, since the interactions between different WECs and different DoFs would generate confusion. The Hankel singular values are used, because of their representation of the energy for each artificial radiation state. High energy states are retained and discarded low energy states. Let $k^D[t_n]$, with $t_n = n\Delta t, n = 0, 1, 2, \ldots, N_\mathrm{t}$ denote the discretized version of a single impulse response component out of $\boldsymbol{K}(t)$. The Hankel matrix is a matrix assembly of the samples of the discrete input response, namely,

$$
H = \begin{bmatrix}
k^D[1] & k^D[2] & \cdots & \cdots & k^D[N_\mathrm{t}] \\
k^D[2] & k^D[3] & \cdots & k^D[N_\mathrm{t}] & 0 \\
\vdots & \vdots & 0 & & \vdots \\
\vdots & k^D[N_\mathrm{t}] & 0 & \ddots & \vdots \\
k^D[N_\mathrm{t}] & 0 & \cdots & \cdots & 0
\end{bmatrix}. \tag{2.42}
$$

Now, H can also be realized by using singular value decomposition,

$$
H = \boldsymbol{U}\boldsymbol{S}\boldsymbol{V}^\mathrm{H} \tag{2.43}
$$

where $\boldsymbol{S}$ contains the singular values in descending order on its diagonal. The unitary matrices $\boldsymbol{U}$ and $\boldsymbol{V}$ contain the singular vectors in their columns and $\boldsymbol{V}^\mathrm{H}$ denotes the Hermitian transpose (complex conjugate transpose) of $\boldsymbol{V}$. Now, let us assume the desired order $\mathcal{O}^\mathrm{R}$ of the radiation state space system is known and let us consider the

partitioning

$$\boldsymbol{S} = \begin{bmatrix} S_1 & \mathbf{0} \\ \mathbf{0} & S_2 \end{bmatrix}. \tag{2.44}$$

Here S_1 contains the $\mathcal{O}^R$ largest singular values on its diagonal and S_2 the remaining singular values. In Sec. 3.4 how to find a suitable maximal order $\mathcal{O}^R$ for the approximation so that S_1 sufficiently approximates the linear impulse response, is addressed. Therefore, (2.43) evolves into

$$H = \begin{bmatrix} \boldsymbol{U}_1 & \boldsymbol{U}_2 \end{bmatrix} \begin{bmatrix} S_1 & \mathbf{0} \\ \mathbf{0} & S_2 \end{bmatrix} \begin{bmatrix} V_1^{\mathrm{H}} & V_2^{\mathrm{H}} \end{bmatrix} \approx \boldsymbol{U}_1 S_1 V_1^{\mathrm{H}}, \tag{2.45}$$

The discrete radiation state space matrices can now be realized with [62] based on [32],

$$A_{\mathrm{R}}^{\mathrm{D}} = S_1^{-1/2} U_{11}^T U_{12} S_1^{1/2} \tag{2.46}$$

$$B_{\mathrm{R}}^{\mathrm{D}} = V_1^{\mathrm{H}} S_1^{1/2} \tag{2.47}$$

$$C_{\mathrm{R}}^{\mathrm{D}} = U_{11} S_1^{1/2} \tag{2.48}$$

$$D_{\mathrm{R}}^{\mathrm{D}} = k^D[0], \tag{2.49}$$

with U_{11} and U_{12} containing the first $\mathcal{O}^R$ singular vectors, with $n_{11} = 0, 1, \ldots, N_t - 2$ and with $n_{12} = 1, 2, \ldots, N_t - 1$, respectively. Finally, the discrete state space matrices

are numerically transformed into continuous time [62],

$$A^{\mathrm{R}} = \left(A_{\mathrm{R}}^{\mathrm{D}} - \boldsymbol{I}_{\mathcal{O}^{\mathrm{R}}}\right)\left(\frac{\Delta t}{2}\left(\boldsymbol{I}_{\mathcal{O}^{\mathrm{R}}} + A_{\mathrm{R}}^{\mathrm{D}}\right)\right)^{-1} \tag{2.50}$$

$$B^{\mathrm{R}} = \Delta t\left(\frac{\Delta t}{2}\left(\boldsymbol{I}_{\mathcal{O}^{\mathrm{R}}} + A_{\mathrm{R}}^{\mathrm{D}}\right)\right)^{-1} B_{\mathrm{R}}^{\mathrm{D}} \tag{2.51}$$

$$C^{\mathrm{R}} = C_{\mathrm{R}}^{\mathrm{D}}\left(\frac{\Delta t}{2}\left(\boldsymbol{I}_{\mathcal{O}^{\mathrm{R}}} + A_{\mathrm{R}}^{\mathrm{D}}\right)\right)^{-1} \tag{2.52}$$

$$D^{\mathrm{R}} = D_{\mathrm{R}}^{\mathrm{D}} - \frac{\Delta t}{2}\left(C_{\mathrm{R}}^{\mathrm{D}}\left(\frac{\Delta t}{2}\left(\boldsymbol{I}_{\mathcal{O}^{\mathrm{R}}} + A_{\mathrm{R}}^{\mathrm{D}}\right)\right)^{-1} B_{\mathrm{R}}^{\mathrm{D}}\right). \tag{2.53}$$

Now, bringing back the subscripts for WEC $i, j \in [1 : N]$ and use the respective DoFs, to state the generalized radiation force vector

$$\boldsymbol{F}_i^{\mathrm{R'}} = \sum_j \left(\boldsymbol{C}_{ij}^{\mathrm{R}}\boldsymbol{x}_{\mathrm{rad},ij} + \boldsymbol{D}_{ij}^{\mathrm{R}}\hat{\boldsymbol{x}}_{\mathrm{vel},j}\right), \tag{2.54}$$

with

$$\dot{\boldsymbol{x}}_{\mathrm{rad},ij} = \boldsymbol{A}_{ij}^{\mathrm{R}}\boldsymbol{x}_{\mathrm{rad},ij} + \boldsymbol{B}_{ij}^{\mathrm{R}}\hat{\boldsymbol{x}}_{\mathrm{vel},j}. \tag{2.55}$$

Here $\boldsymbol{x}_{\mathrm{rad},ij} \in \mathbb{R}^{\sum_j \mathcal{O}_{ij}^{\mathrm{R}}}$ is the artificial radiation state vector and

$$\boldsymbol{A}_{ij}^{\mathrm{R}} = \begin{bmatrix} A_{\hat{x}_i\hat{x}_j}^{\mathrm{R}} & & & & & & \\ & \ddots & & & & \mathbf{0} & \\ & & A_{x_i\hat{z}_j^{\mathrm{P}}}^{\mathrm{R}} & & & & \\ & & & A_{\hat{y}_i\hat{x}_j}^{\mathrm{R}} & & & \\ & & & & \ddots & & \\ & \mathbf{0} & & & & \ddots & \\ & & & & & & A_{\hat{z}_i^{\mathrm{P}}\hat{z}_j^{\mathrm{P}}}^{\mathrm{R}} \end{bmatrix} \in \mathbb{R}^{\sum_j \mathcal{O}_{ij}^{\mathrm{R}} \times \sum_j \mathcal{O}_{ij}^{\mathrm{R}}}, \qquad (2.56)$$

$$\boldsymbol{B}_{ij}^{\mathrm{R}} = \begin{bmatrix} B_{\hat{x}_i\hat{x}_j}^{\mathrm{R}} & & \\ & \ddots & \\ & & B_{\hat{x}_i\hat{z}_j^{\mathrm{P}}}^{\mathrm{R}} \\ B_{\hat{y}_i\hat{x}_j}^{\mathrm{R}} & & \\ & \ddots & \\ \vdots & \vdots & \vdots \\ & \ddots & \\ & & B_{\hat{z}_j^{\mathrm{P}}\hat{z}_j^{\mathrm{P}}}^{\mathrm{R}} \end{bmatrix} \in \mathbb{R}^{\sum_j \mathcal{O}_{ij}^{\mathrm{R}} \times 7}, \qquad (2.57)$$

$$
\boldsymbol{C}_{ij}^{\mathrm{R}} = \left[
\begin{array}{ccccc|c}
C_{b_1 b_1}^{\mathrm{rad}} & \cdots & C_{b_1 p_N}^{\mathrm{rad}} & \mathbf{0}^{1 \times N_{b_2 b_1}^{\mathrm{rad}}} & \cdots & \mathbf{0}^{1 \times N_{b_2 p_N}^{\mathrm{rad}}} \\
\mathbf{0}^{1 \times N_{b_1 b_1}^{\mathrm{rad}}} & \cdots & \mathbf{0}^{1 \times N_{b_1 p_N}^{\mathrm{rad}}} & C_{b_2 b_1}^{\mathrm{rad}} & \cdots & C_{b_2 p_N}^{\mathrm{rad}} \\
& & & \ddots & & \\
& \mathbf{0} & & & \ddots & \\
& & & \cdots & \mathbf{0}^{1 \times N_{p_N - p_N}^{\mathrm{rad}}} & C_{p_N b_1}^{\mathrm{rad}} \cdots C_{p_N p_N}^{\mathrm{rad}}
\end{array}
\right] .
$$

$$\tag{2.58}$$

It was also observed that requiring a very accurate fit seems to be of less importance [32]. This can be attributed to the feedback structure of the model, which filters out some of the dynamics associated with the convolution terms.

2.2.6 Air Chamber Pressure Force

The force connecting the buoy and the piston with the PTO results from the pressure in the air chamber, which is consequently a function of the displaced volume of the OWC and the mass flow rate through the turbine. In the following section the dynamics of the pressure are derived, following the example of [31] to model the PTO with a bi-radial turbine. The main assumptions are:

- The compression/expansion of the air is isentropic

- There is no heat transfer in the air chamber walls

- The temperature of the chamber has only small changes, due to the continuous in and outflow

Beginning with a mass balance on the air chamber control volume,

$$\rho_{c_i}\dot{V}_{c_i} + \dot{\rho}_i V_{c_i} = -\dot{m}_{t_i}, \tag{2.59}$$

where ρ_{c_i} is the air density, $\dot{m}_{t_i}$ is the mass flow through the turbines which is positive for an exhalation and is additionally a function of the position high speed stop valve (HSSV) p_{HSSV}, which is located before the turbine rotor and its position can be controlled. V_c denotes the volume of air inside the chamber, with the air chamber height as a function of position of the bodies

$$V_{c_i} = (h_0 + x_{z_{b_i}} - x_{z_{p_i}})S_{p_i} \tag{2.60}$$

Let us define the dimensionless relative pressure as a function of the absolute air pressure p_i in the chamber of OWC i and the atmospheric pressure p_{at}, i.e.

$$x_{p_i^*} = \frac{p_i - p_{\text{at}}}{p_{\text{at}}}. \tag{2.61}$$

Assuming air as a perfect gas and the process of air compression/expansion as isentropic as proposed in [13], yields

$$\frac{p_i}{\rho_i^\gamma} = \frac{p_{\text{at}}}{\rho_{\text{at}}^\gamma} \equiv \frac{x_{p_i^*} + 1}{\rho_{c_i}^\gamma} = \frac{1}{\rho_{\text{at}}^\gamma} \tag{2.62}$$

where $\gamma = c_p/c_v \approx 1.4$ denotes the specific heat ratio of air, also known as the isentropic expansion factor. c_v and c_p denote the specific heat capacities of air for a

constant volume and pressure, respectively, and are constant under the assumption of a perfect gas. Solving for ρ_{c_i} in (2.62), results in

$$\rho_{c_i} = \rho_{\text{at}}(x_{p_i^*} + 1)^{\frac{1}{\gamma}}. \tag{2.63}$$

Taking the logarithmic derivative $L(f) := \dot{f}/f$ of (2.63), yields

$$\gamma\frac{\dot{\rho}_{c_i}}{\rho_{c_i}} = \frac{\dot{x}_{p_i^*}}{x_{p_i^*} + 1}. \tag{2.64}$$

Substituting (2.63) and (2.64) into (2.59) results in

$$\dot{x}_{p_i^*} = -\gamma\frac{\dot{m}_{t_i}}{\rho_{\text{at}}V_{c_i}}(x_{p_i^*} + 1)^{\frac{\gamma-1}{\gamma}} - \gamma\frac{\dot{V}_c}{V_{c_i}}(x_{p_i^*} + 1) \tag{2.65}$$

Equation (2.65) will appear in the written out form in the fully described state space representation, where the chamber volume and its derivative depend on the position and velocity states, respectively.

The force on the OWC and buoy is now dependent on the pressure difference of the atmosphere $p_i - p_{\text{at}}$ in the chamber together with the cross section of the piston and

can be stated as

$$\boldsymbol{F}_i^{\text{PTO}} = \begin{bmatrix} 0 \\ 0 \\ (x_{p_i^*} p_{\text{at}}) S_p \\ 0 \\ 0 \\ 0 \\ -x_{p_i^*} p_{\text{at}} S_p \end{bmatrix}. \tag{2.66}$$

To completely determine (2.65), the mass flow is required, thus it is necessary to consider the turbine dynamics. The ensuing approach is adapted from [30]. Beginning with the change of the rotational speed x_{Ω_i} of the turbine

$$\dot{x}_{\Omega_i} = \frac{1}{I_{\text{t}}} \left(T_{\text{t}_i} - T_{\text{gen}_i} - B_{\text{t}} x_{\Omega,i} \right) \tag{2.67}$$

where I_{t_i} is the moment of inertia of the ith turbine/generator set, T_{t_i}, T_{gen_i} are instantaneous torques of the ith turbine and the generator, respectively, and B_{t} is a constant that models viscous friction losses. To identify the torque of the turbine, it is necessary to regard its performance characteristics which are presented in dimensionless form. To normalize those values, the rotational speed x_{Ω_i}, the turbine diameter d_{t} and the reference air density ρ_{in} are needed. Furthermore, the turbine characteristics change with the position of the HSSV u_{HSSV}, which limits the air flow into the turbine. ρ_{in} is defined under stagnation conditions at the turbine entrance and dependent on the flow direction, hence a function of the pressure difference between the chamber

and the atmosphere, i.e.

$$
\rho_{\text{in}_i} = \begin{cases} \rho_{\text{at}}(x_{p_i^*} + 1)^{\frac{1}{\gamma}}, & \text{if } x_{p_i^*} > 0 \quad \text{(exhalation)} \\[12pt] \rho_{\text{at}}, & \text{if } x_{p_i^*} < 0 \quad \text{(inhalation)}. \end{cases}
\tag{2.68}
$$

The dimensionless pressure head can now be computed as

$$
\Psi_i = \frac{p_{\text{at}} x_{p_i^*}}{\rho_{\text{in}_i} x_{\Omega_i}^2 d_{\text{t}}^2}.
\tag{2.69}
$$

The dimensionless mass flow rate coefficient of a turbine is defined by

$$
\Phi_i(\Psi_i, u_{\text{HSSV},i}) = \frac{\dot{m}_{\text{t}_i}}{\rho_{\text{in}_i} x_{\Omega_i} d_{\text{t}}^3}.
\tag{2.70}
$$

Finally, the dimensionless power coefficient is given by

$$
\Pi_i(\Psi_i, u_{\text{HSSV},i}) = \frac{P_{\text{t}_i}}{\rho_{\text{in}_i} x_{\Omega_i}^3 d_{\text{t}}^5}.
\tag{2.71}
$$

Those three characteristic coefficients are related through the turbine efficiency as follows:

$$
\eta_{\text{t}_i}(\Psi_i, u_{\text{HSSV},i}) = \frac{\Pi_i}{\Phi_i \Psi_i}
\tag{2.72}
$$

In [4] Φ_i (⋯⋯) and η_{t_i} (- - - -) are given as functions of the dimensionless pressure head Ψ_i and the position of the HSSV u_{HSSV} as illustrated in Fig. 2.8 together with the dimensionless power coefficient (——) calculated with $\Pi = \eta \Phi \Psi$. The mass flow rate $\dot{m}_{\text{t}_i}$ can be determined from (2.70) and is a function of the rotational speed,
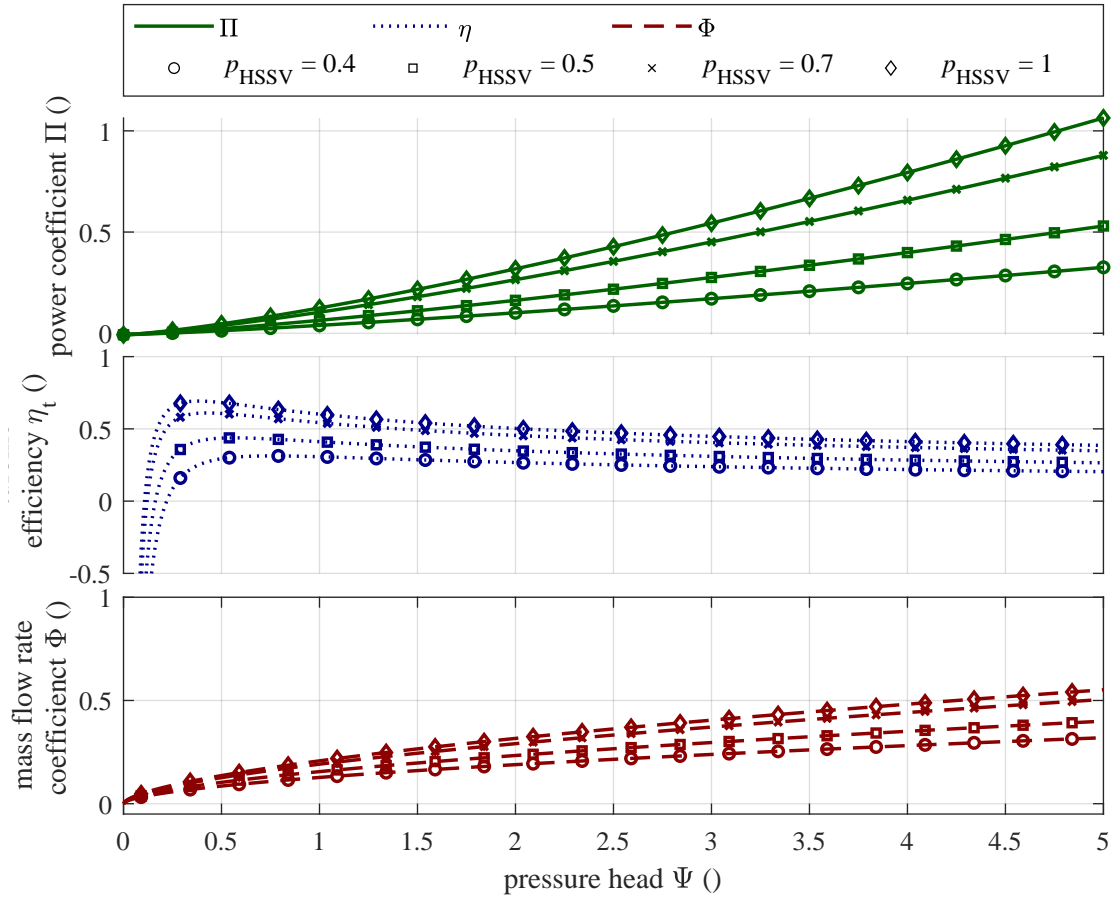
Figure 2.8: Turbine characteristics as functions of the dimensionless pressure head Ψ. Namely, efficiency η, dimensionless flow rate Φ and dimensionless power coefficient Π.

which will become important regarding the controllability of the system. As stated before, an additional high speed stop valve is installed before the biradial turbine, to realise for example latching. Assuming the HSSV can stop the entire mass flow, the mass flow rate can be stated as

$$\dot{m}_{\mathrm{t}_i}(x_{\Omega_i}, u_{\mathrm{HSSV},i}) = \Phi_i(\Psi_i, u_{\mathrm{HSSV},i})\rho_{\mathrm{in}_i}x_{\Omega_i}d_{\mathrm{t}}^3, \tag{2.73}$$

where $p_{\mathrm{HSSV},i}$ denotes the position of the stop valve and is open for $p_{\mathrm{HSSV},i} = 0$ and completely closed for $p_{\mathrm{HSSV},i} = 1$, respectively. Finally, with equations (2.71) and (2.72) all necessary quantities to compute the turbine torque are known, i.e.

$$T_{\mathrm{t}_i} = \rho_{\mathrm{in}_i}x_{\Omega_i}^2 d_{\mathrm{t}}^5 \eta_{\mathrm{t}_i}\Phi_i\Psi_i \tag{2.74}$$

The generator power torque T_{gen_i} is the commonly used control input to WEC. Additionally, the position of the HSSV provides further influence on the pressure change in the air chamber.

2.2.7 Viscous Drag Force

The last considered force is the one due to viscous drag between water and the bodies. It is based on the drag component of the semi-empirical Morison equation [38], namely,

$$\boldsymbol{F}_i^{\mathrm{VD}} = -\frac{1}{2}\rho_{\mathrm{w}}C_{\mathrm{VD}}A_{\mathrm{VD}}\hat{\boldsymbol{x}}_{\mathrm{vel},i}|\hat{\boldsymbol{x}}_{\mathrm{vel},i}|. \tag{2.75}$$

Here C_VD represents a matrix with quadratic drag coefficient on its diagonal, estimated based on empirical data for slender cylinders and A_VD denotes the matrix with the reference area for respective DoF.

2.3   Electric Power Flow Model

The next steps in the power conversion chain happen with much faster dynamics than the WEC motion. Harris shows that the transfer function of the generator current dynamics are approximately one when the main interest is the commanded control torque [28]. The switching dynamics of the power electronics (PE) are even faster. Furthermore, there is no interaction between the electromagnetic energy conversion and the hydrodynamics of the WEC. Consequently, the dynamic model will not include the detailed generator and PE switching dynamics, instead the respective efficiencies account for power dissipation. The generator is run in torque mode and the assumption that $T_{\mathrm{gen},i}$ commanded by the drive is received, holds. A suitable generator to directly attach to the biradial turbine is the SIEMENS IEC low-voltage squirrel cage (SC) electrical model 1LE1603-2AB53-4GB4-Z. The empirical data of the generator efficiency η_gen of the SC machine is illustrated in Fig. 2.9 [4, 5]. Now, let us state the alternating current (AC) electric power,

$$P_{\mathrm{elec},i}^\mathrm{AC} = \eta_{\mathrm{gen},i} |T_{\mathrm{gen},i}| x_{\Omega,i}(t) \tag{2.76}$$
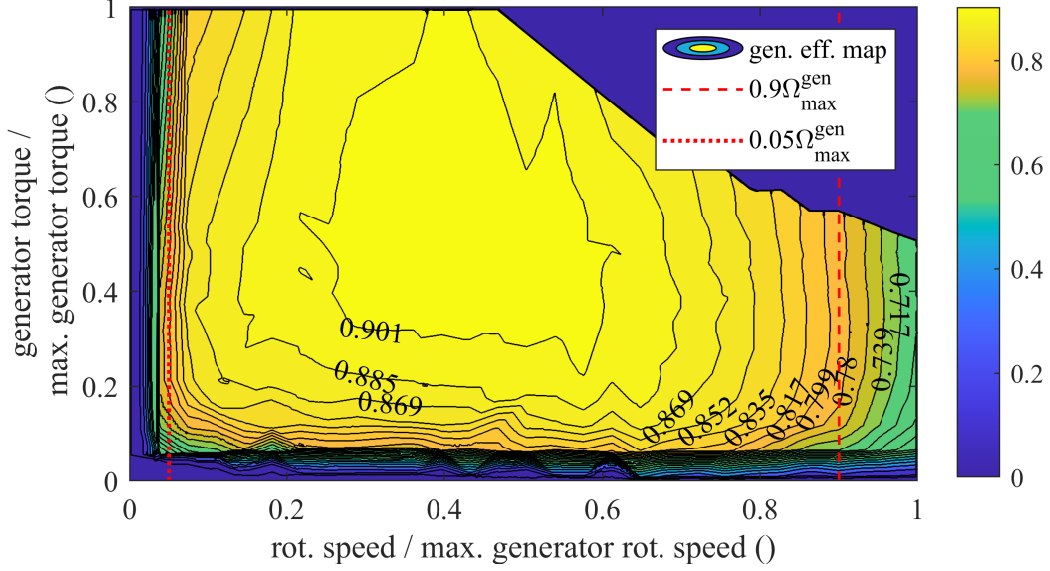
Figure 2.9: Generator efficiency map as a function of the turbine-generator sets rotational speed and generator (control) torque. From [5].

The electric components after each SC machine and their connections are illustrated in Fig. 2.10. Let us assume that every single WEC has the PE to convert from AC to direct current (DC), with round trip efficiency η_{PE}, hence

$$P_{\text{elec},i}^{\text{DC}} = \begin{cases} \eta_{PE} P_{\text{elec},i}^{\text{AC}}, & \text{for } P_{\text{elec},i}^{\text{AC}} \geq 0 \\ P_{\text{elec},i}^{\text{AC}}/\eta_{PE}, & \text{for } P_{\text{elec},i}^{\text{AC}} < 0. \end{cases} \tag{2.77}$$

Next, a DC-link is modelled so that the power can flow freely between the different WECs in the park. This enables the use of the SC generator in motor mode, e.g. for reference speed following. The power necessary to turn the first WECs turbine could come from a currently generating WEC. The high current cables could for example
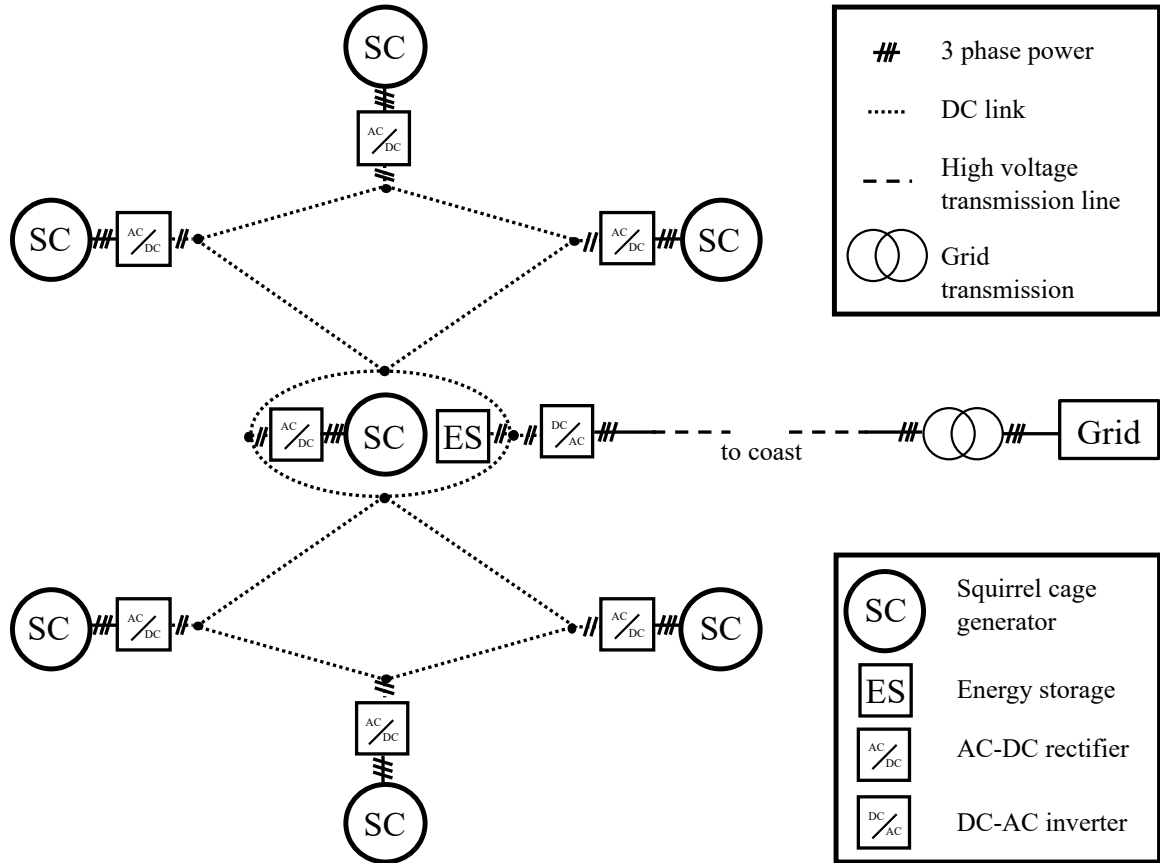
Figure 2.10: Electric power flow model of the WEC park.

go along the IB mooring lines. Let us further assume a directly connected storage medium (battery) in the DC link. The last part of the link is a grid connection, via an inverter with efficiency $\eta_{\mathrm{PE,IV}}$. The instantaneous power of the link is therefore,

$$P_{\mathrm{link}} = \sum_i P_{\mathrm{elec},i}^{\mathrm{DC}} - P_{\mathrm{load}} \qquad (2.78)$$

If the grid load power P_{load} can be met by the aggregated power of the individuals WECs $P_{\mathrm{link}} \geq 0$. On the other hand, if the load is not met the differences need to

come from the storage medium with efficiency η_{SM}. The state of charge x_{SOC} of the battery is the last state space state, with its change rate being

$$\dot{x}_{\text{SOC}} = \frac{1}{W_{\text{SM}}^{\text{rated}}} \begin{cases} \eta_{\text{SM}} P_{\text{link}}, & \text{for } P_{\text{link}} \geq 0 \\ P_{\text{link}}/\eta_{\text{SM}}, & \text{for } P_{\text{link}} < 0. \end{cases} \tag{2.79}$$

Here W_{SM} denotes the rated storage capacity of the battery. Assuming to be able to control that amount of grid power transmission, let us define the last input,

$$u_{\text{load}} = P_{\text{load}}. \tag{2.80}$$

This finalizes the power conversion chain from wave to wire.

2.4   OWC Park State Space Simulation Model

The equations above are transformed to represent them in the state space with variable vector,

$$\dot{\boldsymbol{x}} = \begin{bmatrix} \dot{\boldsymbol{\mathcal{X}}}_{\text{pos}} \\ \dot{\hat{\boldsymbol{\mathcal{X}}}}_{\text{vel}} \\ \dot{\boldsymbol{x}}_{p^*} \\ \dot{\boldsymbol{x}}_{\Omega} \\ \dot{x}_{\text{SOC}} \end{bmatrix} = \begin{bmatrix} \boldsymbol{\mathcal{J}}_r \hat{\boldsymbol{\mathcal{X}}}_{\text{vel}} \\ (\boldsymbol{\mathcal{M}})^{-1} \cdot \boldsymbol{\mathcal{F}}(\boldsymbol{x}) \\ \boldsymbol{f}_{p^*}(\boldsymbol{x}, \boldsymbol{u}_{\text{HSSV}}) \\ \boldsymbol{f}_{\text{k}}(\boldsymbol{x}_{p^*}, \boldsymbol{x}_{\Omega}, \boldsymbol{u}_{\text{gen}}) \\ f_{\text{SM}}(\boldsymbol{x}_{\Omega}, \boldsymbol{u}_{\text{gen}}, u_{\text{load}}) \end{bmatrix} \tag{2.81}$$

Note that script letters represent concatenated vectors and matrices to include all vectors $i \in [1; 7]$. The linear mapping between reference and body coordinate frame

$\boldsymbol{\mathcal{J}}_r$ contains the individual matrices $\boldsymbol{J}_{r,i}$ on its diagonal. The inertial matrix $(\boldsymbol{\mathcal{M}})^{-1}$ contains the individual mass and moment of inertia components in the respective DoF with $\boldsymbol{M}$. Coupling between surge-pitch and sway-roll for the respective buoy is taken into account with $\boldsymbol{M}_{\mathrm{cpl}}$ [40]. Furthermore, $\boldsymbol{\mathcal{M}}$ contains entries connecting spatially distinct WECs due to the added mass components $\boldsymbol{\mathcal{A}}^{\infty}$, thus

$$\boldsymbol{\mathcal{M}} = \boldsymbol{M} + \boldsymbol{M}_{\mathrm{cpl}} + \boldsymbol{\mathcal{A}}^{\infty} \tag{2.82}$$

Further cross body interactions originate from the mooring force and the radiation force, hidden in $\boldsymbol{\mathcal{F}}(\boldsymbol{x})$. The pressure, rotational speed and charge states change rates in (2.81) are presented as functions of their major drivers, but follow eqs. (2.65), (2.67) and (2.79) respectively.

2.5   Summary

The presented first principle equations describe how wave energy is converted to the power grid over time, with help of a Spar-buoy type WEC park. Those system dynamics in all degrees of freedom are presented in a generalized a control oriented state space form. Selecting different WEC park configurations are only subject to different hydrodynamics coefficients and potentially a different mooring configuration, but the general approach is applicable. The dynamic model enables the simulation in engineering software like MATLAB/Simulink and the design of model based control algorithms to alter the system dynamics. However, the parameters like the hydrody-

namics coefficients need to be identified first.

Chapter 3   Hydrodynamics

The commonly used approach to approximate the hydrodynamic interactions in terms of linear hydrodynamic coefficient has shown to not significantly differ from more detailed nonlinear approaches [59]. Therefore, the Boundary Element (BEM) solver software ANSYS Aqwa is used to obtain the main hydrodynamic coefficients, which are required to quantify the hydrodynamic forces (Sec. 2.2.5 and Sec. 2.2.4). The process to determine a suitable separation distance was iterative. First, the BEM results were generated for a triangular array and then the dynamic simulation with Matlab/Simulink of the array restricted to heave motion was evaluated for its interactions [17]. The spacing of $d_\mathrm{s} = 30\,\mathrm{m}$ seemed a good compromise between proximity and enough space for maintenance through boats. Next, the dynamic simulation model in six DoF confirmed that the WECs do not collide with $d_\mathrm{s} = 30\,\mathrm{m}$.

This chapter describes how the hydrodynamic coefficients of a triangular array with $d_\mathrm{s} = 30\,\mathrm{m}$ with a full column representation of the internal water column are obtained and later combined with the hydrodynamic coefficients of the hexagon park simulated without the internal water column in the BEM solver ANSYS Aqwa Release 19.1. The combination is necessary since the seven device in a hexagon violate the maximal diffracting elements in Aqwa, when the internal water column is represented by an artificial rigid body, as done for the triangular array. This is possible since the triangular array is a sub-component of the hexagon park and the properties

can be interpolated and extrapolated, respectively.
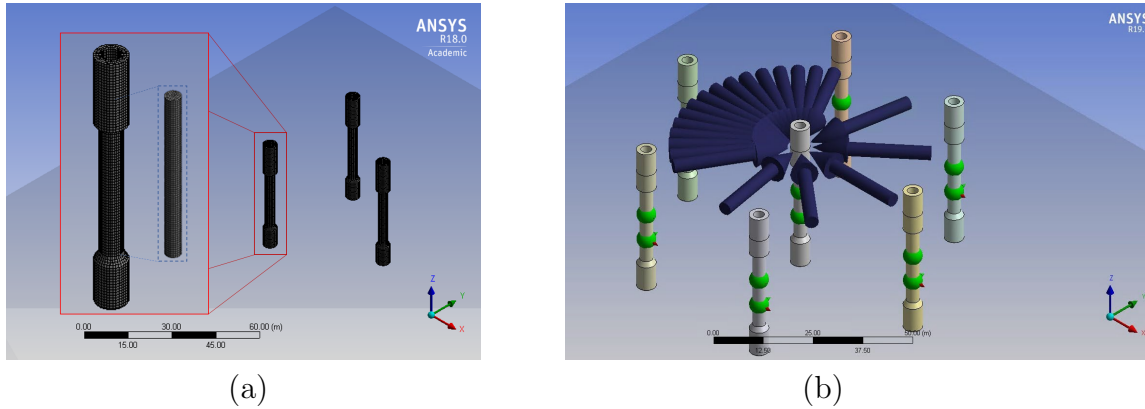
Figure 3.1: Screen shots from the BEM solver ANSYS Aqwa. Left: Triangular Marmok-A-5 array with full-column presentation of the water column. Right: Hexagon seven Marmok-A-5 park with incident wave directions.

3.1 Boundary Element Solver Simulation

ANSYS Aqwa is a 3D simulation tool witch Graphical User Interface (GUI), which uses ANSYS Workbench as its front end. Workbench is a multi physics software that enables importing different CAD formats as well as coupling between distinct physical problems. A facilitation for the simulation process is the Project Schematic where different stages of the simulation are initiated through adding of so-called systems. For example, the Hydrodynamic Diffraction system which provides a toolset for the investigation of the effects of waves on structures, to develop the hydrodynamic parameters required for motion and response analyses. The Project Scheme is divided into multiple steps which can be processed hierarchically until the desired results are obtained. CAD models are imported in the Geometry system, with the specialized

software package DesignModeler (DM) behind it. The model has to be displaced in order to set the XY-Plane where the water surface should meet the semi-submerged geometries. Aqwa is only able to work with surface bodies with their normals pointing outwards therefore all geometries have to have their wall thickness set to zero.

The single OWC WEC is translated and duplicated at the same time to build up the desired park configurations with a spacing of $d_\mathrm{s} = 30\,\mathrm{m}$ between the centers of the WECs. As soon as all bodies are in place and are transformed to surface bodies, the XY-Plane can be used to cut through all bodies, in order to emulate the water surface. Dissected bodies have to be reassembled using the *Part* function of the DM.

The buoy dimensions are as illustrated in Fig. 1.12 and relevant to the actual parameters of the prototype. The OWC is modeled as a physical body inside the BEM modeler with a diameter $d_\mathrm{p}^\mathrm{BEM} = d_\mathrm{p} - 0.02\,\mathrm{m}$, as pictured by the red dashed box surrounding the piston in Fig. 1.12 for the triangular array, but not for the hexagon park. Instead of using a weightless thin plate to represent the water surface inside the chamber as done in the beginning of this study, a full column representation of the piston is used since it reduces numerical instabilities in the frequency dependent hydrodynamic coefficients, which agrees with the results of [51, 1]. Furthermore, the calculated overall mass approaches the actual one, which is of importance for the natural frequency of the piston in the time domain simulations. The meshed water column is illustrated in Fig. 3.1 (a). The incident wave angle θ ranges from $-60°$ to $60°$ in an interval of $8°$ and from $-180°$ to $180°$ in an interval of $40°$, which are illustrated in the WEC park in Fig. 3.1 (b). The wave frequency is also divided into multiple ranges f_1, f_2 and f_3, to better cover the areas of interest, which require a finer

Table 3.1: Numerical values of the BEM simulation parameters.

Quantity	sym/var	value
spacing distance WECs	d_s	$30\,\mathrm{m}$
water depth	d_w	$80\,\mathrm{m}$
incident wave range 1	θ_1	$-60°\!:\!8°\!:\!60°$
incident wave range 2	θ_2	$-180°\!:\!40°\!:\!180°$
wave frequency range 1	f_1	$\{0.015\!:\!0.05\!:\!0.250\}[\mathrm{Hz}]$
wave frequency range 2	f_2	$\{0.256\!:\!0.06\!:\!0.496\}[\mathrm{Hz}]$
wave frequency range 3	f_3	$\{0.506\!:\!0.01\!:\!0.606\}[\mathrm{Hz}]$
diameter buoy	d_b	$5.00\,\mathrm{m}$
diameter inner tube	d_p	$2.82\,\mathrm{m}$
piston diameter in BEM	$d_\mathrm{p}^{\mathrm{BEM}}$	$2.80\,\mathrm{m}$

resolution for low frequencies and long wave periods, respectively. The approximation of the infinite frequency for A_{ij}^∞ is done with the high frequency $\omega_{\mathrm{HF}} = 100.0\,\mathrm{rad/s}$ in Aqwa 19.1. In the ensuing sections the main hydrodynamic results are presented.

3.2 Order Reduction

To improve the computational cost, an interaction distance cut-off is introduced for the hexagon park, while maintaining acceptable accuracy [27]. Therefore, interactions between WECs with more than $d_\mathrm{s} = 30\,\mathrm{m}$ separation are neglected. The scheme is illustrated in Fig. 3.2. The central WEC interacts with all surrounding WECs and the corner WECs interact with the three WECs that lay on the circle around them with radius d_s. In the next section the scheme is also illustrated in matrix form.
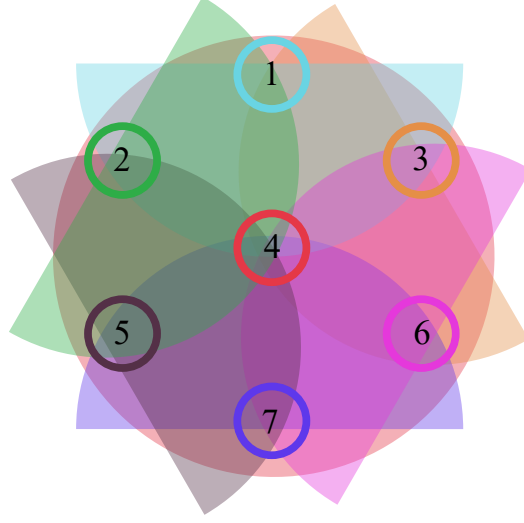
Figure 3.2: Considered cross body interactions in the OWC WEC park. Interactions of bodies with more than $d_{\mathrm{s}} = 30\,\mathrm{m}$ are neglected.

3.3   Added Mass

The concatenated added mass matrix at approximately infinite frequency $\boldsymbol{\mathcal{A}}^{\infty}$ is part of the inertial matrix $(\boldsymbol{\mathcal{M}})^{-1}$ in (2.81).

$$
\boldsymbol{\mathcal{A}}^{\infty} =
\begin{bmatrix}
A_{11}^{\infty} & A_{12}^{\infty} & A_{13}^{\infty} & A_{14}^{\infty} & \mathbf{0} & \mathbf{0} & \mathbf{0} & A_{1}^{\mathrm{bp},\infty} \\
A_{21}^{\infty} & A_{22}^{\infty} & \mathbf{0} & A_{24}^{\infty} & A_{25}^{\infty} & \mathbf{0} & \mathbf{0} & A_{2}^{\mathrm{bp},\infty} \\
A_{31}^{\infty} & \mathbf{0} & A_{33}^{\infty} & A_{34}^{\infty} & \mathbf{0} & A_{36}^{\infty} & \mathbf{0} & A_{3}^{\mathrm{bp},\infty} \\
A_{41}^{\infty} & A_{42}^{\infty} & A_{43}^{\infty} & A_{44}^{\infty} & A_{45}^{\infty} & A_{46}^{\infty} & A_{47}^{\infty} & A_{4}^{\mathrm{bp},\infty} \\
\mathbf{0} & A_{52}^{\infty} & \mathbf{0} & A_{54}^{\infty} & A_{55}^{\infty} & \mathbf{0} & A_{57}^{\infty} & A_{5}^{\mathrm{bp},\infty} \\
\mathbf{0} & \mathbf{0} & A_{63}^{\infty} & A_{64}^{\infty} & \mathbf{0} & A_{66}^{\infty} & A_{67}^{\infty} & A_{6}^{\mathrm{bp},\infty} \\
\mathbf{0} & \mathbf{0} & \mathbf{0} & A_{74}^{\infty} & A_{75}^{\infty} & A_{76}^{\infty} & A_{77}^{\infty} & A_{7}^{\mathrm{bp},\infty} \\
A_{\mathrm{b}_1}^{\mathrm{p},\infty} & A_{\mathrm{b}_2}^{\mathrm{p},\infty} & A_{\mathrm{b}_3}^{\mathrm{p},\infty} & A_{\mathrm{b}_4}^{\mathrm{p},\infty} & A_{\mathrm{b}_5}^{\mathrm{p},\infty} & A_{\mathrm{b}_6}^{\mathrm{p},\infty} & A_{\mathrm{b}_7}^{\mathrm{p},\infty} & A^{\mathrm{pp},\infty}
\end{bmatrix} .
\tag{3.1}
$$

Here $A_{ij}^\infty \in \mathbb{R}^{6\times 6}$ denotes the added mass of WEC buoy i due to acceleration of WEC buoy j in all DoFs, which directly originate from the BEM simulation of the park with the seven spar-buoy WECs. The matrices in the column $A_i^{\mathrm{bp},\infty} \in \mathbb{R}^{6\times 7}$ contain the added mass on all DoFs of WEC i due to heave acceleration of the pistons, derived from the BEM simulation of the triangular array with the pistons. The matrices in the last row $A_{\mathrm{b}_i}^{\mathrm{p},\infty} \in \mathbb{R}^{7\times 6}$ denote the heave added mass components on the pistons due to acceleration of buoy b_i in all DoFs, again derived from the triangular array. The last matrix in the lower right corner $A^{\mathrm{pp},\infty} \in \mathbb{R}^{7\times 7}$ contains the heave added mass components on pistons due to piston heave motion, from the triangular array. The zero matrices are the results if the interaction distance cut-off. The cut-off also affects $A_i^{\mathrm{bp},\infty}$, $A_{\mathrm{b}_i}^{\mathrm{p},\infty}$ and $A^{\mathrm{pp},\infty}$ since they contain bodies from spatially distinct WEC systems, resulting in many zero entries. The numerical values of some examples representing a group of added mass matrices are presented in appendix A.

3.4   Radiation Damping

The radiation damping effects have a high computational complexity to simulate, since they take the past motion of a body into account. In this work a reduction method based on the magnitude the radiation impulse response function (IRF) $K_{ij}(t)$ (eq. (2.41)) is used. The algorithm (adapted from WECSim [62]) that approximates $K_{ij}(t)$ with a state space representation through a Hankel singular value decomposition (2.43) iteratively increases the order $\mathcal{O}^{\mathrm{R}}$ until either the goodness of the fit exceeds 0.95, or the maximal order is reached. The maximal order $\mathcal{O}_{\max}^{\mathrm{R}}$ is depending

on the initial goodness

$$R_{\mathrm{i}}^2 = ||K_{ij}(t) - \bar{K}_{ij}||. \tag{3.2}$$

Here $\bar{K}_{ij}$ denotes the mean value of $K_{ij}(t)$. A high R_{i}^2 means a lot of oscillations in the IRF and potentially time delays. Consequently it needs higher order dynamics to perform an accurate fit. If the maximal value of $K_{ij}(t)$ does not meet a user defined threshold $\mathcal{O}_{\max}^{\mathrm{R}}$ is set to zero. This implies that the radiation interactions for this combination are neglected. Radiation damping effects of the same body are never neglected, mostly for stability reasons and not because they significantly alter the dynamic response. This methods results in the same pattern as the interaction distance cut off, as illustrated with

$$\boldsymbol{B} = \begin{bmatrix} B_{11} & B_{12} & B_{13} & B_{14} & \mathbf{0} & \mathbf{0} & \mathbf{0} & \mathbf{0} \\ B_{21} & B_{22} & \mathbf{0} & B_{24} & B_{25} & \mathbf{0} & \mathbf{0} & \mathbf{0} \\ B_{31} & \mathbf{0} & B_{33} & B_{34} & \mathbf{0} & B_{36} & \mathbf{0} & \mathbf{0} \\ B_{41} & B_{42} & B_{43} & B_{44} & B_{45} & B_{46} & B_{47} & \mathbf{0} \\ \mathbf{0} & B_{52} & \mathbf{0} & B_{54} & B_{55} & \mathbf{0} & B_{57} & \mathbf{0} \\ \mathbf{0} & \mathbf{0} & B_{63} & B_{64} & \mathbf{0} & B_{66} & B_{67} & \mathbf{0} \\ \mathbf{0} & \mathbf{0} & \mathbf{0} & B_{74} & B_{75} & B_{76} & B_{77} & \mathbf{0} \\ \mathbf{0} & \mathbf{0} & \mathbf{0} & \mathbf{0} & \mathbf{0} & \mathbf{0} & \mathbf{0} & B^{\mathrm{pp}} \end{bmatrix}. \tag{3.3}$$

In contrast to the added mass, the entries $\boldsymbol{B}$ are sparse matrices with the frequency dependent radiation coefficients in all six DoFs. In Fig. 3.3 a few of the radiation damping coefficients are illustrated as example. The first subplot contains the heave-

heave radiation $B_{zz}(\omega)$ coefficients of for a WEC in the triangular array and a WEC in the hexagon park. Except for numerical instabilities the coefficients show good agreement. The next two subplot show coefficients only available to the triangular
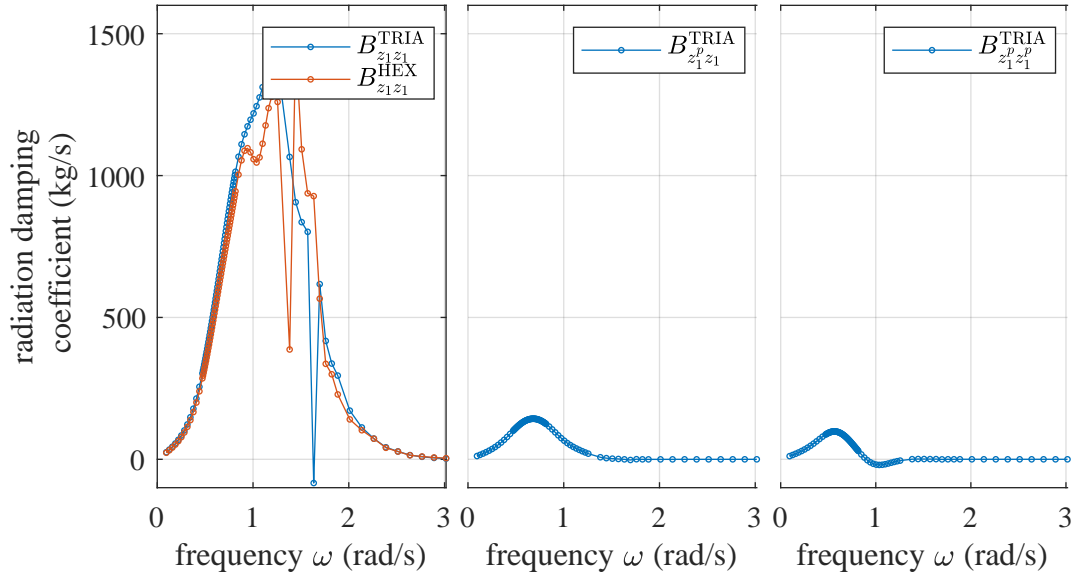
Figure 3.3: Frequency dependent radiation damping coefficient examples from the BEM results of the triangular three WEC array and the seven WEC hexagon WEC park.

array, since they involve the pistons heave motion. The interactions between heave-buoy and heave-piston do not pass the threshold (central subplot in Fig 3.3 and are neglected for the IRFs. The most important IRFs for a buoy due to its own motion are illustrated in Fig 3.4 in dashed, together with the respective state space approximation in solid and the corresponding order $\mathcal{O}$ used for the fit. Due to symmetry of the buoy a lot of radiation combinations are qualitatively identical, e.g. K_{xx} and K_{yy}. Most of the inter-body radiation combinations have in common, that they decay quickly so
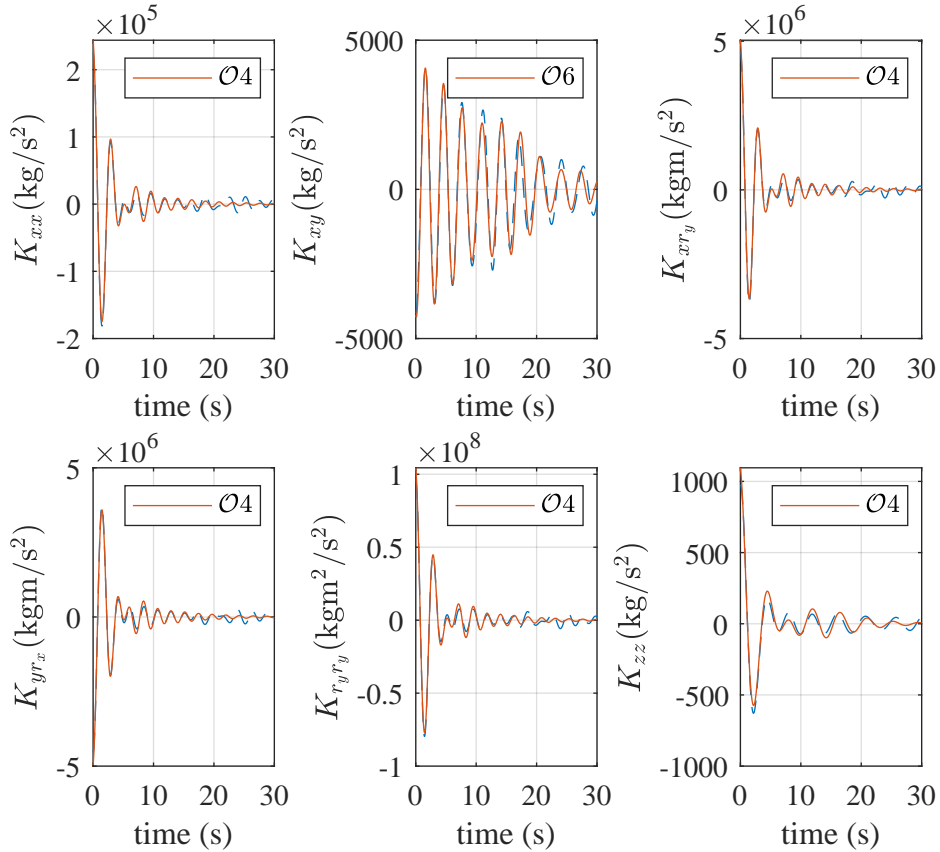
Figure 3.4: Most significant radiation impulse response functions of a buoy due to its own motion.

that they can easily with the relatively low order $\mathcal{O}4$. An exception is the surge-sway IRF K_{xy} (and consequently also K_{yx}). Here $\mathcal{O}6$ is necessary to meet the meet the desired goodness of the fit. The radiation effects between spatially distinct WEC generally need a higher order of the state space approximation, because the peak of the IRF is not at the initial time. Some of those cross-body radiation interactions are illustrated in Fig 3.5. For example $K_{y_j x_i}$ in the top left corner would have benefited

from an order $> \mathcal{O}6$, but the magnitude of the maximal value of $K_{y_j x_i}$ resulted in $\mathcal{O}6$ as threshold. In the top right corner of the figure an example with the highest admissible order $\mathcal{O}8$ is illustrated. It has to be noted that the lower right plot is an interaction

Figure 3.5: Most significant radiation impulse response functions between spatially distinct buoys and for the heave radiation of the piston.

due a body's own motion, namely the IRF for the heave radiation of the piston. Here $\mathcal{O}2$ sufficiently model the simple IRF. Overall the method with Hankel singular value decomposition yields much better goodness of fit with the same state space order
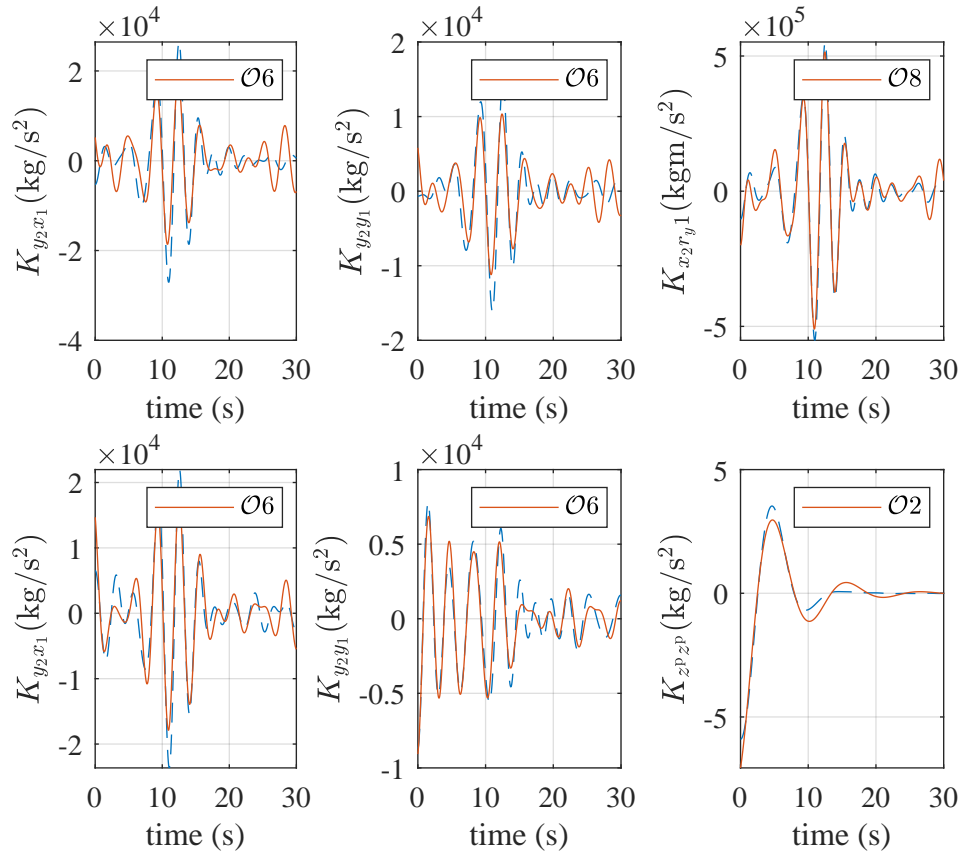
compare to the Prony method previously used in [17]. Especially, for cross-body interactions since Prony's method superposes decaying exponential functions, that all start decaying at the initial time. The overall concatenated radiation state space system eqs. (2.54) and (2.55) has $7N = 49$ inputs and outputs and 3210 artificial radiation states. Without the order reduction it would have been well above 10000 states.

3.5   Excitation Coefficients

The combination of the excitation force coefficients for the excitation force (2.39) between hexagon park and triangle array is straight forward. Fig 3.6 illustrates all the heave excitation force coefficients $\Gamma_i^x(\omega_k, \theta_m)$ for the array with the three WECs and the three pistons in the left column and the corresponding phase components $\phi_i^{\text{Ex}}(\omega_k, \theta_m)$ in the right column. The pistons excitation force coefficient is invariant to the incident wave angle θ_m and only a function of the wave frequency ω_k. The pistons phase is qualitatively identical with the phase component of its buoy. This makes it evident to use the pistons excitation force coefficient from the triangular array and combine it with the phase component of the buoys from hexagon park, to artificially add the heave excitation properties of the water column to the WEC park. All seven excitation force coefficients of the WEC park and the corresponding phase coefficients are illustrated in Fig. 3.7. The symmetry of the hexagon clearly is evident in the coefficients. For example, the pairs WEC1 and WEC5, WEC1 and WEC6, and WEC2 and WEC7 have the same coefficient, but mirrored about the surge axis,
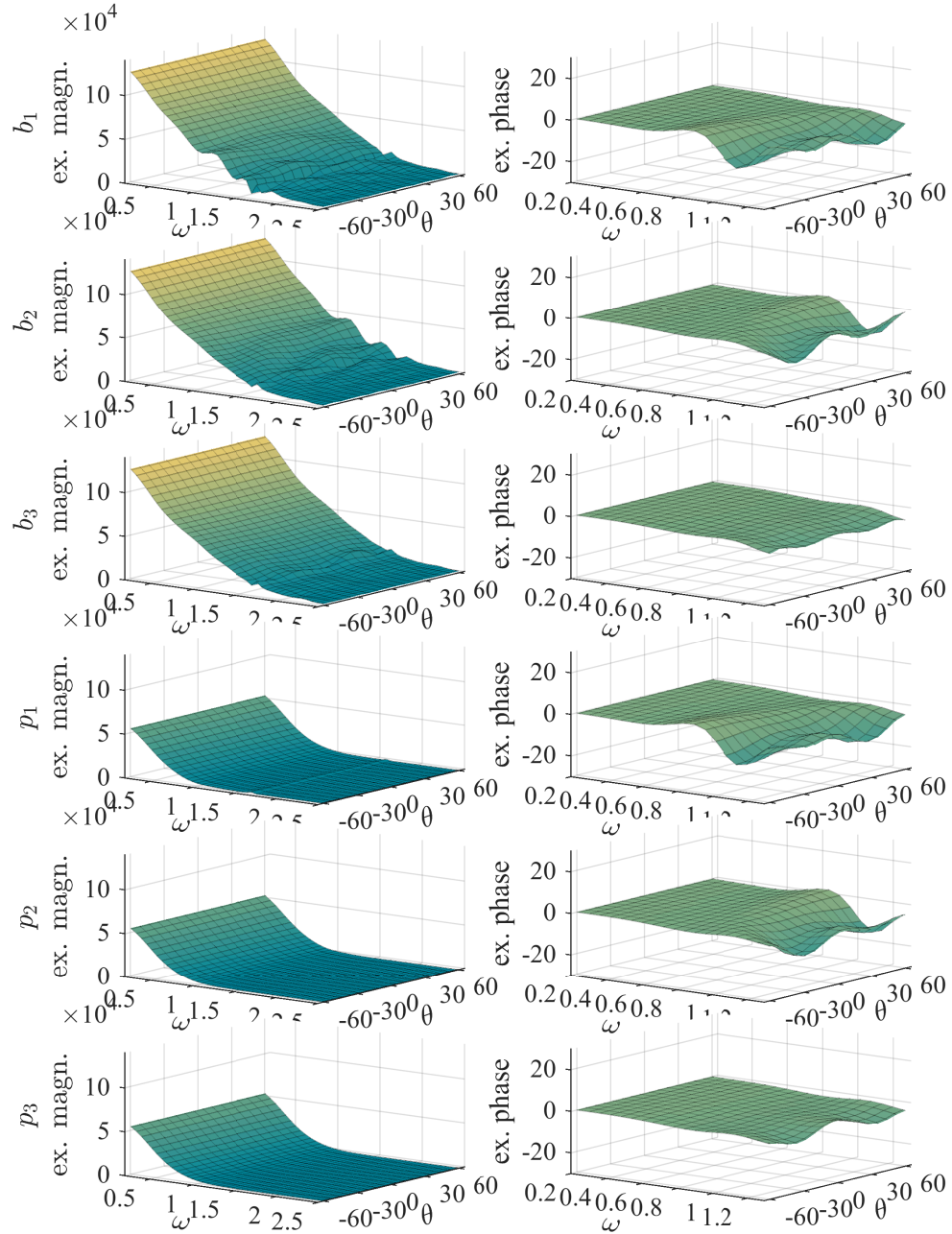
Figure 3.6: Excitation force magnitude and corresponding phase coefficients for the triangular OWC WEC array and the corresponding imaginary pistons.
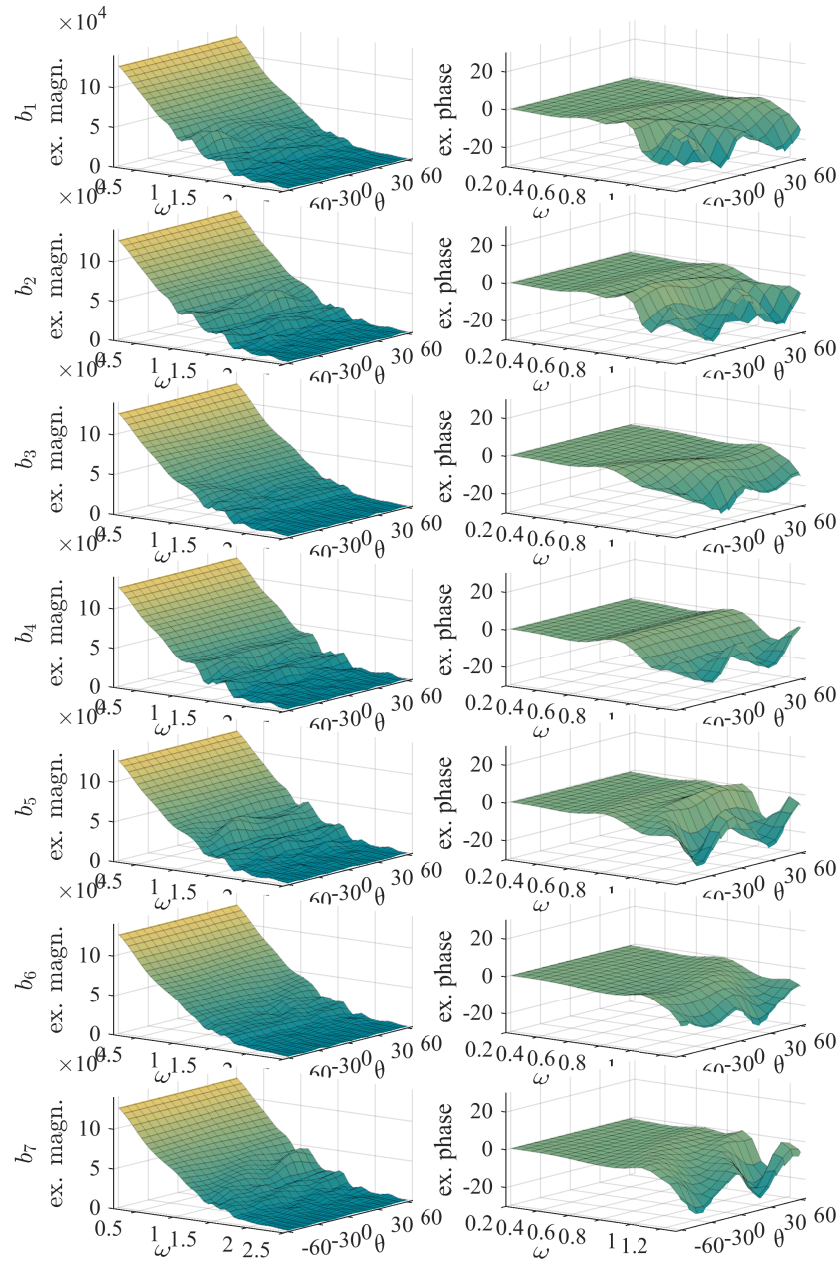
Figure 3.7: Excitation force magnitude and corresponding phase coefficients for the OWC WEC park.

where the incident wave angle is zero. The central WEC4 is axis symmetric with the surge axis. The excitation properties complete the linear hydrodynamic coefficients.

3.6   Summary

The hydrodynamic properties of the hexagon WEC park are approximated based on two BEM simulations. One including the results of the imaginary rigid pistons from the triangular WEC array and another one focusing on the diffraction effects among the WEC park in hexagon shape, with central WEC. With this method the limitations of ANSYS Aqwa are overcome and different park configurations can be approximated similarly based on sub-arrays. The time domain simulation of the derived system dynamics cannot be conducted with the BEM solver, due to too much detail in the air chamber and PTO dynamics.

Chapter 4 Numerical Experiments

The purpose of this chapter is to evaluate the dynamic model derived in Chap. 2 and hydrodynamically quantified in Chap. 3. There is no experimental data publicly available to validate the simulation results again and conducting physical experiments is far beyond the scope of this work. However, based on computer simulation experiments and comparing their outcome to the expectations a discussion why the results are acceptable is made. As time domain simulation environment MATLAB/Simulink is used. The simulations are first conducted without incoming waves and next with irregular waves.

4.1 Simulation Parameters

In table 4.1 the numerical values of important simulation parameters are listed. The mooring line parameters are oriented based on the work of Gomes et al. [26]. The net force of the inter-body mooring clump weights results from a bisection algorithm in order to balance equalize the mooring force in x-direction, when the WEC park is at it's initial position. The net force of the clump weight and the net force of the jumper of the bottom mooring lines parallel to the y-direction are then computed to balance the net mooring force in the sway direction. The turbine and generator parameters are taken from Carrelhas' work [4]. The capacity of the storage medium is chosen so

that it theoretically could maintain $14.4\,\mathrm{kW}$ for $20\,\mathrm{min}$.

4.2   Decay Tests

The first tests for the simulation models are conducted without incoming waves. Instead, an initial condition (IC) is used for a single state to observe how the energy dissipates or is converted into other states over time. Each of the following figures is the result of a different simulation run, illustrated mostly based on the quantities of WEC2, and in some cases states from different WECs to illustrate how the energy is transferred. The first test addresses the decay of the turbine generator set rotational speed in Fig. 4.1. The IC for the turbine rotational speed is set to its nominal speed $x^{\mathrm{IC}}_{\Omega,2} = 1470\,\mathrm{rpm}$. The generator is assumed to not to oppose any torque, but its inertia and friction is added to the turbine. The decaying rotational speed is illustrated in the first plot in Fig 4.1 and it is mostly caused by the turbine friction, as expected. In the second row, the ICs for the heave WECs position are slightly below the still water surface (dashed blue, because it equals the pistons IC). The displaced water equals the mass of all the attached mooring lines and therefore entire park is in equilibrium. The WECs have slightly different ICs, since they carry the mooring weight to a different extend. The third row contains the horizontal displacements of WEC2 and its rotational displacements. The WEC2 moves horizontally for about $1\,\mathrm{cm}$, which is insignificant compared to the WEC dimensions. Consequently, the horizontal components of the mooring force in the last plot appear to be zero compared to the vertical force component, which is constant since the heave position does not

Table 4.1: Numerical values of the simulation parameters

Quantity	sym/var	value
horizontal distance mooring anchor to WEC		$180\,\mathrm{m}$
length bottom mooring line 1	L_1	$153\,\mathrm{m}$
length bottom mooring line 2	L_2	$30\,\mathrm{m}$
length bottom mooring line 3	L_2	$52\,\mathrm{m}$
net force bottom mooring $\parallel x$ clump weight	F_C^x	$-26\,\mathrm{kN}$
net force bottom mooring $\parallel x$ jumper	F_J^x	$30\,\mathrm{kN}$
bottom mooring line weight per unit length	w_L	$34.82\,\mathrm{kg/m}$
length inter-body mooring	L_IB	$17\,\mathrm{m}$
inter-body mooring line weight per unit length	w_IB	$30.1\,\mathrm{kg/m}$
net force inter-body mooring clump weight	F_IB	$-20.388\,\mathrm{kN}$
net force bottom mooring $\parallel y$ clump weight	F_C^y	$-10.065\,\mathrm{kN}$
net force bottom mooring $\parallel y$ jumper	F_J^y	$21.1656\,\mathrm{kN}$
diameter turbine	d_t	$0.5\,\mathrm{m}$
MOI turbine	I_t	$5\,\mathrm{kg\,m^2}$
MOI generator	$I_\mathrm{t,gen}$	$0.24\,\mathrm{kg\,m^2}$
turbine and generator friction coeff. (assumed)	B_t	$0.03\,\mathrm{kg\,m/s^2}$
maximal generator torque	$T_\mathrm{gen}^\mathrm{max}$	$216.5\,\mathrm{N\,m}$
rated generator power	$P_\mathrm{gen}^\mathrm{rated}$	$30\,\mathrm{kW}$
maximal generator rotational speed	$\Omega_\mathrm{gen}^\mathrm{max}$	3000 rpm
power electronics efficiency	η_PE	$92.5\,\%$
storage medium efficiency	η_SM	$89.44\,\%$
rated capacity of the storage medium	$W_\mathrm{SM}^\mathrm{rated}$	$4.8\,\mathrm{kW\,h}$
Lower / Upper bound first derivative σ	K_m; K_M	30.9; 51.7
Upper bound second derivative σ	C_0	150
Linearity region	σ_0	$1\,\mathrm{rad/s}$
slope sgn and switch approx.	c_1; c_2	50 ; 10^5
SMC parameter	α; λ; γ	6; 8; 0.5

noticeably change over time. The horizontal displacement must results from the mooring system that is not in perfect equilibrium, but more than sufficient to not to unexpectedly alter the systems dynamics.

For the next decay test the IC for the heave position of WEC2 is set to be 3 m above the still water surface. The vertical displacement of WEC2 and its piston are illustrated in Fig. 4.2 in the first plot. The resulting oscillation decays by over 90% after 90 s in ten oscillations. This indicates that the natural period of the WEC is about 9 s. The motion of the WEC, clearly drives the motion of the piston. Some of the motion energy from WEC is radiated away to WEC1 and WEC4, illustrated in the second row of Fig. 4.2. However, note the y-axis scale. The oscillation is magnified six times. The horizontal and rotational displacements of WEC2 are illustrated in the third plot. The excitation of the surge displacement and the pitch rotation is explained with the mooring system. When only WEC2 is elevated not only the mooring force in vertical direction increases, but also the mooring force component in the x-direction and consequently a pitch torque as well. The vertical component mooring force in the last plot decays with the vertical displacement of WEC2. The behaviour of the decay from a horizontal displacement is presented in Fig. 4.3. The initial position of WEC is set to be additional 3 m from the central WEC, along the line through WEC2 and WEC4, thus $\Delta\hat{x}_2 = -2.6$ m and $\Delta\hat{y}_2 = 1.5$ m. Noticeable is that the horizontal positions decay about four times slower compared to the vertical position (illustrated in the first row of Fig. 4.3). The transfer to the motion to the other WECs is mostly due to the mooring force and to a lesser extent because of the radiation force. The second plot shows that first WEC1 and WEC4 are horizontally

displace in the direction of WEC and later the motion is transferred to WEC6, which is on he opposite end of the park (all WECs in the park are affected). The magnitude of yaw rotation (in dashdotted orange) in the third plot would not occur naturally. But it is an expected behaviour, because the initial displacement of WEC2 does not include an initial rotation. Therefore, the yaw angle of the fairleads is not aligned with the mooring lines initially and consequently the buoy experiences a torque about the yaw axis. The yaw rotation decays very slowly, since there is no restoring component. The mooring forces components in the last plot are somewhat proportional to the instantaneous horizontal, but strongly nonlinear. The last decay test investigates the behaviour for a pitch IC in Fig. 4.4, namely $\Delta \hat{r}_2^y = 15°$. Note that the right y-axis in the third row of Fig. 4.4 is changed compared to the previous plots. The first observation is the slight coupling between the pitch excitation and the resulting heave excitation, in the first row. The heave modes of the other WEC are excited to a lesser extend (about 10%, but noticeably). The strong coupling with the surge displacement $\hat{x}_2$ is again explained with the initial tension in the mooring system. When WEC2 is rotated about its center of gravity, the fairleads change their position and are not in equilibrium, although the CoG has not been initially displaced.

4.3   Irregular Waves Performance

In this section the excitation of the WEC park does not originate from its initial conditions, but from the simulated ocean waves. First, a single sea state is used to discuss the park behaviour, when exposed to a wave with significant wave height

$H_\text{s} = 2\,\text{m}$, peak energy period $T_\text{p} = 9\,\text{s}$ and a single incident wave angle $\theta_1 = 15°$. This sea state is important for the annual energy capturing in the wave climate of Leixões, Portugal [43]. The choice for the sea climate of Leixões, Portugal is based on the origin of the Marmok-A5 and the probability of sea state occurence is illustrated in Fig. 4.7. The first plot in Fig. 4.5 presents the free surface elevation at the location of WEC2. The resulting heave displacement is illustrated in the second plot for both the buoy and the piston of WEC2. Recall that the natural period of the WEC is somewhere around 9s, explaining the higher oscillation amplitude compared to the free surface elevation in many times.

The heave position of the WEC server array, namely WEC2, WEC4 and WEC5 are illustrated together in the third plot of Fig. 4.5. The signals are shifted in time, but only vary in the ballpark of 5% in their maximal values. To quantify the instantaneous WEC motion, a new quantity is introduced for the later following control design. Namely, the averaged, moving root-mean-square (RMS) value of the server array $\bar{z}_\text{server}^\text{RMS}$, which is illustrated on top of plot three in red and uses the right y-axis. Here, $\bar{z}_\text{server}^\text{RMS}$ will be used to quantify how well the entire WEC park responds to incoming waves over the last 30 seconds. Note that the RMS value has no relation to power and that the notation can be miss-leading, but satisfies it's purpose of being a measure to quantify and compare the WEC motion in the recent past. The last plot in Fig.4.5 shows that the mooring configuration does its job in keeping the WEC within a radius of $60\,\text{cm}$ of its horizontal origin and the rotation does not exceed $2°$. The next Fig. 4.6 is from the same simulation run with WECs heave displacement and $\bar{z}_\text{server}^\text{RMS}$ in the first plot, but the other quantities are exchanged. First, it has to be mentioned that,

although the control law has not been introduced yet, the turbine is controlled with the benchmark control law (6.1). Otherwise, the turbine would quickly accelerate above its maximal rotational speed. The rotational speed is illustrated in the last plot of Fig. 4.6. In the second plot all the forces acting on WEC2 are illustrated. The hydrostatic restoring force has an up to 5 times higher magnitude compared to the other significant forces, namely excitation force, pressure chamber force and mooring force. The viscous drag and the radiation force component due the velocity components are not noticeable with the naked eye. The radiation force component due to the acceleration cannot be decoupled from the other force (compare (2.81)). The resulting chamber pressure and the related turbine pressure head coefficient are illustrated in the third row in Fig. 4.6. After the turbine is up to speed after about 35 seconds a noticeable amount of air can flow through the turbine and consequently the relative chamber pressure oscillates within a reasonable range. The rotational speed decreases always when $\bar{z}_{\text{server}}^{\text{RMS}}$ decreases. This time behaviour shows that different phases of WEC resonance can occur within minutes in the same sea state. This brings up the idea to control the WEC differently in the time intervals of low WEC response, as if it would be a different operating regime. The results from a previous study show that it can be beneficial to follow a constant rotational speed in low energetic sea state [18]. As last part of the irregular wave numerical experiments, time domain simulations with a simulation time of 20 minutes, or 1200 seconds are conducted in every sea state representative of the climate in Leixões, Portugal. The

performance is investigated based on the time averaged mechanical power

$$\bar{P}_{\text{mech}} = \frac{1}{1200 - 20} \int_{20}^{1200} T_{\text{gen}} x_\Omega \mathrm{d}t. \tag{4.1}$$

The power results for different incident wave angles are illustrated in Fig. 4.8. The color shading of the bivariate plots represent the array interaction factor q (compare Sec. 1.5.1). To obtain the the interaction factor, a simulation model with a single WEC in all DoF had to be built. The main difference (except, obviously, the missing WECs and consequently the missing interactions) is that the single WEC does not use interbody mooring cable, but the same bottom mooring cables with lighter clump weights. If the power number is written with black font $q > 1$ and if it is written in white $q < 1$. The results show that especially in sea states with higher wave heights the park performs worse compared to the same amount of isolated WECs. However, this study does not look into survivability and violating the constraints of the physical components yet. The nature of the WEC park might be beneficial in regards to a safe operation.
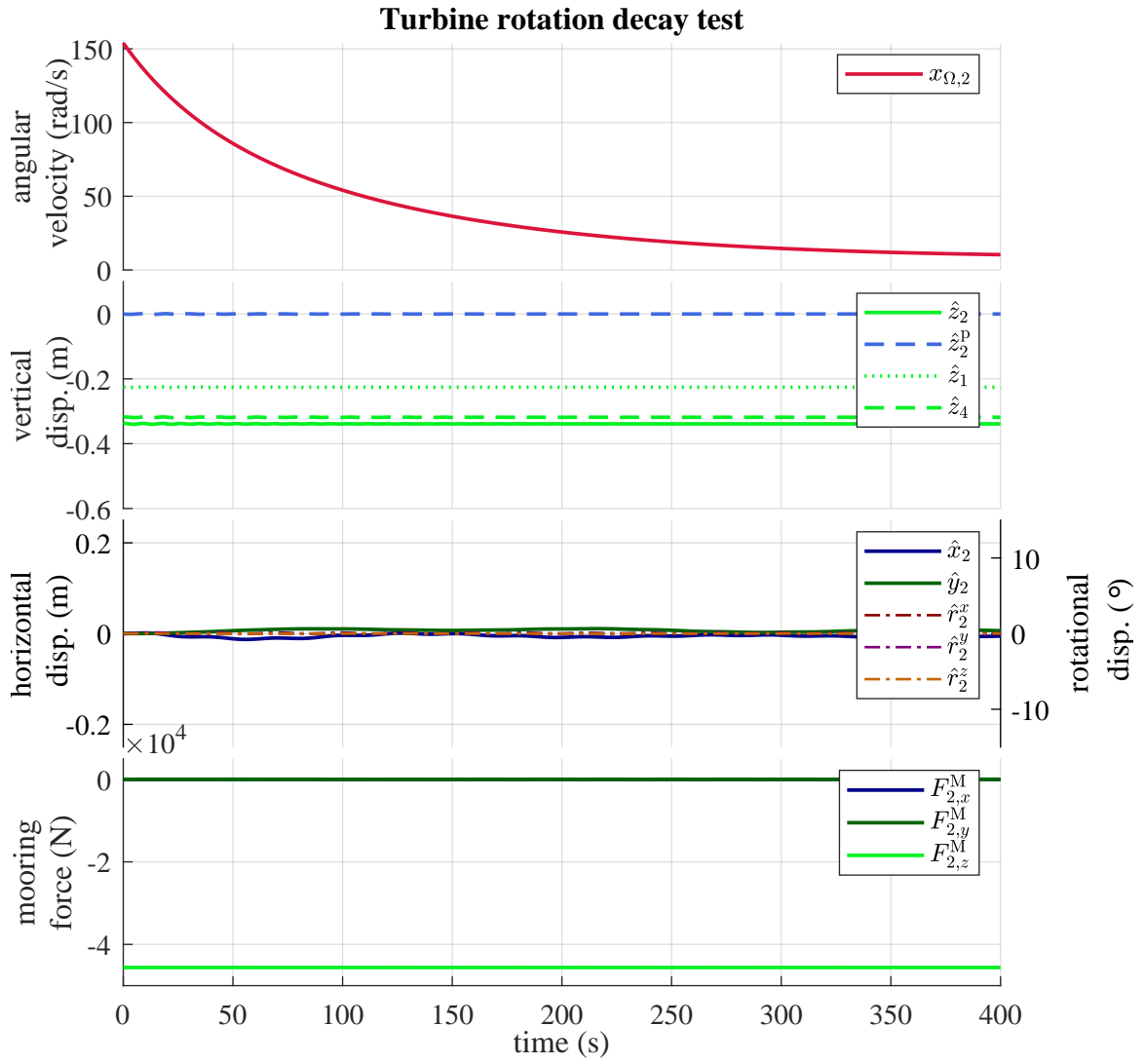
Figure 4.1: Decay test for turbine rotational speed WEC2, with $x_{\Omega,2}^{\mathrm{IC}} = 1470\,\mathrm{rpm}$
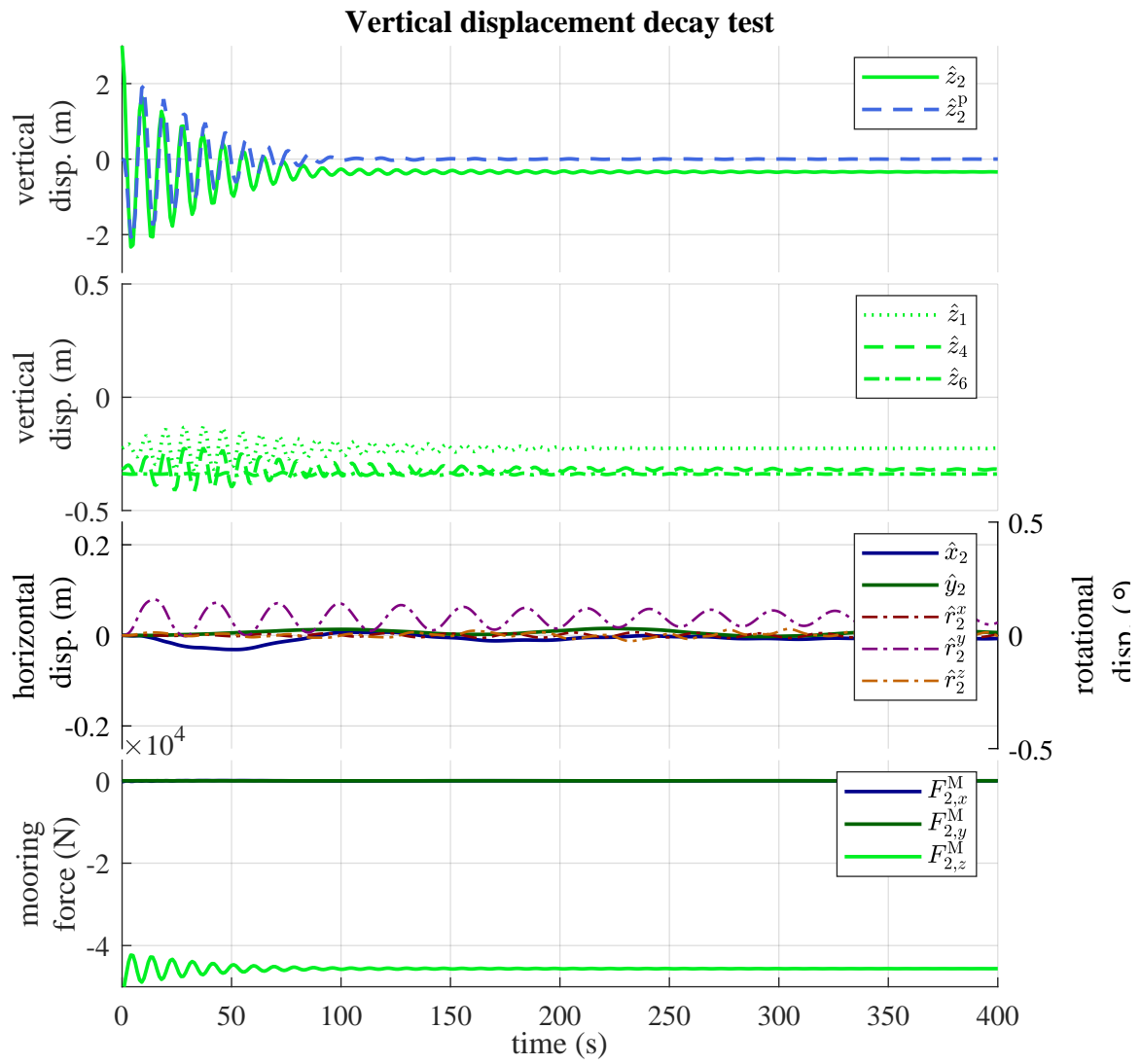
Figure 4.2: Decay test for vertically displaced WEC2, with $z_2 = 3\,\mathrm{m}$.
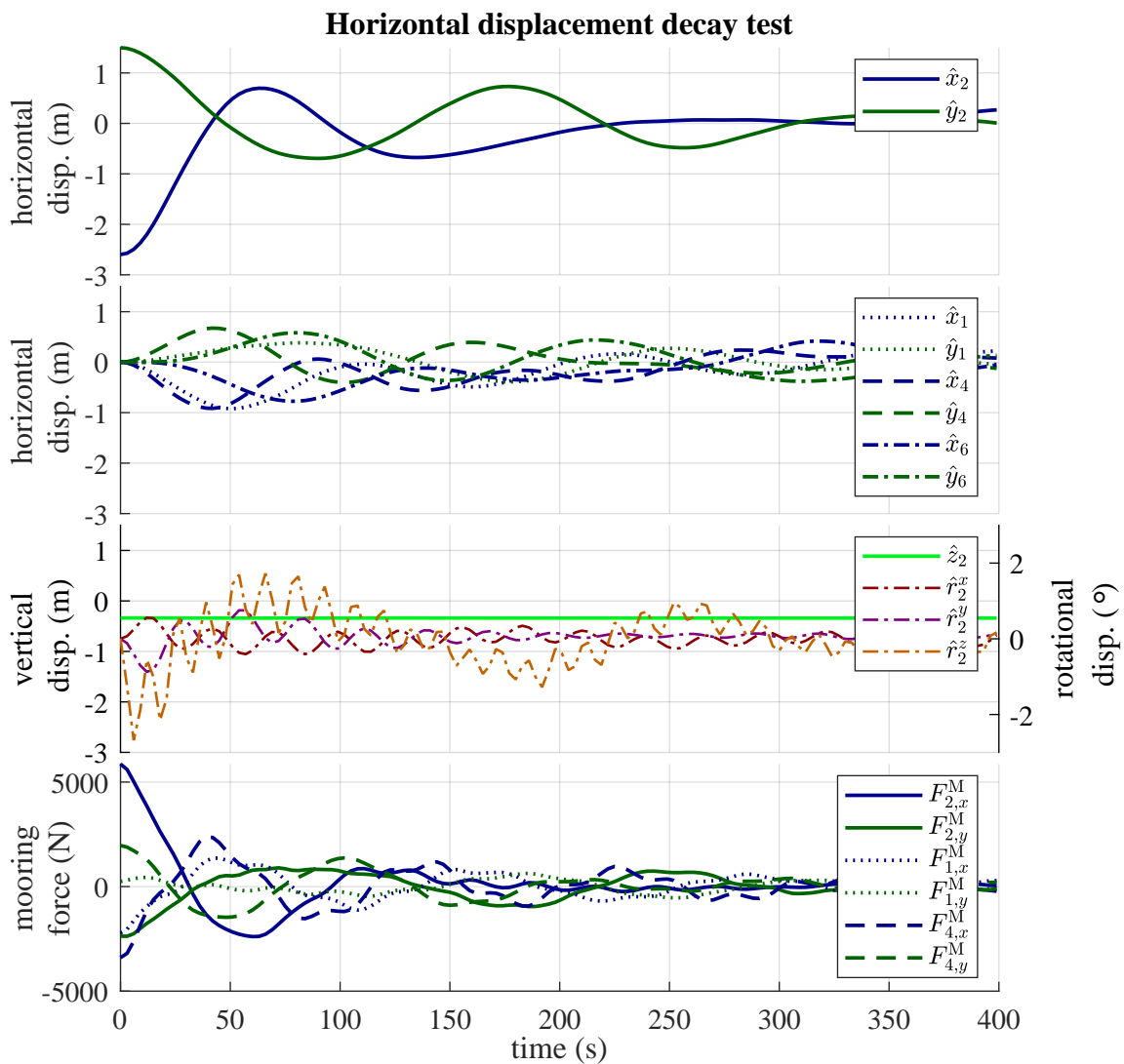
Figure 4.3: Decay test for horizontally displaced WEC2, with $\Delta\hat{x}_2 = -2.6\,\mathrm{m}$ and $\Delta\hat{y}_2 = 1.5\,\mathrm{m}$
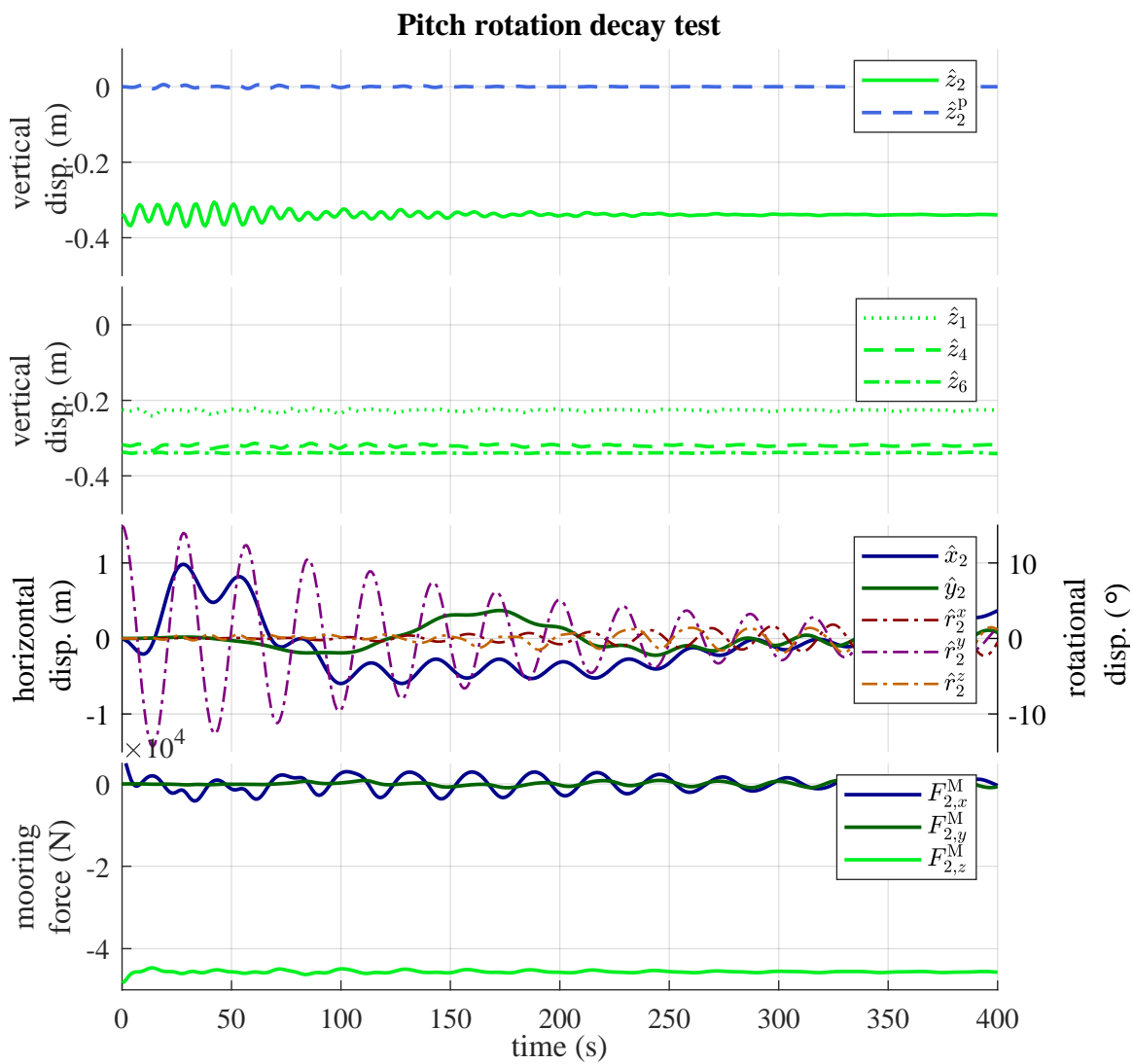
Figure 4.4: Decay test for pitch rotated WEC2, with $\Delta \hat{r}_2^y = 15°$.
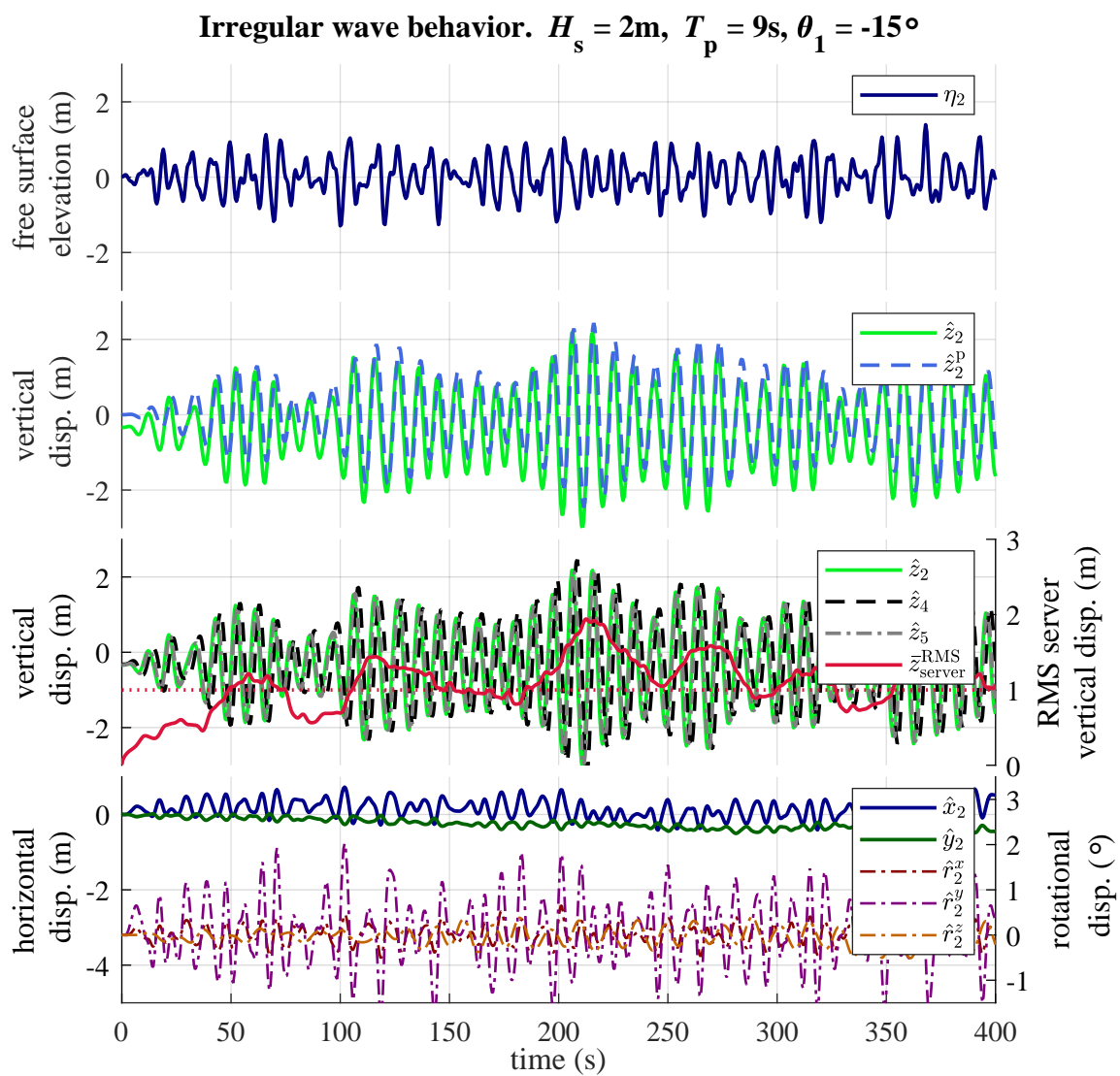
Figure 4.5: Time series of WEC displacements exposed to an irregular wave.
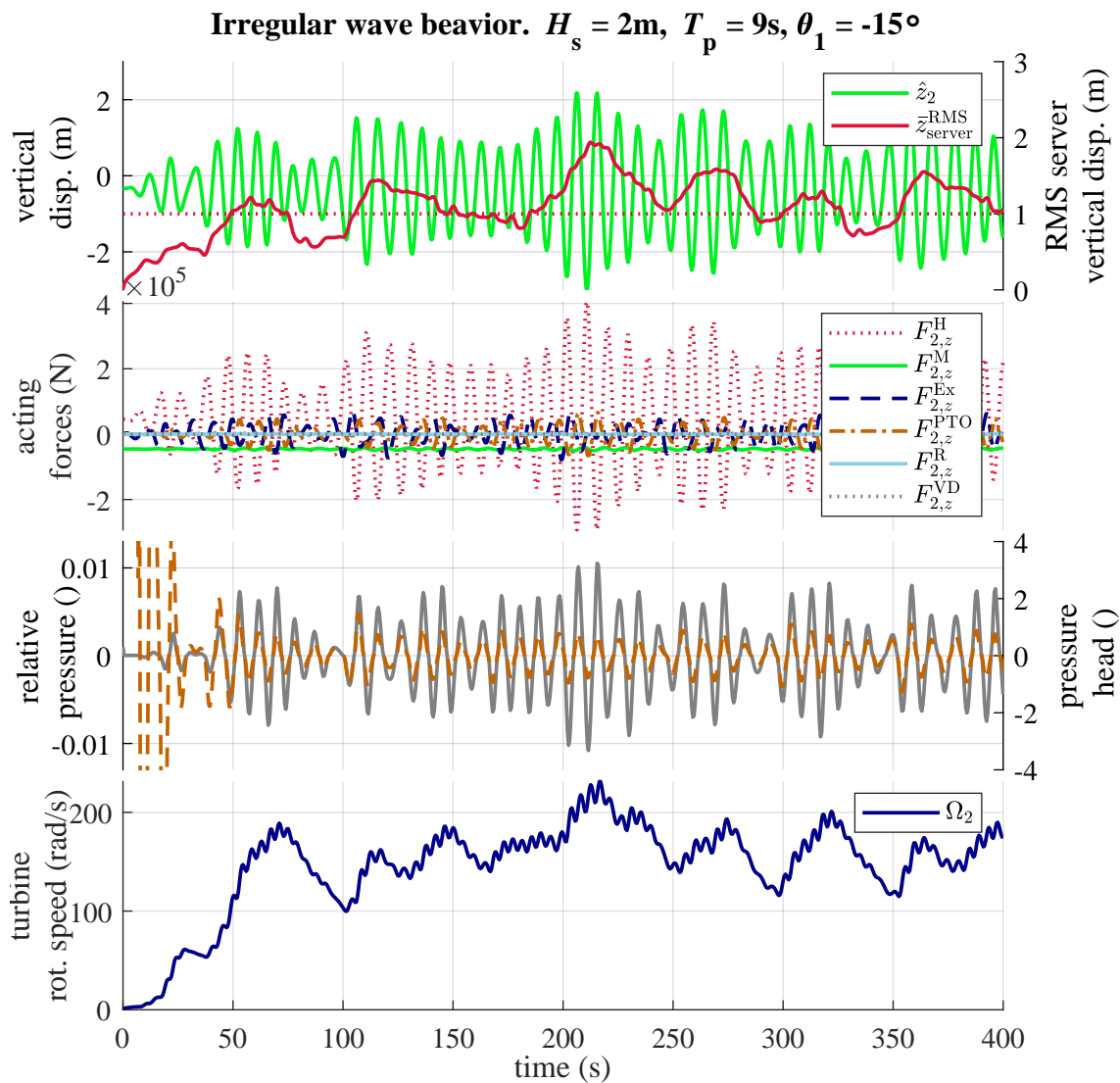
Figure 4.6: Time series of the acting forces and the turbine quantities of WEC2 exposed to an irregular wave.
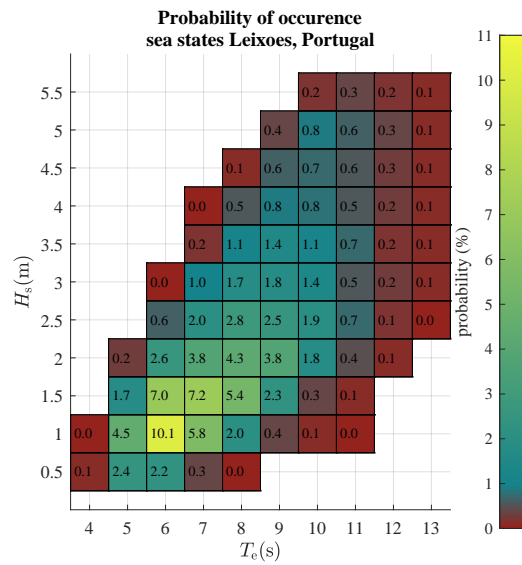
Figure 4.7: Scatter plot of probabilities of occurrence for the most representative sea states off Leixões, Portugal. Adapted from [43].
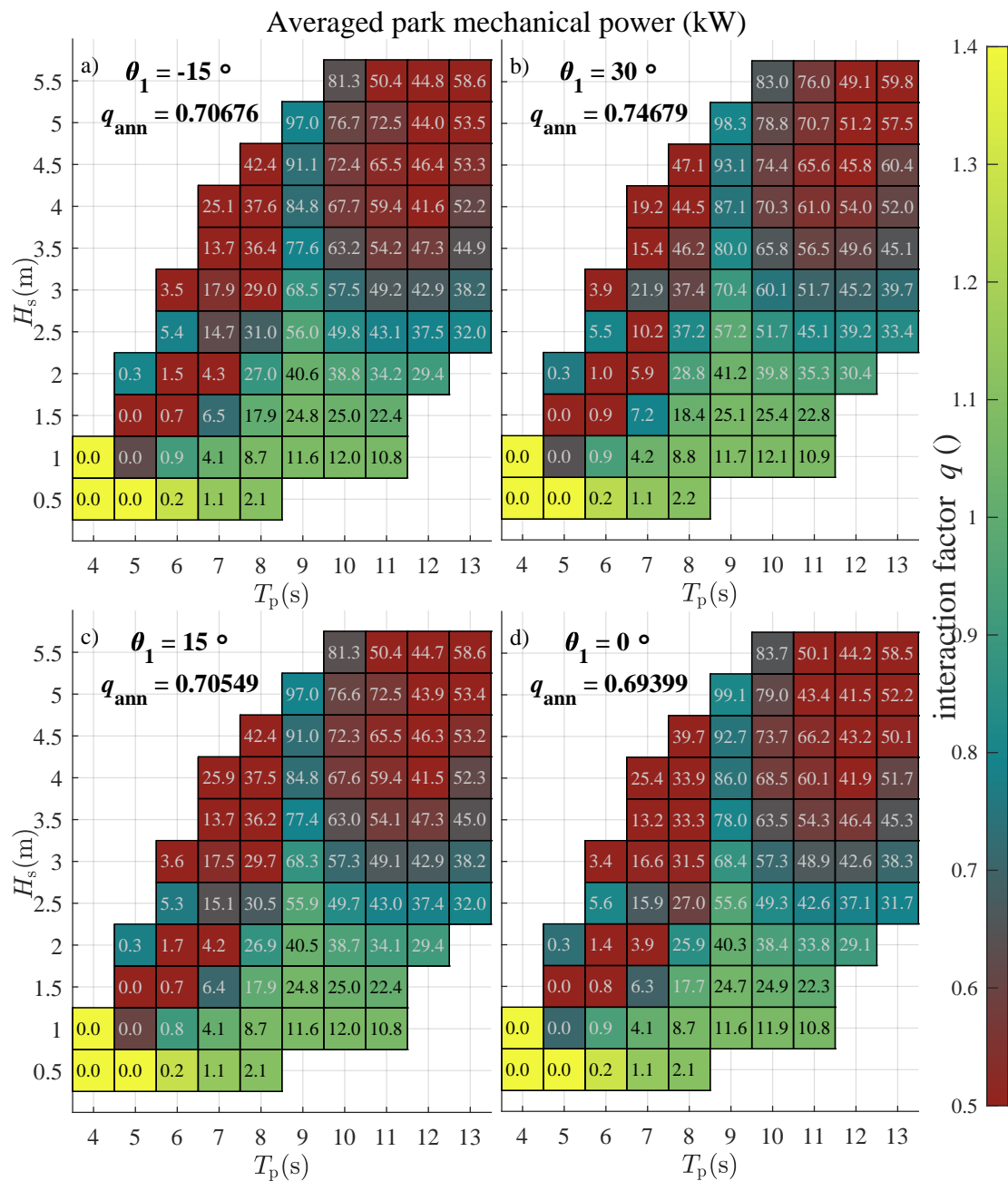
Figure 4.8: Average mechanic park power (turbine power) in the wave climate of Leixões, Portugal. The color/shading indicates the q-factor.

Chapter 5   Discrete Event Model

The previous chapter showed that different phases of resonance occur within minutes in the same sea state. This brings up the idea to implement different operating regimes, since in low energetic sea states a reference velocity enforcing control algorithm has shown to improve the power capturing [17]. Furthermore, in times of high WEC response the physical constraints of the components could be violated and would require an extreme conditions operating regimes. To identify different global and local operating regimes it requires some kind of of observer and to enable different controllers it will require a supervisory controller on top of the local controllers.

A supervisory control based on the concept of discrete-event systems (DES) naturally yields a hierarchical structure, due to the abstraction of the lower levels for the higher levels (compare Fig. 6.5). Furthermore, each level of control causes an allowable range of operation for the lower levels [45]. The DES itself evolves with the occurrence of *events* [44], one example would be if the generator exceeds its maximal admissible rotational speed. When looking at the state space time domain simulation model from this perspective, the continuous dynamics between events are unimportant. The discrete states from the set Q of a DES should not be confused with state space states with a clear physical meaning. The discrete states rather describe an operating regime of the WEC. The possible paths of discrete states via events is illustrated in Fig. 5.1 for the entire (controlled) WEC park.

5.1   OWC park Automaton

The Automaton G_i describes the discrete event dynamics of the WEC i in the WEC park, including the local controllers that are designed in Chap. 6. The park Automaton $\boldsymbol{G}$ is extended from the work of Bratcu et. al., modelling the behaviour of a wind turbine for safe and optimal operation [2]. Note that the Automaton in Fig. 5.1 is vectorized, i.e. bold face indicates a vector of states or events with each entry accounting for a single WEC. Clearly, different WECs can be in different states at the same instance of time. A few uncontrollable events, namely u_1, u_2 and u_4 are effective globally. The controllable event c_{3C} can only be activated for the WECs in the client part of the array, thus the state RFSMC can only be reached by such, since the server array determines the reference velocity. The functional states are all indicated by the box around them, and identified as,

WT	Waiting
S	Start
RFSMC	Reference following with SMC
IDFB	Ideal Feedback control
IDFB HSSV	Ideal FB control with HSSV
BRK	Break sequence
BRKT	Break sequence timer
STOP	Stop park
IMF	Irreversible mechanical failure
IEF	Irreversible electrical failure

Those states describe the possible behavior of an OWC WEC. Note that discrete states such as vibrations or parametric resonance could be easily included in the
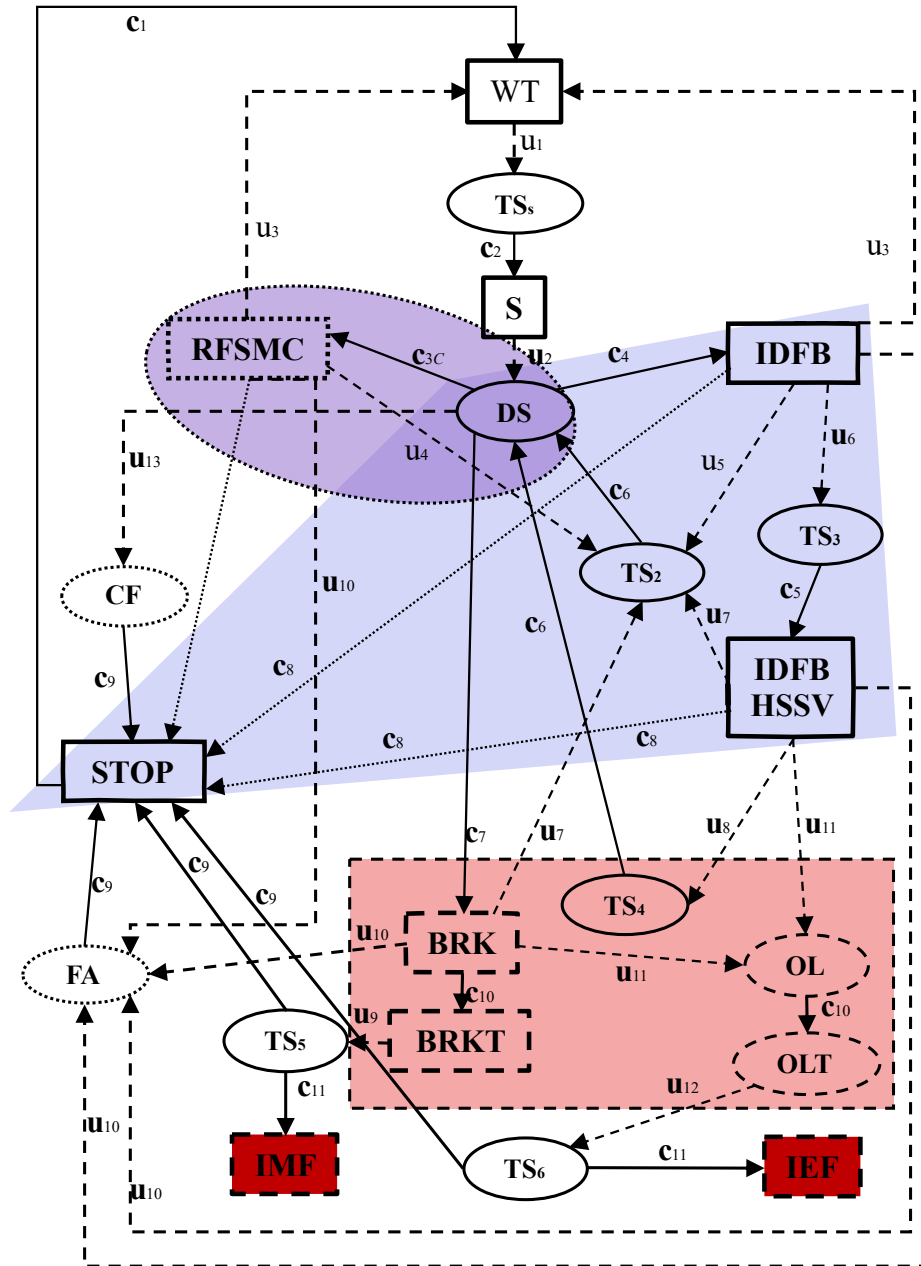
Figure 5.1: Discrete event model of the WEC park G, including centralized controllers.

Automaton, but since the developed time domain model is not capable of simulating such effects, they are neglected. The states contained in the blue trapezoid and the purple ellipsoid represent the desired behavior of the system will be referred to as marked states $Q_{\mathrm{m},i}$. The marked states $Q_{\mathrm{m},i} \subset Q_i$ model a cyclic working process and all but the STOP state are the functional states responsible for power conversion. The STOP state needs to be accessible from all other states, in case of a manual shut down of the WEC, through the controllable event $c_{8,i}$. A safe operation of the automaton is achieved if the catastrophic state IMF and IEF are prevented. Let us define the desired states $Q_{\mathrm{D},i} = Q_i - \{\mathrm{IMF}_i, \mathrm{IEF}_i\}$.

The states inside the red rectangle are states of extreme operation and are only admissible for a limited amount of time, thus the corresponding timing states. The overload state OL is not a functional state, in the sense that no controller can prevent electrical overload once it occurs (all local controllers have protection mechanisms included to avoid overload, so if OL is reached, the local controller failed).

Let us introduce transition states to model the time for decision making of the supervisor (here one time step) and to break algebraic loops, since e.g. the position of the stop valve is used to determine a discrete state, but is also a control output at the same time. Therefore, the temporary states,

DS Decision state
CF Control failure
FA Failure
TS Transition states
OL Overload state

are used. The events that the actuators in the WEC can control are called controllable events $\Sigma_{c,i}$:

c_1 WEC activation

c_2 Start power conversion

c_3 Enable reference following control (SMC)

c_4 Enable Ideal Feedback (FB) control

c_5 Enable FB and HSSV control

c_6 Disable current controller

c_7 Enable break sequence

c_8 Manual stop

c_9 Emergency stop

c_{10} Start counting

c_{11} Continue counting

The behaviour of the discrete model is complete with the uncontrollable events $\Sigma_{u,i}$:

u_1 Enough WEC heave motion (global)

u_2 Turbine rotation > min. generator speed

u_3 Not enough WEC heave motion (global)

u_4 Medium-High WEC heave motion (global)

u_5 Low WEC heave motion (global)

u_6 Turbine at 90% max. generator speed

u_7 Turbine below 90% max. generator speed

u_8 Turbine over max. speed

u_9 Half of time over max. speed passed

u_{10} Functional failure

u_{11} Half of admissible time in overload passed

u_{12} No suitable controller found

This yields the set of all events $\Sigma_i = \Sigma_{c,i} \cup \Sigma_{u,i}$. To describe the transition between the states in Q_i via the events in Σ_i, the transition function $\delta_i : Q_i \times \Sigma_i \to Q_i$ is used. Note, that the event c_{3C} is blocked for the server array. Uncontrollable events are always enabled to occur. This fully describes the automaton for each WEC

$$G_i = (Q_i, \Sigma_i, \delta_i, q_0, Q_{m,i}), \tag{5.1}$$

with the initial state q_0 being the STOP state for the entire park.

Chapter 6   Control Design

The purpose of the control algorithms for WECs is almost always to maximize energy absorption from the incoming waves, subject to the WEC dynamics and the physical limitations of the device and the actuators [20]. A challenge for floating OWCs is that the turbine pressure head versus flow rate is nearly quadratic which implies that the turbine rotational speed barely affects the hydrodynamic process of the WEC [5]. Consequently, this work focuses on improving the electro-mechanical energy conversion instead, while maintaining safe operation, without damaging the actuators and electric components. This is done with a supervisory controller, which sits on a higher hierarchical level than the local controller on WEC i. The supervisor switches between different local control strategies for the control inputs, namely, the generator torque $u_{\mathrm{gen},i} = T_{\mathrm{gen},i}$ and the position of the High Speed Stop Valve $u_{\mathrm{HSSV},i} = p_{\mathrm{HSSV},i}$. The supervisor also decides if the WEC park is run at a constant base load for the grid load control input $u_{\mathrm{load}} = P_{\mathrm{load}}$, or if more or less power needs to be transmitted to the grid depending on the battery state of charge and the current park performance.

6.1   Local Control

In this section the actual numeric values for the control inputs $u_{\mathrm{gen},i}$, $u_{\mathrm{HSSV},i}$ and u_{load} are quantified. Every algorithm has protection mechanisms to not to exceed the
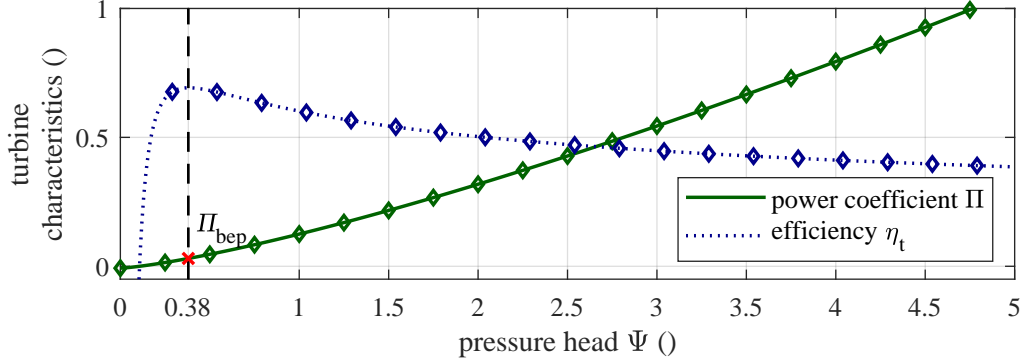
Figure 6.1: Dimensionless turbine characteristics for an open HSSV, with the best efficiency point indicated.

actuators limitation incorporated.

6.1.1 Feedback Control Law Optimizing Pneumatic Efficiency

Henriques et. al. present an ideal feedback control for the generator torque based on the instantaneous angular velocity for practical use [30, 29], namely,

$$u_{\text{gen},i}^{\text{IDFB}} = \min\left(a_{\text{bep}}x_{\Omega,i}^2, \ \frac{P_{\text{gen}}^{\text{rated}}}{x_{\Omega,i}}, \ T_{\text{gen}}^{\text{max}}\right). \tag{6.1}$$

It is ideal in terms of the maximization of the aerodynamic efficiency of a fixed OWC which runs the identical biradial turbine and limited by the physical generator constraints, namely the rated power $P_{\text{gen}}^{\text{rated}}$ and the maximal generator torque $T_{\text{gen}}^{\text{max}}$. To determine the parameter a_{bep} at the best efficiency point, let us use $\Pi(\Psi_{\text{bep}})$

(compare 6.1) and rearrange the turbine torque equation (2.74),

$$a_{\text{bep}} x_{\Omega,i}^2 = \underbrace{\rho_{\text{at}} d_{\text{turb}}^5 \Pi(\Psi_{\text{bep}})}_{a_{\text{bep}}} x_\Omega^2, \tag{6.2}$$

and use the the atmospheric density as reference density. This generator control will function as benchmark in the time domain simulation.

6.1.2 Second-Order Sliding Mode Generator Control

In preliminary work different second-order SMC controllers that are tuned for the OWC array equipped with biradial turbines and the constraint to the maximal torque are presented [19]. The four algorithms are derived after the example of the fundamental work from [35]. For this work the controller with the smoothest control signal is chosen, a second-order SMC approach with a prescribed law of variance (PLV) that calculates the generator torque T_{gen} based on the rotational speed x_Ω and its time derivative $\dot{x}_\Omega$ to follow a reference angular velocity Ω_{ref}. This allows the generator to operate efficiently in terms of electric energy conversion as soon as there is a pressure difference in the air chamber. The turbine torque is considered a disturbance for the SMC algorithm and the maximal expected disturbance needs to be estimated to tune the control parameters.

6.1.3 SMC Derivation

Starting with the entire system dynamics (2.81) which are rewritten as

$$\dot{\boldsymbol{x}} = \boldsymbol{f}(\boldsymbol{x}(t), u_{\text{gen}}, u_{\text{HSSV}}), \tag{6.3}$$

where $\boldsymbol{f}$ satisfies class C^1. A real generator is physically constrained to a maximal value $T_{\text{gen}}^{\text{max}}$, thus the dimensionless control input $u = u_{\text{gen}}/T_{\text{gen}}^{\text{max}}$ is introduced and the SMC is designed s.t. it will keep $|u| \leq 1$. Let us define the sliding surface in terms of the control error between the constant reference rotational speed Ω_{ref} and the instantaneous rotational speed,

$$\boldsymbol{\sigma}(t, \boldsymbol{x}) = \Omega_{\text{ref}} - \boldsymbol{x}_\Omega. \tag{6.4}$$

The sliding variable $\sigma(t, \boldsymbol{x})$ is of class C^2. The differential operator considering u constant

$$\mathcal{L}_u = \frac{\partial}{\partial t}(\cdot) + \frac{\partial}{\partial \boldsymbol{x}}(\cdot) \boldsymbol{f}(\boldsymbol{x}, \boldsymbol{u}_{\text{gen}}, \boldsymbol{u}_{\text{HSSV}}), \tag{6.5}$$

represents the total derivative with respect to (6.3). Let us define

$$\dot{\boldsymbol{\sigma}}(t, \boldsymbol{x}, u) = \mathcal{L}_u \boldsymbol{\sigma}(t, \boldsymbol{x}) = -\dot{\boldsymbol{x}}_\Omega. \tag{6.6}$$

Now assume there exists a set $\{t, \boldsymbol{x}, u\} : |\sigma_i(t, x)| < \sigma_0$, where σ_0 is called the linearity region, such that

$$0 < K_{\text{m}} < \left| \frac{\partial \dot{\sigma}_i}{\partial u} \right| < K_{\text{M}}. \tag{6.7}$$

With the positive constants K_{m} and K_{M}. Moreover, boundedness of the second derivative of the sliding surface is required, namely,

$$|\mathcal{L}_u \mathcal{L}_u \sigma_i(t, x)| < C_0. \tag{6.8}$$

If the assumptions of the bounded derivatives (6.7) and (6.8) are satisfied, the PLV algorithm [35] drives σ and $\dot{\sigma}$ towards 0 and makes the system dynamics follow the reference velocity with a smooth control input signal. This PLV algorithm computes the time rate of change of u_i, namely,

$$\dot{u}_i = \begin{cases} -u_i, & \text{if } |u_i| > c_{\mathrm{sw},i} \\ -\alpha \operatorname{sgn}(\dot{\sigma}_i - g(\sigma_i)) & \text{if } |u_i| \leq c_{\mathrm{sw},i}. \end{cases} \tag{6.9}$$

The choice of function $g(\sigma_i) = -\lambda \operatorname{sgn} \sigma_i |\sigma_i|^\gamma$, with $\lambda > 0$, $0.5 \leq \gamma < 1$ and

$$\alpha > \left(C_0 + \sup g'(\sigma_i) g(\sigma_i)\right)/K_{\mathrm{m}} \tag{6.10}$$

is a sufficient condition for convergence to the sliding surface [61]. The switching variable $c_{\mathrm{sw},i}$ limits the area of regular operation, since the control effort is opposed as soon as $|u_i| > c_{\mathrm{sw},i}$. Here, $c_{\mathrm{sw},i}$ is used to respect the physical generator constraints, thus

$$c_{\mathrm{sw},i} = \min\left(1, P_{\mathrm{rated}}^{\mathrm{gen}}/(T_{\mathrm{gen}}^{\mathrm{max}} x_{\Omega,i})\right), \tag{6.11}$$

and therefore $u_{\text{gen}} \leq \min(T_{\text{gen}}^{\max}, P_{\text{rated}}^{\text{gen}}/x_{\Omega,i})$. After time integration and scaling with the maximal generator torque the control signal for the generator is obtained,

$$u_{\text{gen},i}^{\text{SMC}} = T_{\text{gen}}^{\max} \int \dot{u}_i dt. \tag{6.12}$$

From the definition of the sliding surface (6.4) and the requirement of $\dot{\sigma}$ in the control algorithm (6.12) it follows that the controller needs knowledge of $\dot{x}_{\Omega,i}(t)$ in eq. (2.67) and therefore the rotational speed $x_{\Omega,i}(t)$ needs to be measured as well as the relative air pressure inside the chamber $x_{p^*,i}(t)$ to use the turbine dynamics to estimate the instantaneous $T_{\text{turb},i}$. An alternative that does not require $\dot{x}_{\Omega}$, namely a super twisting sliding mode controller from [35], is previously proposed, for the Marmok-A-5 equipped with the biradial turbine [17]. But its control signal is less smooth and it overshoots after the torque limit is reached.

6.1.3.1   PLV Controller Parameters

The numerical values for the controller parameters α, λ and γ, which are based on the bounds K_{m}, K_{M} and C_0, that bound the disturbances, are given in table 4.1 and the reference rotational speed is

The change rate of (6.6) with respect to the input is

$$\frac{\partial \dot{\sigma}}{\partial u} = \frac{T_{\text{gen}}^{\max}}{J} \tag{6.13}$$

and $K_{\text{m}} = 0.75|T_{\text{gen}}^{\max}|/J$ and $K_{\text{M}} = 1.25|T_{\text{gen}}^{\max}|/J$ is chosen. For the second derivative

let us assume the density of the mass flow (2.63) to be constant, due to the fact that it only changes slightly when alternating for an inhalation or an exhalation, but it simplifies the analytical derivation. Consequently,

$$\ddot{\sigma} = \mathcal{L}_u \mathcal{L}_u \sigma(t, x) \tag{6.14}$$

$$= \underbrace{-J^{-1}\left(\frac{\partial T_{\text{turb}}}{\partial t} + \frac{\partial T_{\text{turb}}}{\partial x_{p^*}}\dot{x}_{p^*} + \frac{\partial T_{\text{turb}}}{\partial x_\Omega}\dot{x}_\Omega - 2B\dot{x}_\Omega\right)}_{C(x,u)} + \frac{T_{\text{gen}}^{\max}}{J}\dot{u}. \tag{6.15}$$

To identify the partial derivatives of the turbine torque, the partial derivatives of the power coefficient Π are required, which finally are a function of $\partial\Pi/\partial\Psi$, $\partial\Psi/\partial x_{p^*}$, $\partial\Psi/\partial x_\Omega$ and $\partial\Psi/\partial t$. Theoretically $C(x,u)$ is radially unbounded, however, with previous simulation of the park and knowledge of the subspace of the state space that is reached by the park of OWCs, an upper bound C_0 can be computed numerically. Therefore the expected disturbance that will occur to push the system dynamics of the sliding surface is estimated. The choice of $\gamma = 0.5$ and the combination $\alpha = 6$ and $\lambda = 8$ satisfies the inequality (6.10).

6.1.4   Valve Control

The high speed stop valve (HSSV) can limit or cut off airflow through the turbine and consequently reduce conversion between pneumatic and mechanical power. This power shedding is useful in times when the mechanical power would exceed the generator constraints. Previously, the HSSV is closed entirely when $\Omega_{\text{gen}}^{\max}$ is reached [29]. But, the generator efficiency map in Fig. 2.9 indicates that the efficiency η_{gen} is

dropping significantly beyond $0.9\,\Omega_{\text{gen}}^{\text{max}}$. Therefore, the HSSV control used here, limits the mechanical power by partially closing the HSSV, which is physically possible between 0.4 (40% open) and 1 (open), for an efficient electro-mechanical conversion. A closure > 0 and < 0.4 is physically not possible, since the pressure due to the restricted cross-area is too low for the HSSV to maintain its position, thus it needs to be closed entirely. When the HSSV position control is activated a straight forward proportional-integral (PI) controller with anti wind up structure to maintain $0.9\,\Omega_{\text{gen}}^{\text{max}}$ is used while possible within the HSSV constraints. Let us define the control error

$$e_{\Omega,i}(t) = 0.9\Omega_{\text{gen}}^{\text{max}} - x_{\Omega,i}(t). \tag{6.16}$$

The integrators initial condition is one and is reset on every new activation. The resulting control law in terms of the anti-wind-up cases is,

$$u_{\text{HSSV},i} = \begin{cases} K_{\text{p}}e_{\Omega,i} + \int K_{\text{i}}e_{\Omega,i}, & \text{if } 0.4 < u_{\text{HSSV},i} < 1 \\[2mm] K_{\text{p}}e_{\Omega,i} + \int \left(K_{\text{i}}e_{\Omega,i} - K_{\text{WU}}(u_{\text{HSSV},i} - 0.4)\right), & \text{if } u_{\text{HSSV},i} \leq 0.4 \\[2mm] K_{\text{p}}e_{\Omega,i} + \int \left(K_{\text{i}}e_{\Omega,i} - K_{\text{WU}}(u_{\text{HSSV},i} - 1)\right), & \text{if } u_{\text{HSSV},i} \geq 0.9 \geq 1 \end{cases} \tag{6.17}$$

Here the constant K_{p}, K_{i} , K_{WU} denote the proportional, integral and anti-wind-up gain, respectively.

6.1.5 Grid Load Control

The command for the power available for grid transmission u_{load} follows one of three cases. The first case, thereafter called the default case, outputs a constant power predefined based on the significant wave height and the peak energy period, which could be forecasted hours or even days in advance. The second case is a protection mechanism for the ES. This case is active if the ES cannot store the excess power of the park, while the default constant power is delivered to the grid. Consequently, more than the default power needs to flow into the grid and it will never get the ES full. This yields two conditions for the second case: The ES is *almost full AND* the current WEC motion response is *high*. The last case is activated when the ES is *almost empty* (close to its lower threshold of the effective storage) *AND* the current WEC motion is *low*, consequently the WECs cannot meet the default grid load.

$$
u_{\text{load}} = \begin{cases} P_{\text{base}}^{\text{grid}}(H_{\text{s}}, T_{\text{p}}) & \text{default} \\ P_{\text{base}}^{\text{grid}}(H_{\text{s}}, T_{\text{p}})\left(\frac{0.1}{1-x_{\text{SOC}}} - 1\right) & x_{\text{SOC}} \geq 0.9 \,\&\, \bar{z}_{\text{server}}^{\text{RMS}} \geq 1 \\ P_{\text{base}}^{\text{grid}}(H_{\text{s}}, T_{\text{p}})\left(10x_{\text{SOC}} - 1\right) & x_{\text{SOC}} \leq 0.2 \end{cases} \tag{6.18}
$$

Here, the base load is a function of the very first equation in this thesis. Namely, the theoretical wave energy P_{w} per meter wave crest (1.1), with an assumed wave to wire efficiency of 30% and the buoys diameter d_{p} as reference length, but limited to 85 kW. This yields,

$$
P_{\text{base}}^{\text{grid}}(H_{\text{s}}, T_{\text{p}}) = \min\left(0.3 d_{\text{p}} P_{\text{w}}(H_{\text{s}}, T_{\text{p}}), 85\text{e}3\right). \tag{6.19}
$$

The resulting grid base loads are illustrated in the scatter plot in Fig. 6.2. Note,
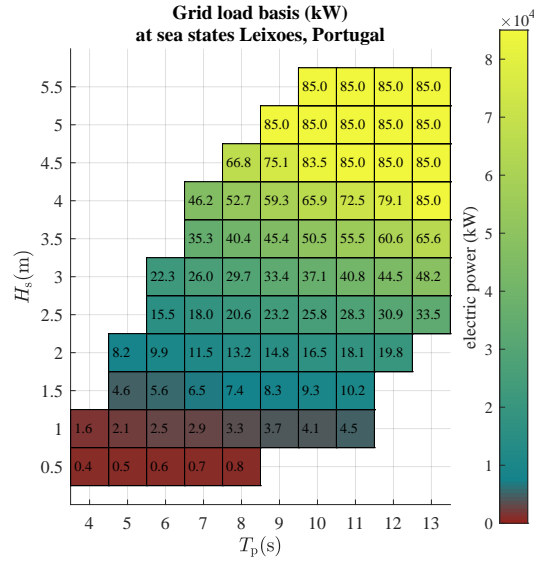
Figure 6.2: Grid base load $P_{\text{base}}^{\text{grid}}(H_{\text{s}}, T_{\text{p}})$ depending on the significant wave height and the peak energy period for the grid control.

that the load in the last case in (6.18) is zero if $x_{\text{SOC}} = 0.1$, thus it prevents the charge from falling significantly lower. The conditions could be realized with a fuzzy logic, but in this work a supervisory control approach is used, since the global state of charge and the respective WEC motion are used to determine the event discrete park state.

6.2 Reference Speed Generation

A main take-away from a study leading up to this work is that for low sea states better power conversion is achieved if the turbine/generator set follows a constant reference

speed [18]. The reference speed needs to be appropriate for the available energy in the waves. Originally, the reference speed was set to the average rotational speed previously obtained from the simulation with the Ideal FB control law (6.1) for each sea state. The power gains can be explained with the inertia of the turbine/generator set, that have been assumed to be zero when deriving (6.1). In this work an extended idea is pursued. Instead of a constant reference rotational speed, a time varying reference is allowed, but the reference signal shall have less frequent changes compared to the rotational speed that would be achieved with the Ideal FB control law. With the information gathered between the server array WECs 2,4 and 5 a reference signal can be computed online, which is guaranteed to be met wit the available wave energy. The server array has a wave estimator and reference speed generation algorithm on board to share the information with the client WECs.

6.2.1   Wave Estimator

The wave estimator in this work it not required to obtain detailed information about the ocean waves, instead its main goal is an estimate for the incident wave direction θ_{est} and an estimate for phase velocity $v_{\text{p,est}}$ (compare (1.6)) over the last approximately 100 seconds. The estimates are based on the time difference between significant wave troughs measured at the buoys of the server array. The condition for a wave trough candidate is

$$\boldsymbol{\eta}_{\text{tr}}(\boldsymbol{t}_{\text{tr}}) = \boldsymbol{\eta}(\boldsymbol{t}_{\text{tr}}) < 0 \text{ AND } \big(\boldsymbol{\eta}(\boldsymbol{t}_{\text{tr}}) - \boldsymbol{\eta}(\boldsymbol{t}_{\text{tr}-1})\big) < 0. \tag{6.20}$$

Here $\boldsymbol{t}_{\text{tr}} \in \mathbb{R}^3$ is the vector of time instances when a trough is at the respective buoy from the server array, namely WEC2, WEC4 and WEC5. The time step before the condition is satisfied is $\boldsymbol{t}_{\text{tr}-1}$. The time difference between WEC2 and WEC4 and WEC5 and WEC4 is of interest, thus

$$\Delta t_{42} = \boldsymbol{t}_{\text{tr}}(2) - \boldsymbol{t}_{\text{tr}}(1) \tag{6.21}$$

$$\Delta t_{45} = \boldsymbol{t}_{\text{tr}}(2) - \boldsymbol{t}_{\text{tr}}(2) \tag{6.22}$$

However, due to the irregularity of the waves sometimes the condition is satisfied shortly after the first one, if two local troughs follow each other (see Fig. 1.6 at 30 seconds). Therefore, Δt_{42} and Δt_{45} are only accepted if they are larger than 1 second. The one second is an estimate based on the minimal distance a wave has to travel between the first two WECs and WEC4, namely $(\sqrt{3}/2)d_{\text{s}}$ and the maximal expected phase velocity, based on $T_{\text{p}}^{\text{max}} = 14\,\text{s}$. Now, based on simple geometry within the equilateral server triangle array, the relation

$$0 = \sin\left(60° - \theta_{\text{est}}\right) - \frac{\Delta t_{42}}{d_{\text{s}}} v_{\text{p,est}} \tag{6.23}$$

$$0 = \cos\left(30° - \theta_{\text{est}}\right) - \frac{\Delta t_{45}}{d_{\text{s}}} v_{\text{p,est}} \tag{6.24}$$

holds when assuming a plane wave. Here, the distance between the WECs is assumed to be constant, since the entire park moves together horizontally, as shown in Chap. 4, thus d_{s} is used. The equation system (6.23) is solved in MATLAB/Simulink for θ_{est} and $v_{\text{p,est}}$ using the *Algebraic Constraint* block. Lastly, the frequently occurring

guesses are low pass filtered with a first order transfer function with time constant $\tau_{\text{est}} = 30\,\text{s}$,

$$\tilde{\theta}_{\text{est}}(t) = \left(1 - \mathrm{e}^{-t/\tau_{\text{est}}}\right)\theta_{\text{est}}(t) \tag{6.25}$$

$$\tilde{v}_{\text{p,est}}(t) = \left(1 - \mathrm{e}^{-t/\tau_{\text{est}}}\right)v_{\text{p,est}}(t) \tag{6.26}$$

The resulting estimates over time for the wave used in Sec. 4.3 is illustrated in Fig. 6.3. Recall, the incident wave angle used is $\theta = -15°$, which is successfully estimated after approximately 100 seconds.
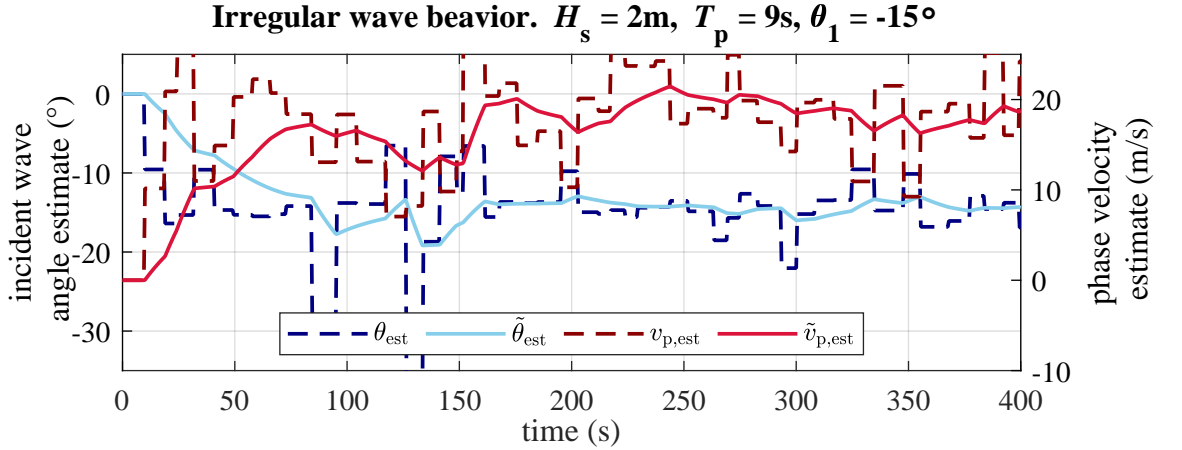

Figure 6.3: Time evolution of the estimated incident wave angle and the estimated phase velocity

6.2.2 Delayed and Smoothed Reference Rotational Velocity

Now, let us obtain the distances a plane wave needs to travel between the server WEC2 and its client WEC1 and WEC3 and between server WEC5 and its clients

WEC6 and WEC7. Again, the assumption that the horizontal distance between two distinct WEC does not change significantly compared to their initial distance holds, thus

$$\boldsymbol{d}_{\text{est}}(t) = \begin{bmatrix} d_{12}(t) \\ d_{32}(t) \\ d_{65}(t) \\ d_{75}(t) \end{bmatrix} = d_{\text{s}} \begin{bmatrix} \cos\left(30° - |\tilde{\theta}_{\text{est}}(t)|\right) \\ \sqrt{3}\cos\left(|\tilde{\theta}_{\text{est}}(t)|\right) \\ \sqrt{3}\cos\left(|\tilde{\theta}_{\text{est}}(t)|\right) \\ \cos\left(30° + |\tilde{\theta}_{\text{est}}(t)|\right) \end{bmatrix}. \tag{6.27}$$

Together with the estimated velocity of the wave this yields the time delay for the reference turbine velocity,

$$\boldsymbol{\tau}_{\text{ref}}(t) = \begin{bmatrix} \tau_{12}(t) \\ \tau_{32}(t) \\ \tau_{65}(t) \\ \tau_{75}(t) \end{bmatrix} = \frac{\boldsymbol{d}_{\text{est}}(t)}{\tilde{v}_{\text{p,est}}(t)}. \tag{6.28}$$

The instantaneous turbine rotational speeds from WEC2 and WEC5 are delayed so that after $\boldsymbol{\tau}_{\text{ref}}(t)$ the delayed reference velocity reaches $95\,\%$, with help of a first order time varying state space system,

$$\dot{\boldsymbol{x}}_{\Omega}^{\text{ref}}(t) = \begin{bmatrix} 3/\tau_{12}(t) & & & \\ & 3/\tau_{32}(t) & & \\ & & 3/\tau_{65}(t) & \\ & & & 3/\tau_{75}(t) \end{bmatrix} \boldsymbol{x}_{\Omega}^{\text{ref}} + \begin{bmatrix} 1 & 0 \\ 1 & 0 \\ 0 & 1 \\ 0 & 1 \end{bmatrix} \begin{bmatrix} x_{\Omega,2} \\ x_{\Omega,5} \end{bmatrix}. \tag{6.29}$$

Furthermore, the delay yields natural low pass filtering. This smooths out the high frequency turbine acceleration, which happens every time the air flow alternates. Consequently, the air pressure does not need to overcome the inertia of the turbine/generator at the high frequency, but can be opposed by the generator torque directly, improving the electro-magnetic energy conversion. The state space system for the reference speed is only activated when reference following is required, thus the initial condition is reset and set to the momentous rotational speed of the respective turbine. The last step is to decrease the reference rotational speed by 20% from its delayed states,

$$
\boldsymbol{\Omega}^{\mathrm{ref}} = \begin{bmatrix} \Omega_1^{\mathrm{ref}}(t) \\ \Omega_3^{\mathrm{ref}}(t) \\ \Omega_6^{\mathrm{ref}}(t) \\ \Omega_7^{\mathrm{ref}}(t) \end{bmatrix} = \begin{bmatrix} 0.8 & & & \\ & 0.8 & & \\ & & 0.8 & \\ & & & 0.8 \end{bmatrix} \boldsymbol{x}_\Omega^{\mathrm{ref}} \tag{6.30}
$$

Note that this constant value is arbitrary and it is chosen to ensure that the power flux in the diffracted wave is enough to reach the reference when hitting the client WECs. The resulting reference rotational velocity for server WEC2 and its client WECs is illustrated inf Fig. 6.4. The reference following system is not active whenever $\boldsymbol{\Omega}^{\mathrm{ref}}$ is constant, because the conditions for reference following are not met. The decision if the conditions are met is in the hand of the supervisory control system.
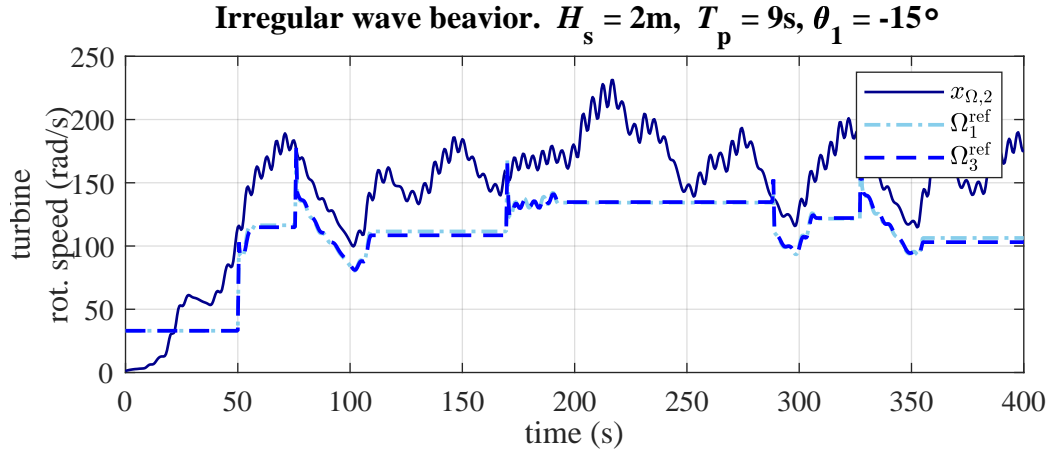
Figure 6.4: Turbine angular velocity from WEC2 and the generated reference velocity signal for WEC3.

6.3 Supervisory Control

To constrain the behavior of the previously presented Automaton in Chap. 5, Fig. 5.1 which describes the discrete event dynamics of the WEC park a standard supervisory control approach is used [45]. The approach is combined with some elements presented for the work on wind turbines [2]. Ultimately, the supervisor S_i is a discrete event Automaton T_i, driven by the states of the WEC park plant G_i, with an output map ψ_i, that imposes the predefined behavior onto G_i through a control action γ_i, as illustrated in Fig. 6.5. Let us name the desired Automaton

$$D_i = (Q_{\mathrm{D},i}, \Sigma_i, \delta_i, q_0, Q_{\mathrm{m},i}). \tag{6.31}$$

A language of an Automation is the (infinite) set of sequences of events along its path (see paths in Fig. 5.1). The general language of G_i shall be denoted $L(G_i)$ and the
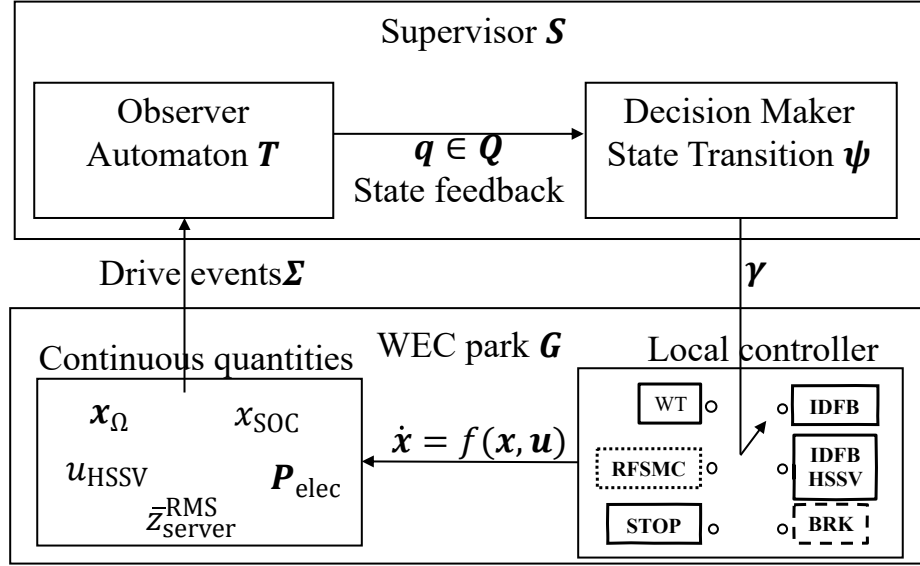
Figure 6.5: Hierarchical structure of the supervisory controller, managing the operation regime of the WEC park. The supervisor is driven by time continuous variables from the WEC park that trigger discrete events.

language of the behaviour over the marked states $L_{\mathrm{m}}(G_i)$. The language through the marker states Q_{m}, controlled by S_i in G_i is

$$L_{\mathrm{m}}(G_i, S_i) = L_{\mathrm{m}}(G_i) \cap L(G_i, S_i). \tag{6.32}$$

This is the language of the desired closed loop system.

6.3.1 Controllability and supervisor formal design

Now, let the language of the desired behavior of Automaton D_i be denoted K_i. Generally, the aim of the supervisor is not to modify $L(G_i)$ itself, but to achieve the desired

language $L_\mathrm{m}(G_i, S_i)$, while maintaining the nonblocking behaviour. The necessary condition for this language controllability [[45], prop. 4.1] are restated in

Proposition 1 *Fix a nonblocking Automaton G with closed language $L(G)$ and marked language $L_m(G)$.*

1. *For nonempty $K \subseteq L(G)$ there exists a supervisor S such that $L(G, S) = K$ iff K is prefix closed and controllable.*

2. *For nonempty $K \subseteq L_m(G)$ there exists a supervisor S such that $L_m(G, S) = K$, and the closed loop system is nonblocking iff K is controllable,*
   and $\bar{K} \cap L_m(G) = K$

Furthermore, K is controllable if

$$\bar{K}\Sigma_\mathrm{u} \cap L(G) \subseteq \bar{K}. \tag{6.33}$$

Here, $\bar{K}$ denotes a prefix of K. Therefore, (6.33) requires that any previous sequence of events in K if followed by an uncontrollable event u, needs to be be a prefix of another sequence in K. This makes $\bar{K}$ invariant under control action of Σ_u. Clearly, due to the desired cyclic behavior of the designed supervisor D_i, this condition is satisfied. The Automaton G_i can always be pushed back into a sequence of events in K_i and furthermore, as the marked states are part of D_i, K_i is $L_\mathrm{m}(G_i)$-*closed*, satisfying the second condition in proposition 1. Consequently, the supervisor can be realized with (T_i, ψ_i). The difference to, for example, a Markov Decision Process is that the WEC park dynamics under the local controllers are not stochastic and

Continuous	Discrete state				
rot. speed $x_{\Omega,i}$	(1) $[0;0.025)$	(2) $[0.025;0.9)$	(3) $[0;1)$	(4) ≥ 1	$\times \Omega_{\text{gen}}^{\max}$
valve pos. $u_{\text{HSSV},i}$	(1) $=0$	(2) $[0.4;1)$	(3) $=1$		
elec. power $P_{\text{elec},i}$	(1) ≤ -1	(2) $(-1;1)$	(3) ≥ 1		$\times P_{\text{gen}}^{\text{rated}}$
array motion moving RMS	(1) $[0;0.2)$	(2) $[0.2;0.4)$	(3) $[0.4;1)$	(4) ≥ 1	
battery charge x_{SOC}	(1) $[0;0.1)$	(2) $[0.1;0.2)$	(3) $[0.2;0.9)$	(4) $[0.9;1)$	

Table 6.1: Discrete Event Observer

specifying the language K_i after the paths identified in Fig 5.1 prescribes the desired closed loop behavior.

6.3.2 State Observer

The Automaton T_i , which is a component of the supervisor S_i functions similar to an observer, namely, it uses the state space states to detect the current discrete event state $q_i \in Q_i$. It is at this stage where knowledge about the system is incorporated into the numeric values that function as threshold. The first three rows of Table 6.1 are taken for each WEC i, whereas the last two rows are global states. The extreme values originate from the physical constraints. The intermediate intervals for the rotational speed intervals are determined due to the efficiency of the generator Fig. 2.9. It has to be noted that the values for the array motion which is based on the mean

moving average root-mean-square (RMS) heave position of the three server WECs is somewhat arbitrary, but based on the observations of the time domain simulation model power generation capabilities.

6.3.3 Decision Maker

All five states detected in Table 6.1 are used to construct the state transition function ψ_i for the supervisor S_i of WEC i (compare Fig 6.5). Here, ψ_i is a 5-tuple, with the respective dimension for the inputs, i.e. $\mathbb{Z}^{4 \times 3 \times 3 \times 4 \times 4}$. The state transition function is constructed before the simulation for every WEC i to implement a mapping from the discrete state q_i to a control action, based on the cyclic behavior originating from the design of the controlled Automaton in Fig. 5.1 and its prescribed language K_i. If no new discrete event occurs, there is no change in the discrete state and consequently no new control action. The only difference between server and client array is that instead of activating c_{3C}, the supervisor will force the WECs in the server array to activate c_4. The consequence of reaching a state with no predefined control action is c_9, the stop of the WEC.

Chapter 7   Control Simulation Results

The time domain simulations are conducted with MATLAB/Simulink using the fixed time step Euler (`ode1`) solver because of the solver's reliability when handling discontinuous dynamics ($\Delta t = 0.001$s). The discontinuous dynamics arise because of the switching nature of the SMC reference following control and the switching between different local controllers through the supervisor.

7.1   Detailed Irregular Wave Simulations

To illustrate the effectiveness of the proposed control architecture, the same sea state as in Chap. 4 is used with the same random wave created with the PM spectrum. Recall, the significant wave height is $H_s = 2$m and main energy period is $T_p = 10$s. The simulation is conducted over 1200s simulation time to go through different phases of WEC response. The detailed time evolution of important quantities from server WEC2 and client WEC3 are illustrated in Fig. 7.1 as an example. Clearly, the free surface elevation in the first plot is identical over the first 400 seconds as in Fig. 4.5 and so is the heave displacement of WEC2 $\hat{z}_2$ (as expected $\hat{z}_3$ is similar, but shifted in time). Therefore, the quantities like the horizontal and rotational displacements are not pictured. Instead, the focus is on the system states which define the control algorithms outputs and are vice versa impacted by the control feedback.
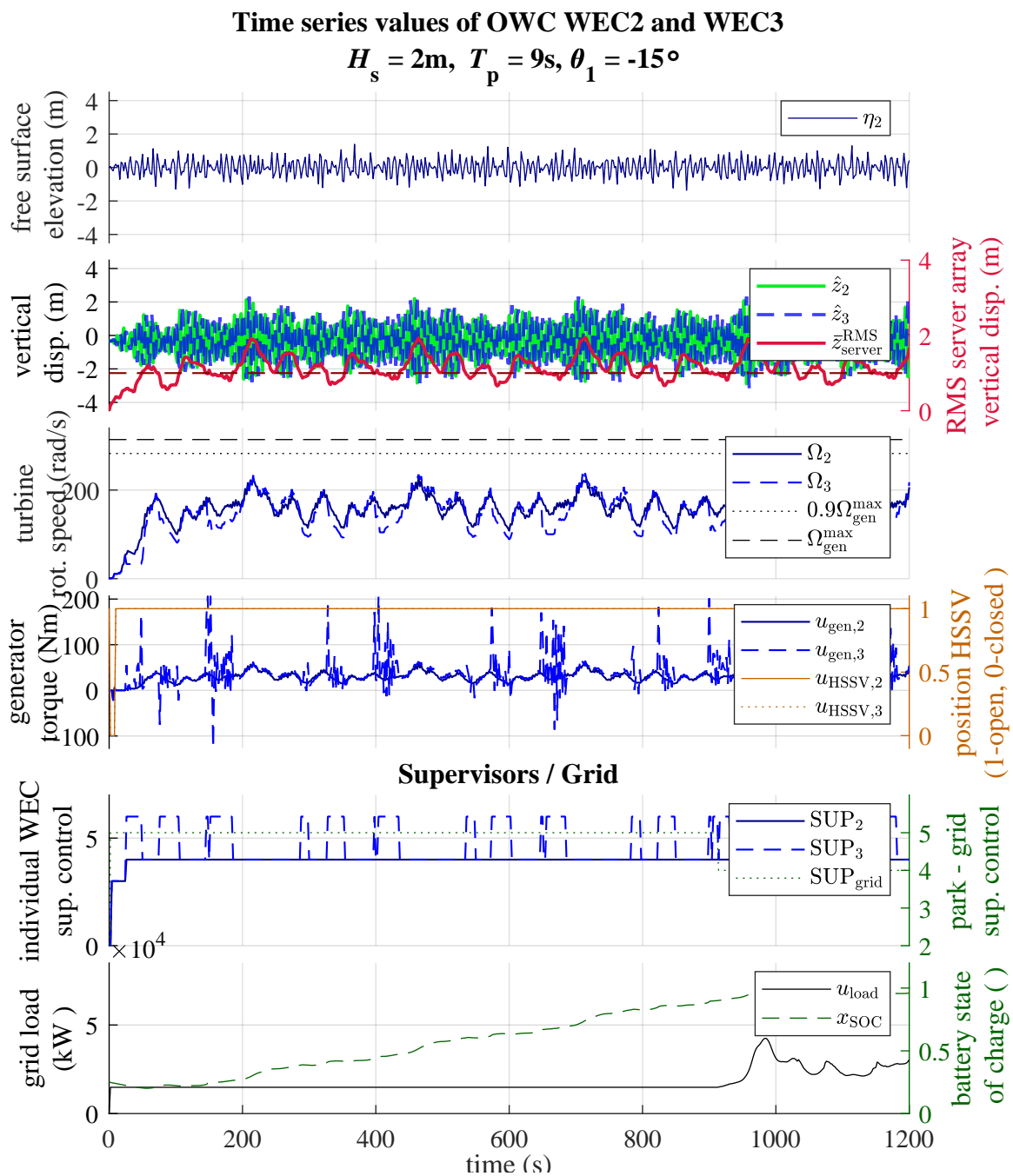
Figure 7.1: Time series simulation results for the (server) WEC2 and the (client) WEC3, in a random wave with $H_s = 2$m and $T_p = 9$s.

The rotational speed of the turbine/generator set is illustrated in the third plot of Fig. 7.1. Here, the rotational speed of the client WEC3 (in dashed blue) differs from $x_{\Omega,2}$ (in solid dark blue) when the reference following control is active. The reference following is active when the server array heave motion response is low (and if there is enough charge in the battery to input power into the client WECs). The resulting supervisor control output for WEC3 equals the value 6, which is illustrated in the six row of Fig. 7.1. During those time intervals the respective generator control torque $u_{\text{gen},3}$ in the fourth row seems to chatter. However, recall that the generator dynamics are much faster then the hydrodynamics and the 2nd order SMC signal is smooth in the order of a second, as shown in the more detailed studies [18, 19]. However, the continuing alternation between high and small control torque decreases the peak-2-average power ratio, but the electromagnetic energy conversion is forced to be at higher efficiency. The rotational speeds never exceed $0.9\,\Omega_{\text{gen}}^{\text{max}}$ (dotted), therefore the HSSVs of both WECs are open the entire time (after it is initially opened, see fourth row). The WEC park meets the constant grid base load and has excess power to continuosly increase the battery state of charge. When x_{SOC} gets closer to one the grid load u_{load} is increased so that $x_{\text{SOC}} < 1 \forall t$. Note that the efficiency assumed for the base load was not sea state dependent and the parks natural frequency of the park is close to $T_{\text{p}} = 9$s, therefore the wave-to-wire efficiency is higher compared to other sea states and the base load should be higher based on the newly gathered knowledge. Now, let us investigate the supervisor performance for a more energetic sea state, to evaluate if the protection mechanism work as they are designed to do. For this purpose a random wave with $H_{\text{s}} = 4$m and $T_{\text{p}} = 9$s is used and the results
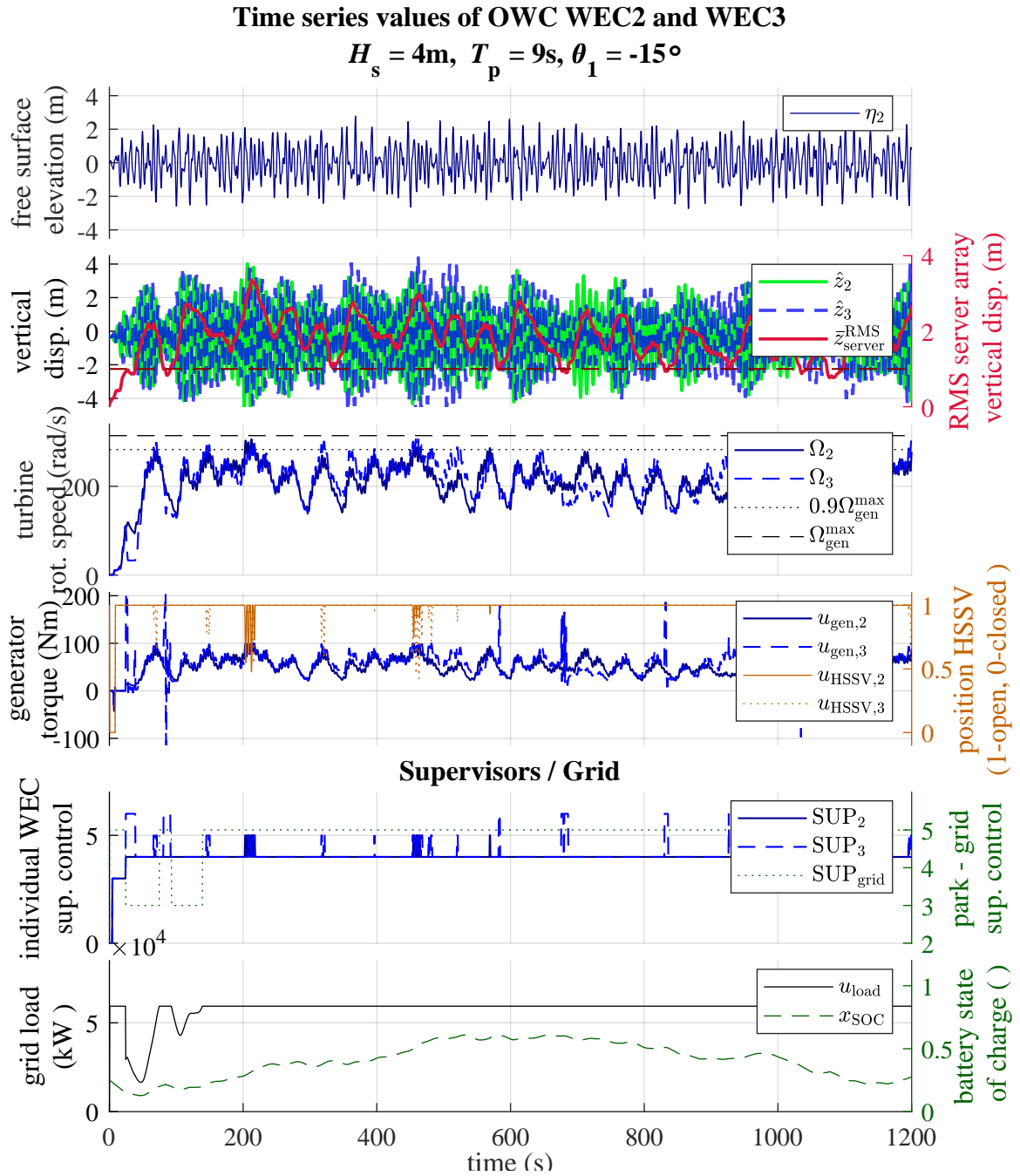
Figure 7.2: Time series simulation results for the (server) WEC2 and the (client) WEC3, in a random wave with $H_\mathrm{s} = 4$m and $T_\mathrm{p} = 9$s.

are presented in Fig. 7.2. The main difference to the previous wave case are, first, that the reference following control is activated less, because of the generally higher server array motion. Second, the rotational speed exceeds $0.9\,\Omega_{\mathrm{gen}}^{\max}$ (dotted), but with the partial closure of the HSSV (illustrated in the fourth row) to rotational speed is successfully kept below $\Omega_{\mathrm{gen}}^{\max}$ (dashed). Last, in the beginning of the simulation the park is not capable of delivering the constant base load, which is now higher due to the theoretical higher wave energy, see Sec. 6.1.5. As a consequence, the load is decreased to not drain the battery too much. The initial SOC is the same for all simulation runs. Fig. 7.3 presents the same simulation run, but only the time interval from 400 s to 800 s is illustrated. Consequently, the HSSV action becomes visible. Namely, the partial closure when the turbine/generator set is accelerating followed by entirely opening as soon as the rotational speed is back under $0.9\,\Omega_{\mathrm{gen}}^{\max}$. The control action $u_{\mathrm{HSSV},3}$ is higher than $u_{\mathrm{HSSV},2}$, as is the average rotational speed Ω_3 of the client WEC, resulting from the higher heave motion $\hat{z}_3$ response. The higher motion response is not control related, but due to the hydrodynamic interactions.

7.2 Average Power Results

This section presents average mechanical power and average electrical (AC) power simulation results. However, the focus is not on the absolute achieved values, but on the qualitative results when compared to the Ideal FB control law that has been used together with HSSV protection mechanisms in Sec. 4.3. Again, a power value in black illustrates a higher or equal power value when compared to the Ideal FB
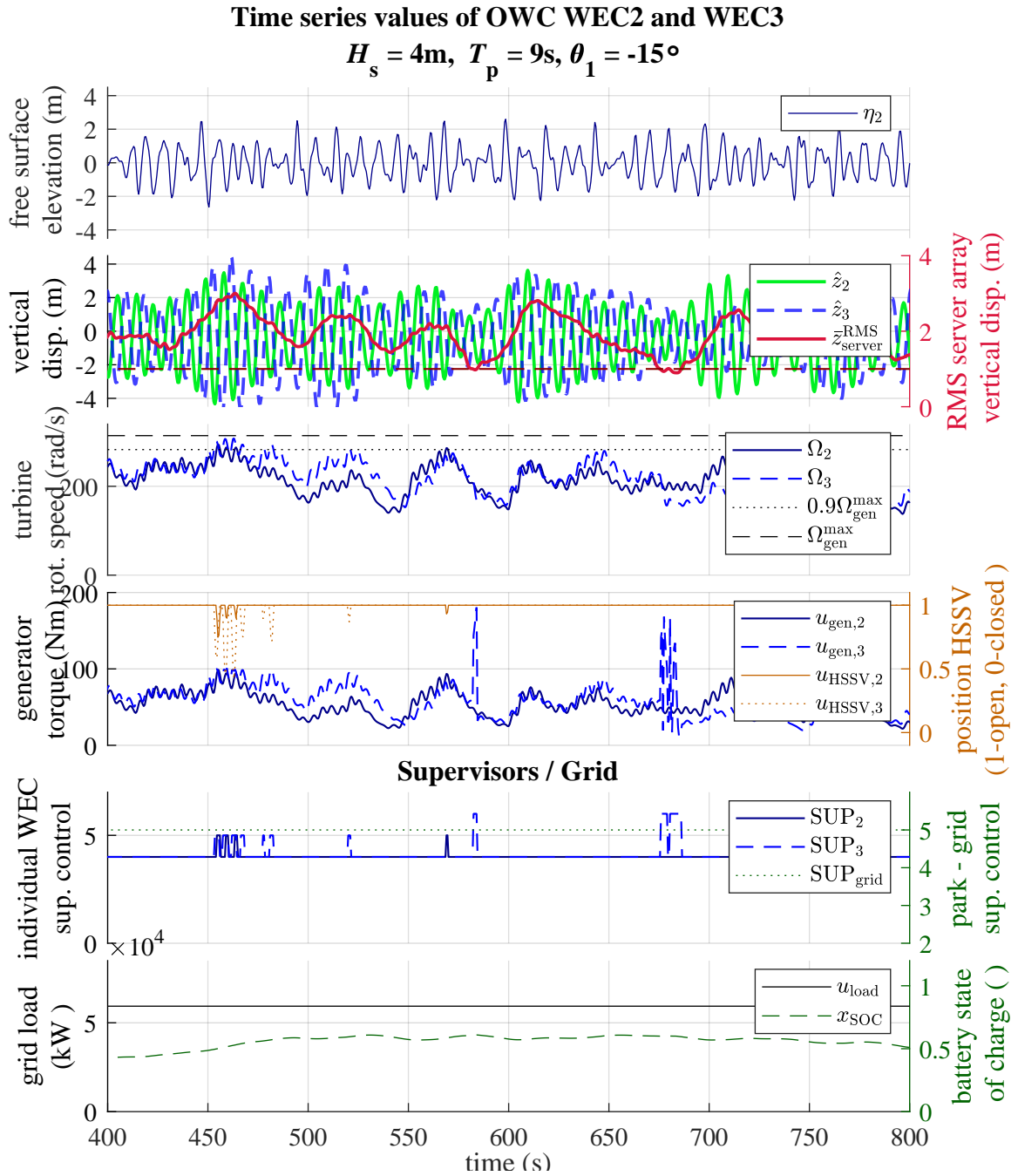
Figure 7.3: Time series simulation results from $400\,\mathrm{s}$ to $800\,\mathrm{s}$ for the (server) WEC2 and the (client) WEC3, in a random wave with $H_{\mathrm{s}} = 4$m and $T_{\mathrm{p}} = 9$s.

and a white font indicates less power, respectively. The main takeaways from the mechanical power results, illustrated in Fig. 7.4 are first that the annual mechanical power increase through supervisory control is insignificant with about 0.4%. Second, the supervisory controller spends more energy than energy is transferred to the turbine, in the very low energetic sea states ($T_\mathrm{p} = 4\,\mathrm{s}$ to $5\,\mathrm{s}$). Consequently, the WEC park should not be run with reference following mode enabled in the low energetic sea states. The color/shading of the average electric park power indicates more improvement compared to the mechanical power. This especially holds for the low-medium energetic sea states. Also, when looking at the number of sea states with black power values it becomes evident that the supervisor improves the wave-to-wire energy conversion in most sea states. However, the annual improvements are still only just short of 2%, which was to be expected, since the Spar-buoy type WECs dynamics are not significantly altered by the turbine and chamber dynamics.

Figure 7.4: Average park mechanical power for the supervisory control in the wave climate of Leixões, Portugal [43]. The color/shading indicates the comparison to the Ideal control law.
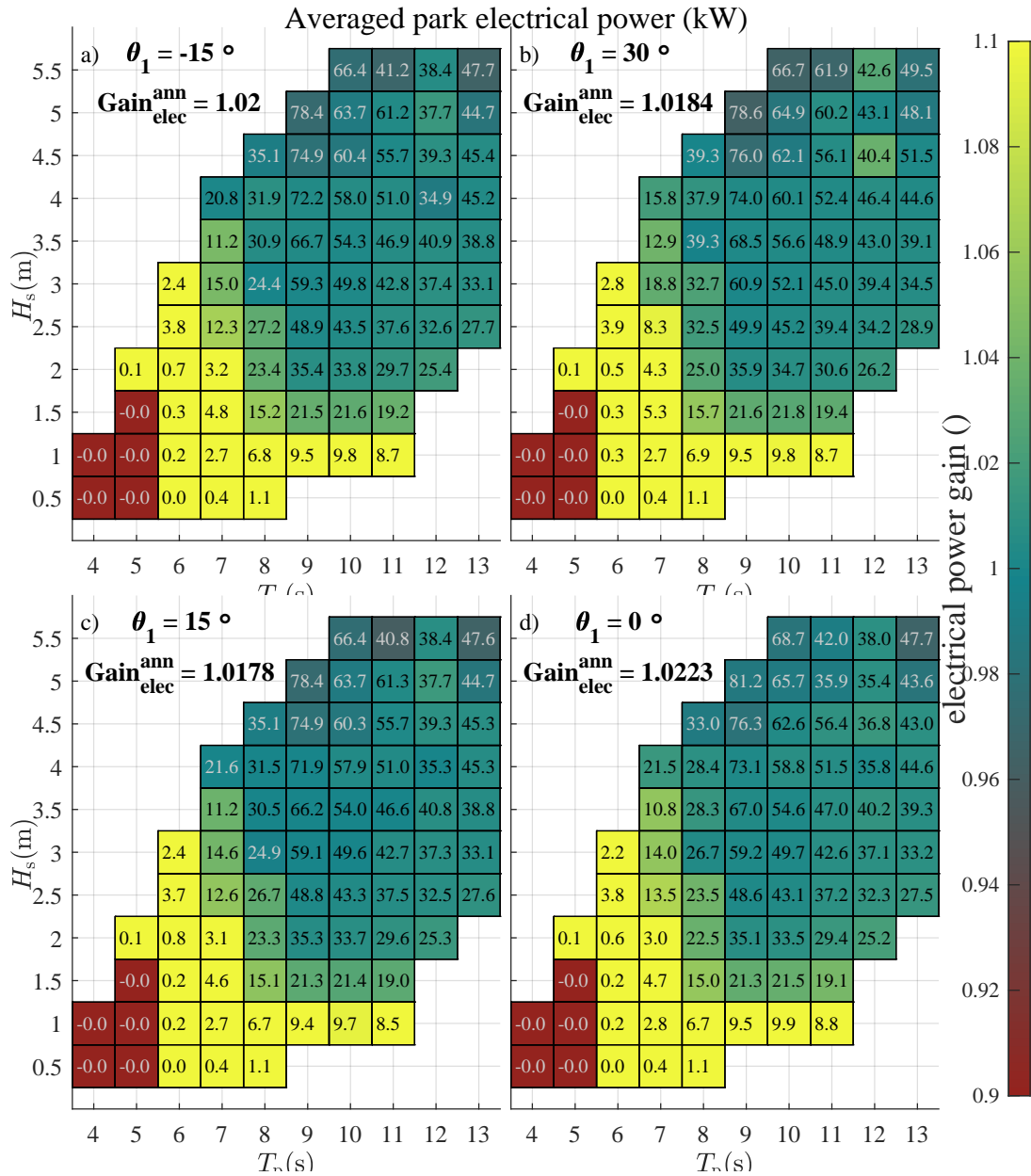
Figure 7.5: Average park electrical power for the supervisory control in the wave climate of Leixões, Portugal [43]. The color/shading indicates the comparison to the Ideal control law.

Chapter 8   Conclusion

The main contribution of this work is the detailed control oriented state-space simulation model. A version of the model which is restricted to heave motion is the foundation of five graduate students research. In the MATLAB/Simulink environment all signals and functions are generalized and vectorized such that new physical array configurations can be emulated conveniently when the necessary hydrodynamic coefficients are available and adjustments to the mooring configuration are made. As shown, the limitations of ANSYS Aqwa can be overcome with interpolation between different BEM results as part of the post-processing. The extended wave-to-wire model considering all degrees of freedom, which is presented in this thesis, proves that the preferable separation distance of 30 m is admissible with the used shared mooring configuration, without WEC collision. The average park interaction factor is lower than one, meaning that the park converts less power compared to the same amount of devices if they were isolated. However, the shared mooring configuration saves 66% of the mooring cable compared to individually moored WECs, which saves initial cost.

The WEC control inputs, namely the generator torque and the valve position have little to no impact on the hydrodynamic process of the floating Spar-buoy WEC, therefore it is difficult for a controller to improve the wave to device interactions. The relative pressure in the air chamber crosses zero about every WEC oscillation

period, due to the inhalation and exhalation. Consequently, maintaining the best efficiency of the self rectifying turbine at all times is impossible with the alternating air flow. There is the potential to maintain an ideal pressure head for longer by using the valve, but this comes with the downside of shedding power and decreasing the turbine efficiency.

This thesis focuses on the efficiency of the electromagnetic energy conversion as the leverage point for power improvement in different operating regimes. For times of low WEC - wave resonance a generally lower reference turbine velocity is prescribed from the server WECs to the client WECs. In times of high WEC-wave response an algorithm to shed power is used not only to physically protect the components, but to maintain a high generator efficiency. While this especially improves the average power in low energetic sea states, the annual electric power improvement for the sea climate in Leixões, Portugal is about 2%.

The implemented classical supervisory control approach ensures safe operation of the park with switching between different local controllers and it has emergency shut down options to protect the components. The supervisor is global in the sense that it uses global knowledge about the wave field and the WEC response, obtained from the server array performance, to make decisions for the client array. Although the proposed controller only improves the annual electric power conversion by 2%, it shows potential for investigations with different local controllers, optimized for different operating regimes. Furthermore, there is potential for the application of the standard supervisory control approach in Wave Energy in general, due to its adaptability to different WEC types and incorporation of safety mechanisms.

Unless Spar-buoy OWC WECs are equipped with additional actuators (mechanical solution), it is unlikely that even a globally optimal controller that takes all park interactions into account significantly improves power capturing, compared to the existing methods.

Bibliography

[1] Bret Bosma, Ted K. A. Brekken, Pedro Lomonaco, Aisha Mckee, Bob Paasch, and Belinda Batten. Physical model testing and system identification of a cylindrical OWC device. In *12th European Wave and Tidal Energy Conference (EWTEC), Aug 2017*, pages 910: 1–10, 2017.

[2] A. I. Bratcu, I. Munteanu, D. C. Cernega, and M. Culea. Safe and optimal operation of grid connected wind power systems by supervisory control. In *EUROCON 2007 - The International Conference on "Computer as a Tool"*, pages 2542–2549, 2007.

[3] T. K. A. Brekken, B. A. Batten, and E. A. Amon. From blue to green [ask the experts]. *IEEE Control Systems Magazine*, 31(5):18–24, 2011.

[4] A. A. D. Carrelhas. *Experimental study of the model and the prototype of a self-rectifying biradial air turbine with fixed guide-vanes. (in Portuguese)*. Master thesis, Instituto Superior Técnico, Universidade de Lisboa, 2017.

[5] A. A. D. Carrelhas, L. M. C. Gato, J. C. C. Henriques, A. F. O. Falcão, and J. Varandas. Test results of a 30 kW self-rectifying biradial air turbine-generator prototype. *Renewable and Sustainable Energy Reviews*, 109:187–198, 2019.

[6] S. De Chowdhury, J. R Nader, A. Madrigal Sanchez, A. Fleming, B. Winship, S. Illesinghe, A. Toffoli, A. Babanin, I. Penesis, and R. Manasseh. A review of hydrodynamic investigations into arrays of ocean wave energy converters.

[7] W.E. Cummins. The impulse response function and ship motions. *Symposium on Ship Theory at the Institut für Schiffbau der Universität Hamburg*, 01 1962.

[8] A. D. de Andrés, R. Guanche, L. Meneses, C. Vidal, and I. J. Losada. Factors that influence array layout on wave energy farms. *Ocean Engineering*, 82:32–41, 2014.

[9] Department of Trade and Industry. Near Shore Floating Oscillation Water Column: Prototype developement and evaluation. URN Number: 05/581, 2005.

[10] Patxi Etxaniz. Wave Energy: An industry with a bright future, 2017.

[11] Iain Fairley, Matthew Lewis, Bryson Robertson, Mark Hemer, Ian Masters, Jose Horrillo-caraballo, Harshinie Karunarathna, and Dominic E Reeve. A classification system for global wave energy resources based on multivariate clustering. *Applied Energy*, 262(October 2019):114515, 2020.

[12] Falcão, António F. de O. Wave energy utilization: A review of the technologies. *Renewable and Sustainable Energy Reviews*, 14(3):899–918, 2010.

[13] A.F.de O. Falcão and P.A.P. Justino. OWC wave energy devices with air flow control. *Ocean Engineering*, 26(12):1275–1295, 1999.

[14] António F.O. Falcão and João C.C. Henriques. Oscillating-water-column wave energy converters and air turbines: A review. *Renewable Energy*, 85:1391–1424, 2016.

[15] António F.O. Falcão, João C.C. Henriques, Luís M.C. Gato, and Rui P.F. Gomes. Air turbine choice and optimization for floating oscillating-water-column wave energy converter. *Ocean Engineering*, 75:148–156, 2014.

[16] Johannes Falnes. *Ocean waves and oscillating systems: Linear interactions including wave-energy extraction.* Cambridge Univ. Press, Cambridge, 2010.

[17] Daniel T. Gaebele, Mario E. Magaña, Ted K. A. Brekken, and Oliver Sawodny. State space model of an array of oscillating water column wave energy converters with inter-body hydrodynamic coupling. *Ocean Engineering*, 195:106668, 2020.

[18] Daniel T. Gaebele, Mario E. Magaña, Ted K. A. Brekken, João C. C. Henriques, Ana A. D. Carrelhas, and Luís M. C. Gato. Second order sliding mode control of oscillating water column wave energy converters for power improvement. *IEEE Transactions on Sustainable Energy*, 12(2):1151–1160, 2021.

[19] Daniel T. Gaebele, Mario E. Magaña, Ted K.A. Brekken, and João C.C. Henriques. Constrained sliding mode control for oscillating water column wave energy converters. *IFAC-PapersOnLine*, 53(2):12327–12333, 2020. 21th IFAC World Congress.

[20] Demián García-Violini, Nicolás Faedo, Fernando Jaramillo-Lopez, and John V. Ringwood. Simple controllers for wave energy devices compared. *Journal of Marine Science and Engineering*, 8(10), 2020.

[21] Giuseppe Giorgi, Rui P.F. Gomes, João C.C. Henriques, Luís M.C. Gato, Giovanni Bracco, and Giuliana Mattiazzo. Detecting parametric resonance in a floating oscillating water column device for wave energy conversion: Numerical simulations and validation with physical model tests. *Applied Energy*, 276:115421, 2020.

[22] Global Wind Energy Council. Global Wind Report 2020: Annual Market Update, 2020.

[23] Global Wind Energy Council. Global Wind Report 2021: Annual Market Update, 2021.

[24] R.P.F. Gomes, J.C.C. Henriques, L.M.C. Gato, and A.F.O. Falcão. Hydrodynamic optimization of an axisymmetric floating oscillating water column for wave energy conversion. *Renewable Energy*, 44:328–339, 2012.

[25] Rui Pedro Figueiredo Gomes. *Wave energy extraction from oscillating systems: numerical modelling and experimental testing*. PhD thesis, Instituto Superior Técnico, University of Lisbon, 2013.

[26] Rui P.F. Gomes, Luís M.C. Gato, João C.C. Henriques, Juan C.C. Portillo, Ben D. Howey, Keri M. Collins, Martyn R. Hann, and Deborah M. Greaves. Compact floating wave energy converters arrays: Mooring loads and survivability through scale physical modelling. *Applied Energy*, 280:115982, 2020.

[27] Malin Göteman, Jens Engström, Mikael Eriksson, and Jan Isberg. Fast modeling of large wave energy farms using interaction distance cut-off. *Energies*, 8(12):13741–13757, 2015.

[28] J. Harris. *Development of a Hybrid Simulation for an Ocean Wave Energy Converter*. Master thesis, Oregon State University Search for this term in SA@OSU, 2021.

[29] J C C Henriques, J C C Portillo, W Sheng, L M C Gato, and A F O Falcão. Dynamics and control of air turbines in oscillating-water-column wave energy converters: Analyses and case study. *Renewable and Sustainable Energy Reviews*, 112:571–589, June 2019.

[30] J. C. C. Henriques, W. Sheng, A. F. O. Falcão, and L. M. C. Gato. A Comparison of Biradial and Wells Air Turbines on the Mutriku Breakwater OWC Wave Power Plant. In *ASME 2017 36th International Conference on Ocean, Offshore*

and Arctic Engineering, page V010T09A037, New York, N.Y., 2017. American Society of Mechanical Engineers.

[31] J.C.C. Henriques, R.P.F. Gomes, L.M.C. Gato, A.F.O. Falcão, E. Robles, and S. Ceballos. Testing and control of a power take-off system for an oscillating-water-column wave energy converter. *Renewable Energy*, 85:714–724, 2016.

[32] S. Kung. A new identification and model reduction algorithm via singular value decomposition. In *Proceedings of the 12th Asilomur Conference on Circuits, Systems and Computers*, pages 705–714, Novermber 1978.

[33] Horace Lamb. *Hydrodynamics*. Univ. Press, Cambridge, 6th ed., repr., transf. to digital printing edition, 2006.

[34] Wilhelm Lauer and Jörg Bendix. *Klimatologie*. Das geographische Seminar. Westermann, Braunschweig, neubearb., 2., neu bearb. und korr. aufl. edition, 2006.

[35] Arie Levant. Sliding order and sliding accuracy in sliding mode control. *International Journal of Control*, 58(6):1247–1263, 1993.

[36] A. LiVecchi, A. Copping, D. Jenne, A. Gorton, R. Preus, G. Gill, R. Robichaud, R. Green, S. Geerlofs, S. Gore, D. Hume, W. McShane, C. Schmaus, and H. Spence. Powering the blue economy; exploring opportunities for marine renewable energy in maritime markets. *U.S. Department of Energy, Office of Energy Efficiency and Renewable Energy. Washington, D.C*, 1, 2019.

[37] L. Marquis, M. Kramer, and P. Frigaard. First Power Production Figures from the Wave Star Rpshage Wave Energy Converter, 2010.

[38] J.R. Morison, J.W. Johnson, and S.A. Schaaf. The force exerted by surface waves on piles. *Journal of Petroleum Technology*, 2(05):149–154, 1950.

[39] Jean-Roch Nader, Song-Ping Zhu, and Paul Cooper. Hydrodynamic and energetic properties of a finite array of fixed oscillating water column wave energy converters. *Ocean Engineering*, 88:131–148, 2014.

[40] C Oikonomou, RPF Gomes, LMC Gato, and AFO Falcão. Analysis of a triangular array of floating oscillating water column devices with inter-body mooring connections in regular waves. In *Proc. 12th European Wave and Tidal Energy Conference*, 2017.

[41] F. D. Ommanney. *The Ocean*. Oxford University Press, London, second edition edition, 1961.

[42] Markel Penalba and John V. Ringwood. A review of wave-to-wire models for wave energy converters. *Energies*, 9(7), 2016.

[43] J. C. C. Portillo, K. M. Collins, R. P. F. Gomes, J. C. C. Henriques, L. M. C. Gato, B. D. Howey, M. R. Hann, D. M. Greaves, and A. F. O. Falcão. Wave energy converter physical model design and testing: The case of floating oscillating-water-columns. *Applied Energy*, 278:115638, 2020.

[44] J. Prosser, J. Selinsky, H. Kwatny, and M. Kam. Supervisory control of electric power transmission networks. *IEEE Transactions on Power Systems*, 10(2):1104–1110, 1995.

[45] P. J. G. Ramadge and W. M. Wonham. The control of discrete event systems. *Proceedings of the IEEE*, 77(1):81–98, 1989.

[46] Jun B Rho, Hang S Choi, Hyun S Shin, and In K Park. A Study on Mathieu-type Instability of Conventional Spar Platform in Regular Waves. *International Journal of Offshore and Polar Engineering*, 15(2):104–108, 2005.

[47] John V. Ringwood. Wave energy control: status and perspectives 2020 ∗∗this paper is based upon work supported by science foundation ireland under grant no. 13/ia/1886 and grant no. 12/rc/2302 for the marine renewable ireland (marei) centre. *IFAC-PapersOnLine*, 53(2):12271–12282, 2020. 21th IFAC World Congress.

[48] David Ross. *Energy from the Waves*. Elsevier Science, Burlington, 2nd ed. edition, 1981.

[49] Albrecht Ruprecht. Ocean Energy: Lecture: winter semester 2017/2018, 2018.

[50] Liliana Rusu and Florin Onea. The performance of some state-of-the-art wave energy converters in locations with the worldwide highest wave power. *Renewable and Sustainable Energy Reviews*, 75:1348–1362, 2017.

[51] W Sheng, Raymond Alcorn, and Tony Lewis. Assessment of primary energy conversions of oscillating water columns. 1. hydrodynamic analysis. *Journal of Renewable and Sustainable Energy*, 6:053113, 09 2014.

[52] George G. Stokes. On the theory of oscillatory waves. *Transactions of the Cambridge Philosophical Society*, 8:441–455, 1847.

[53] Reza Taghipour, Tristan Perez, and Torgeir Moan. Hybrid frequency–time domain models for dynamic response analysis of marine structures. *Ocean Engineering*, 35(7):685–705, 2008.

[54] M. Takao, T. Setoguchi, K. Kaneko, S. Raghunathan, and M. Inoue. Noise characteristics of turbines for wave power conversion. *Proceedings of the Institution of Mechanical Engineers, Part A: Journal of Power and Energy*, 216(3):223–228, 2005.

[55] Alex Techet. Hydrodynamics: 2.016: Reading Nr.6, Added Mass. Reading Nr.6, Added Mass, 2005.

[56] James Tedd and Jens Peter Kofoed. Measurements of overtopping flow time series on the Wave Dragon, wave energy converter. *Renewable Energy*, 34(3):711–717, 2009.

[57] Tianna Bloise Thomaz, David Crooks, Encarni Medina-lopez, Leonore Van Velzen, Henry Je, Joseba Lopez Mendia, Raul Rodriguez Arias, and Pablo Ruiz Minguela. O & M Models for Ocean Energy Converters : Calibrating through Real Sea Data. *Energies*, 12, 2019.

[58] Pedro C. Vicente, A. F. O. Falcão, and Paulo A.P. Justino. A time domain analysis of arrays of floating point-absorber wave energy converters including the effect of nonlinear mooring forces. In *3rd International Conference on Ocean Energy*, 2010.

[59] Fabian Wendt, Kim Nielsen, Yi-hsiang Yu, Harry Bingham, Claes Eskilsson, Morten Kramer, Tim Bunnik, Ronan Costello, and Sarah Crowley. Ocean Energy Systems Wave Energy Modelling Task : Modelling , Verification and Validation of Wave Energy Converters. *Journal of Marine Science and Engineering*, 7:1–3, 2019.

[60] H. A. Wolgamot, P. H. Taylor, and R. Eatock Taylor. The interaction factor and directionality in wave energy arrays. *Ocean Engineering*, 47:65–73, 2012.

[61] K. D. Young, M. Thoma, and U. Ozguener. *Variable Structure Systems, Sliding Mode and Nonlinear Control*. Springer-Verlag, Berlin, Heidelberg, 1st edition, 1999.

[62] Yi-Hsiang Yu, Kelley Ruehl, Jennifer Van Rij, Nathan Tom, Dominic Forbush, David Ogden, Adam Keester, and Jorge Leon. Wec-sim v4.2, December 2020.

APPENDIX

Chapter A   Added Mass Numeric Values

The numerical values for the added mass matrices in (3.1) are stated below. The highest added mass values are due to the acceleration for the bodies itself, represented by

$$
A_{ii}^{\infty} \approx A_{11}^{\infty} =
\begin{bmatrix}
637580 & -7 & 3 & -118 & 2657400 & -265 \\
-10 & 637600 & -77 & -2657200 & 87 & -49 \\
-21 & -84 & 23748 & -905 & 253 & 0 \\
-96 & -2657300 & -798 & 79131000 & 1196 & 193 \\
2657600 & 88 & -12 & 993 & 79127000 & -1462 \\
-263 & -48 & -0 & 201 & -1487 & 1
\end{bmatrix}. \tag{A.1}
$$

The first cross-body interactions are taken into account with

$$
A_{ij}^{\infty} \approx A_{12}^{\infty} =
\begin{bmatrix}
-1548 & -1519 & -59 & 1507 & -2063 & 1 \\
-1533 & 214 & -35 & 298 & -1532 & 1 \\
-247 & -142 & 14 & 28 & -57 & 0 \\
1326 & 358 & -129 & -5358 & 38690 & -1 \\
-1892 & -1324 & 224 & 38639 & -49999 & 2 \\
0 & 0 & 0 & -1 & 2 & -0
\end{bmatrix}. \tag{A.2}
$$

The cross-body interactions in opposite direction is qualitatively similar, but note the change of some signs,

$$
A_{ji}^{\infty} \approx A_{21}^{\infty} =
\begin{bmatrix}
-1545 & -1530 & 60 & 1551 & -2086 & 0 \\
-1518 & 215 & 34 & 315 & -1531 & 0 \\
246 & 143 & 14 & -41 & 62 & -0 \\
1321 & 361 & 128 & -5321 & 38570 & -1 \\
-1900 & -1338 & -225 & 38660 & -49941 & 2 \\
1 & 0 & -0 & -1 & 2 & -0
\end{bmatrix}. \tag{A.3}
$$

The next matrix,

$$
A_{1}^{\mathrm{bp},\infty} =
\begin{bmatrix}
0 & 0 & 0 & 0 & 0 & 0 & 0 \\
0 & 0 & 0 & 0 & 0 & 0 & 0 \\
6883 & 0 & 0 & 0 & 0 & 0 & 0 \\
-223 & 260 & 260 & 260 & 0 & 0 & 0 \\
-381 & -448 & -448 & -448 & 0 & 0 & 0 \\
0 & 0 & 0 & 0 & 0 & 0 & 0
\end{bmatrix}, \tag{A.4}
$$

is one example for the effect of piston motion on a buoy. For different WECs the nonzero entries of $A_{1}^{\mathrm{bp},\infty}$ will be at the respective location conforming the interactions

distance cut-off. The same holds for the

$$
A_{\mathrm{b_1}}^{\mathrm{p},\infty} = \begin{bmatrix} -752 & 584 & 3491 & -547 & 0 & 0 \\ 0 & 0 & 0 & 225 & 1037 & 0 \\ 0 & 0 & 0 & 225 & 1037 & 0 \\ 0 & 0 & 0 & 225 & 1037 & 0 \\ 0 & 0 & 0 & 0 & 0 & 0 \\ 0 & 0 & 0 & 0 & 0 & 0 \\ 0 & 0 & 0 & 0 & 0 & 0 \end{bmatrix} , \tag{A.5}
$$

where the entries represent the added mass to all the pistons, due to the motion of the first buoy in six DoF. The piston-piston interactions clearly show the interaction distance cut-off structure,

$$
A_{77}^{\mathrm{p},\infty} = \begin{bmatrix} 14928 & -32 & -32 & -32 & 0 & 0 & 0 \\ -32 & 14928 & 0 & -32 & -32 & 0 & 0 \\ -32 & 0 & 14928 & -32 & 0 & -32 & 0 \\ -32 & -32 & -32 & 14928 & -32 & -32 & -32 \\ 0 & -32 & 0 & -32 & 14928 & 0 & -32 \\ 0 & 0 & -32 & -32 & 0 & 14928 & -32 \\ 0 & 0 & 0 & -32 & -32 & -32 & 14928 \end{bmatrix} . \tag{A.6}
$$